University of New Mexico
UNM Digital Repository

Optical Science and Engineering ETDs | Engineering ETDs

2-14-2014

IMAGING INTERFEROMETRIC MICROSCOPY TO THE LIMITS OF AVAILABLE FREQUENCY SPACE

Alexander Neumann

Follow this and additional works at: https://digitalrepository.unm.edu/ose_etds

Recommended Citation
Neumann, Alexander. "IMAGING INTERFEROMETRIC MICROSCOPY TO THE LIMITS OF AVAILABLE FREQUENCY SPACE." (2014). https://digitalrepository.unm.edu/ose_etds/31

This Dissertation is brought to you for free and open access by the Engineering ETDs at UNM Digital Repository. It has been accepted for inclusion in Optical Science and Engineering ETDs by an authorized administrator of UNM Digital Repository. For more information, please contact disc@unm.edu.

Alexander Neumann

Candidate

ECE

Department

This dissertation is approved, and it is acceptable in quality and form for publication:

Approved by the Dissertation Committee:

Professor S. R. J. Brueck , Chairperson

Professor J.-C. Diels

Professor M. M. Hayat

Professor K. Lidke

Professor R. P. Prasankumar

IMAGING INTERFEROMETRIC MICROSCOPY TO THE LIMITS OF AVAILABLE FREQUENCY SPACE

BY

ALEXANDER NEUMANN

M.S., Physics, Kazakh State University, 1982
M.S., Engineering, Moscow Institute of Physics and Technology, 1987

DISSERTATION

Submitted in Partial Fulfillment of the
Requirements for the Degree of
Doctor of Philosophy

Optical Science and Engineering

The University of New Mexico
Albuquerque, New Mexico

December, 2013

DEDICATION

To my father

ACKNOWLEDGMENTS

I wish to express my sincere gratitude to Professor Steven R. J. Brueck, who gave me opportunity to work on exciting problems and provided guidance during the research work. I am thankful for his participation in this work, for his enthusiasm and immense knowledge, for his patience, and his help with writing papers and this dissertation.

I would like to thank the members of my committee: Professors Jean-Claude Diels, Majeed Hayat, Keith Lidke, Rohit P. Prasankumar, for their advice, help and comments.

I am indebted to Yuliya Kuznetsova for encouragement, for her help in taking experimental data, for valuable discussions, and for help with writing papers. Her calm and friendly character made the collaboration really enjoyable.

I am thankful to Felix Jaeckel for making the mask with small features for our experiment.

I would like to take this opportunity to thank all the others who have contributed in any way, shape or form to the completion of this dissertation.

IMAGING INTERFEROMETRIC MICROSCOPY – RESOLUTION TO THE LIMITS OF FREQUENCY SPACE

by

Alexander Neumann

M.S., Physics, Kazakh State University, 1982
M.S., Engineering, Moscow Institute of Physics and Technology, 1987
Ph.D., Optical Science and Engineering, University of New Mexico, 2013

ABSTRACT

Imaging interferometric microscopy (IIM) is a synthetic aperture approach offering the potential of optical resolution to the linear systems limit of optics (~$\lambda/4n$). IIM allows one to resolve structures not accessible in a conventional illumination setup, while using a low *NA* microscope objective and thus keeping the large working distance, depth of focus and field of view associated with the lower *NA*.

The goal of this dissertation is to reach ultimate resolution limits of non-fluorescent microscopy by using IIM in new optical configurations realizing a solid immersion technique with immersion materials employed in advanced regimes unsuitable in other systems. The immersion advantages of IIM can be realized if the object is in close proximity to a solid-immersion medium. Illumination through the substrate involves photons propagating at angles beyond total internal reflection, collection of high frequencies, and decoupling this radiation by a grating on the medium surface opposite to the object. The spatial resolution as a function of the medium thickness and refractive index as well as the field-of-view of the optical system is derived and applied to

simulations. Structural illumination technique allows aliasing high spatial frequency into the low frequency range and using conventional microscopes at high resolution.

This technique may be useful for broad swath of technical applications, biological and medical research.

TABLE OF CONTENTS

LIST OF FIGURES

LIST OF TABLES

Chapter 1. Introduction

1.1 Overview

Microscopy is among the oldest and the most scientifically important applications of optics with a rich heritage extending hundreds of years. The fundamental physical principles of microscopy were established by Abbe, Rayleigh and others around the end of the nineteenth century [Abbe 1873, Rayleigh 1879].The diffraction limit of approximately one wavelength was established, but as we will see below, this is not a simple limit and care must be exercised in its interpretation. Notwithstanding this centuries old heritage, there are an increasing number of exciting developments in the microscopy of both illuminated (e.g. sensitive to spatial variations in the complex index of refraction) and self-luminous (fluorescent / photoluminescent) objects. Indeed, we are on the verge of enormous breakthroughs in microscopy and ultimately nanoscopy that will extend microscopy's reign as the most important scientific application of optics well into the future and will provide useful competition to other imaging modalities such as e-beam microscopy and the many variants of atomic force / scanning tunneling microscopy.

So what sets the stage for this explosion in possibilities and improvements? We see at least five major trends in modern microscopy:

1. Developments in lasers for illumination continue with advances in coherence, brightness, ultrafast pulses, etc. making easy and routine experimental arrangements that were previously tour-de-force laboratory triumphs. Examples are sources for two- and multi-photon microscopes and laser sources optimized for optical coherence tomography of scattering media such as biological tissue and

inhomogeneous solids.

2. Advances in the understanding and control of the quantum physics of molecular and solid-state materials. These are particularly critical for advanced fluorescence techniques, such as STED, GSD, STORM, PALM and others, which are briefly reviewed below, but are mainly outside of the scope of this dissertation.

3. Transfer of ideas from both long wavelengths (RF and microwave radar and imaging) and from very short wavelengths (lithographic imaging that is being driven by the demands of Moore's law into extreme sub-wavelength regimes.) At the long wavelength end of the spectrum, synthetic aperture radar imaging (SAR) has developed into a part of an all-important defense asset, e.g., airborne warning and control (AWACs) systems. The technology of SARs using relative motion between an antenna and its target region synthesizes larger phased array radar to provide much finer spatial resolution than is possible with conventional beam-scanning means [Curlander and McDounough 1991]. In microscopy, similar ideas are the foundation of imaging interferometric microscopy (IIM), reviewed below. At the short wavelength end of the spectrum, the demands of the silicon integrated circuit industry, requiring the ability to image and manufacture ever smaller features with ever greater densities over ever larger areas, have both borrowed from old ideas in microscopy (off-axis illumination, immersion, pupil plane filtering) and re-introduced some ideas back into microscopy (computational lithography/microscopy, nonlinear photoresist response and synthetic aperture techniques). As this is written (summer 2013) the silicon industry is manufacturing at the 32-nm node, with gate features of perhaps 10 nm, using a 193-nm photon

based lithography tool – certainly well below the wavelength. An essential aspect of lithography is that the photosensitive material, photoresist, has a highly nonlinear intensity response and offers the possibility of higher spatial harmonics to extend resolution for the binary imaging required for IC manufacturing. This is the basis of double patterning which is now the leading candidate for the manufacturing of the 22-, 16-, and 12-nm roadmap nodes [International Technology Roadmap for Semiconductors]. On the other hand, once you produce a lithographic pattern, it is not easily changed in other than a subtractive (etching) or additive (lift-off) process. In contrast for microscopy, digital manipulation of partial images is readily performed and forms an essential aspect of many of the new techniques.

4. Dramatic and continuing advances in the electronic capture, manipulation and storage of image information. CCD cameras with up to 500 megapixels (Mpx) are commercially available, and digital image processing has progressed enormously along with increasing computational capabilities. These advances are, of course, a consequence of the lithographic improvements that allow the definition of ~ 20 nm-scale features in integrated circuits.

5. Advances in nanophotonics and nanoscale fabrication of novel optical materials (metamaterials and plasmonics) that allow sub-wavelength manipulation of light. Interestingly, as is the case with so many "new" fields, plasmonics is an old field that is being reinvigorated by the fabrication advances, and by the antenna ideas of RF and microwave physics transposed to a new wavelength regime.

The result is an explosion of new techniques and new possibilities that offer a true revolution in the capabilities of optical microscopy and allow it to extend to the nanoscale, historically the domain of electron-beam techniques. This development is of particular importance for cell biology studies because of the need for imaging the dynamics of molecules in water-based ambients. Semiconductor manufacturing is another important application where the enhanced resolution possible with new techniques will play a significant role. As the benefits of integration and miniaturization are incorporated in photonics developments, microscopy will again have an essential role in characterization and inspection. The future of nanotechnology clearly involves additional integration and hierarchical nanoscale structures that will additionally require diagnostic and characterization tools capable of dealing with vast amounts of nanoscale information and extending beyond serial technologies to true imaging capabilities.

1.2 Parameters that describe microscopy

At its most ambitious, the goal of microscopy is to provide full three-dimensional structural and possibly spectroscopic (chemical) information of complex structures. This is a challenge of a very high order and many different techniques have been developed to attack its parts. These are briefly catalogued in this chapter.

It is useful to briefly define some of the most common specifications of microscope systems to provide a common language [Gu 2000, Török and Kau 2007]. A typical microscopy system consists of: a light source; an illumination system; a sample arrangement including a 3D scanning capability; a collection system (objective lens and auxiliary optics); and an image recorder, most often today an electronic camera interfaced with a

computer or other digital storage device.

Sources range from incoherent, continuous lamps and light emitting diodes to very high coherence (and therefore brightness) lasers, and to very high bandwidth, femtosecond (fs)-pulse lasers. This represents an enormous diversity of spectral, spatial and temporal characteristics and many different techniques have been developed to maximize the imaging information content and to take advantage of various source capabilities. The illumination system is characterized by a wavelength (denoted as λ) and numerical aperture that describes the angular distribution of the light incident on the sample plane. It is often desirable to manipulate the angular illumination distribution to enhance certain features of the image and it is important to keep in mind the distinction between the NA_{ill} which is:

$$NA_{ill} = \sin(\alpha_{ill}) \tag{1.1}$$

where α_{ill} is the maximum incidence angle of light that is transmitted through the illumination optics onto the object, and the measurement $NA_{ill\text{-}sys}$ which can be any subset of the angles within NA_{ill}. This distinction is often not made explicit in descriptions of microscopy techniques, which can lead to confusion. There is more detailed discussion of this issue in section 1.3.2.

The collection system consists of an objective lens, again characterized by an *NA* and auxiliary optics to transport the image to the camera for recording. Additional optics, such as polarizers, wave plates and prisms for Nomarski optical schemes, and phase plates for phase-contrast microscopy, are often incorporated in the optics after the objective lens. The working distance is the distance between the object and the first surface of the objective lens.

There are tradeoffs between resolution, depth of field, and working distance that are familiar to anyone who has used a microscope. In general, the resolution (see discussion below) increases linearly with the *NA* of the objective lens and with a decrease in the source wavelength. The depth-of-field decreases as the square of the *NA* within the paraxial approximation (in the paraxial approximation $\sin\theta_{NA} \sim \theta_{NA,}$ where $\theta_{NA} = \sin^{-1}(NA)$). These are fundamental relationships related to diffraction effects. In general, the working distance and the field of view decrease as the *NA* is increased, but this is specific to individual lenses and both quantities can be increased for a fixed *NA* with more complex (and more expensive) objective lenses.

1.3 Resolution

1.3.1 Image formation

Resolution in an optical image-forming system is a measure of the limits of the system to transfer information about small features in the object to the image. This quantity is very dependent on parameters of the imaging system including, but not restricted to: the illumination scheme (including the temporal and spatial coherence of the source); the optical characteristics of the object; the collection optical system including its aberrations (as a function of spatial frequency and position of a feature in the object plane); and the system noise. In general there is no single parameter that can fully characterize the resolution.

We begin by establishing a qualitative understanding of image formation. The rigorous theory of image formation is quite complex and is given in detail in many places [Born and Wolf 1999, Klein and Furtak 1986, Goodman 1985]. We present a much

simplified model that gives perhaps a fresh point of view on the imaging system to promote the understanding of some of its properties. The essence of this approach is to consider the optical response to a simple amplitude grating and then to recognize that it is possible, by Fourier analysis, to represent an arbitrary object as a superposition of gratings (a Fourier sum/integral). This makes available much of the apparatus of linear systems theory [Goodman1998]. However, it is important to remember that image formation is not a linear process. Light is scattered by the object, transmitted through the optical system and detected in the image plane by a nonlinear (square law) detector. This nonlinear step has profound implications on the final image and results in much of the complexity, but also has many advantages. It is natural to start an investigation of the system with just a simple grating object. Any object can be expressed in a Fourier integral, and this analysis is quite general as long as the nonlinear step at the detection plane is properly taken into account.

First, consider a simple single-lens, unity magnification, optical system, Fig. 1.1(a), with a thin (<< an optical wavelength) amplitude grating of period *d*(e.g. a chrome on glass structure) illuminated at normal incidence by coherent light of wavelength λ, and with a lens with a sufficiently large *NA* so that the zero-order beam, $E_0 e^{-ik_0 z}$, the symmetrical first order diffracted beams, $E_1 e^{ik_d x} e^{-i\sqrt{k_0^2 - k_d^2}z}$, $E_{-1} e^{-ik_d x} e^{-i\sqrt{k_0^2 - k_d^2}z}$, and the symmetrical second order diffracted beams $E_2 e^{i2k_d x} e^{-i\sqrt{k_0^2 - (2k_d)^2}z}$, $E_{-2} e^{-i2k_d x} e^{-i\sqrt{k_0^2 - (2k_d)^2}z}$ are collected by the optical system. Here $k_d \equiv 2\pi/d$ and $k_0 \equiv 2\pi/\lambda$ are the grating and photon wave vectors, respectively, x is the transverse spatial coordinate and z is the spatial coordinate in the direction of the optical axis. In general, there are higher order

diffracted beams, up to the optical transmission limit, $m \leq k_0/k_d$, with m an integer, and evanescent, non-propagating diffracted orders for larger integer values of m. To begin, we use a scalar approximation and ignore the polarization of the incident and scattered beams; below we discuss some of the limits of this approach. Initially, we ignore all z-terms by considering the image in the focal plane $z = 0$; note that there is a set of such planes including the object plane and the conjugate image plane defined by the optical system. For simplicity, this discussion is in terms of a transmission system ; extending to reflective system is straightforward.

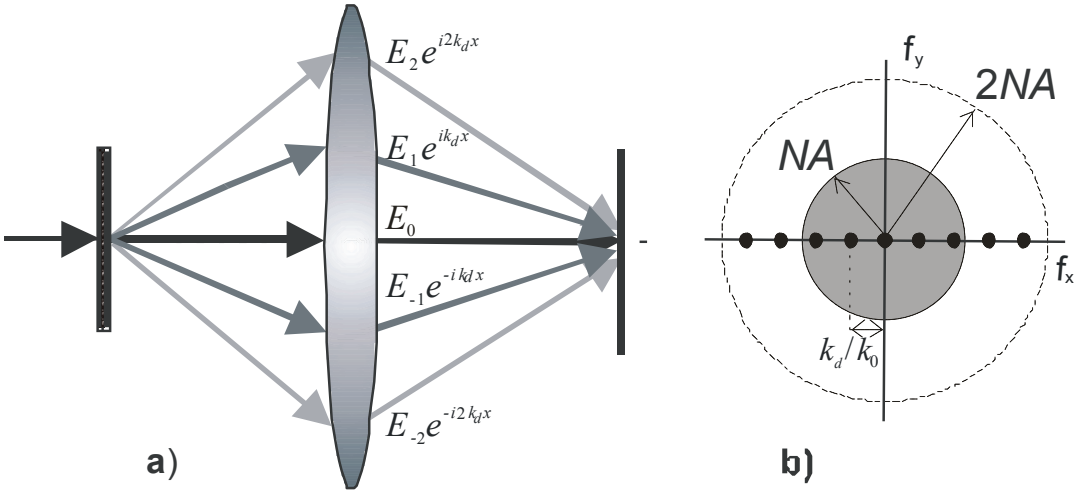

Fig.1.1. Image formation: a) arrangement and b) spatial frequency coverage. (For convenience of representation, we show the diffracted beams displaced in the vertical direction, and the corresponding spatial frequencies separated the horizontal direction; effectively the representation is rotated by 90° between parts a) and b).)

The image is formed by the interference of the zero-order beam with each of the higher order diffracted beams transmitted through the lens NA. In addition there are contributions from the interference of each order with itself (constant across the image)

and from the interference of different diffracted orders (the non-imaging terms that contribute to a dark field image). Mathematically, the field at the image plane can be described as:

$$E_{total} = E_0 + E_1 e^{ik_d x} + E_{-1} e^{-ik_d x} + E_2 e^{i2k_d x} + E_{-2} e^{-i2k_d x} = E_0 + 2E_1 \cos(k_d x) + 2E_2 \cos(2k_d x) \tag{1.2}$$

where the object is a thin amplitude grating so that $E_i = E_{-i}$, for $i = 1, 2$.

Then the intensity is:

$$\begin{aligned} I_{total} = &\left|E_0 + 2E_1 \cos(k_d x) + 2E_2 \cos(2k_d x)\right|^2 = \\ &\left|E_0\right|^2 + 2\left|E_1\right|^2 + 2\left|E_2\right|^2 \quad \textbf{(baseline)} \\ &+ 4\left|E_0 E_1\right| \cos(k_d x) + 4\left|E_0 E_2\right| \cos(2k_d x) \quad \textbf{(image)} \\ &+ 4\left|E_1 E_2\right| \cos(k_d x) + 2\left|E_1\right|^2 \cos(2k_d x) + 4\left|E_1 E_2\right| \cos(3k_d x) + 2\left|E_2\right|^2 \cos(4k_d x), \\ &\textbf{(dark field)} \end{aligned} \tag{1.3}$$

This result has been parsed into three categories: baseline or constant terms with no spatial variation, imaging terms corresponding to the interference between the zero and higher order terms, and dark field terms corresponding to the interference between two non-zero orders. Since the intensity is simply a sum of cosine functions, its 2D (x, y) Fourier transform is a series of δ-functions along the k_x transform coordinate, e.g. the Fourier transform of $\cos(2k_d x) = \left(e^{2ik_d x} + e^{-2ik_d x}\right)/2$ is just a pair of δ-functions at offset spatial frequencies of $\pm 2k_d$ along the k_x axis. For convenience, we plot this information in dimensionless coordinates, normalized to k_0 ($=2\pi/\lambda$) and denoted by f_x, so that the acceptance cone of the objective lens is a circle of radius *NA* as shown in Fig. 1.1(b). The domain of the image terms is restricted to this *NA* circle, whereas the dark field terms extend to a radius of $2NA$. Of course a δ-function is an idealized representation, as

limitations of the imaging system(e. g. field-of-view) will delimit the image and broaden the corresponding Fourier transform. The intensity of the zero-frequency component, at the origin of the (f_x, f_y) plot, from Eq. 1.3, is $|E_0|^2 + 2|E_1|^2 + 2|E_2|^2$. The amplitude of the δ-functions at the fundamental grating frequency, $\pm k_d/k_0$, equal to $4(|E_0E_1| + |E_1E_2|)$, has contributions from both imaging and dark-field terms. Similarly, the amplitude of the second order grating peaks at $\pm 2k_d/k_0$ ($= 4|E_0E_2| + 2|E_1|^2$) contains both imaging and dark field terms. The higher (third and fourth) order spatial frequency terms arise solely from dark field interference terms. Note that these terms arise from interference between two waves scattered from the object and that the observed frequencies are, therefore, linear combinations of the scattered frequencies from the object. Dark field imaging is quite useful in many microscopy applications: additional discussion will be provided below. Here, the goal is to recover the scattering coefficients (amplitude and phase) of the object and the dark field terms will be subtracted to leave the image terms.

It is possible to obtain the higher spatial frequency image terms using a lower (by up to a factor of two) *NA* lens along with off-axis illumination. We denote the numerical aperture of the low NA lens by NA_{low} to simplify the bookkeeping. In the case of NA_{low}, the grating period and lens *NA* are such that only the zero-order (grating transmission) and first diffracted orders are transmitted through the lens and onto the CCD camera (Fig. 1.2(a)) for normal incidence illumination. In this case, the intensity at the image (camera) plane is:

$$I_{low} = |E_0 + 2E_1\cos(k_d x)|^2 = |E_0|^2 + 2|E_1|^2 + 4|E_0E_1|\cos(k_d x) + 2|E_1|^2\cos(2k_d x) \quad (1.4)$$

The frequency space coverage is shown in Fig. 1.2(b). The E_1 beam is inside the lens *NA* and is transmitted to the image plane, the second order scattering (E_2 beam) is outside the

lens *NA* and is not captured by the optical system. The two points outside the gray circle represent the final term in equation 1.4; these are the result of mutual interference between the complementary first order fields. The distance between these two orders in frequency space is doubled and corresponding features appear beyond NA_{low}. These high frequency features (part of the "dark field") are a result of the square- law detection. The spatial frequency domain of the dark fields always extends over a frequency space with a radius of $2NA_{low}$ (dotted circle in Fig. 1.2(b)).

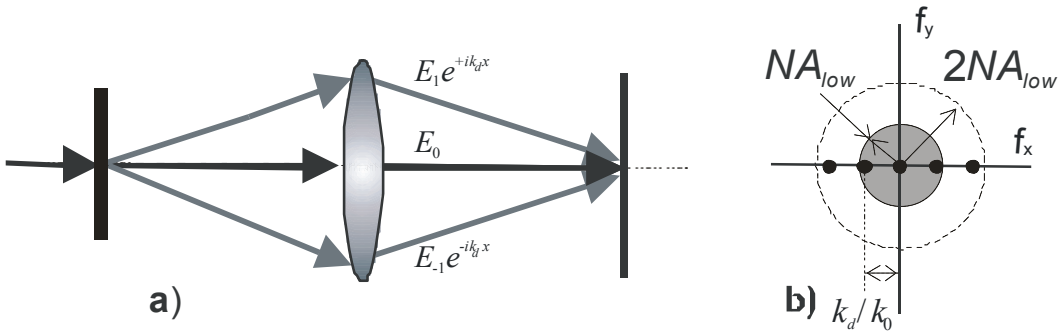

Fig.1.2. Image formation: a) arrangement with reduced NA and b) spatial frequency coverage.

One of the E_2 beams can be transmitted through the objective lens optical system by introducing a tilt of the illumination beam at an angle α_{ill}. Now every scattered plane wave from the object has an additional phase term $e^{-ik_0 \sin\alpha_{ill}x} = e^{-ik_o f_{ill}x}$ which means that the scattered beams are tilted in accordance with the grating equation, $\sin\theta_{out} = \sin\alpha_{ill} - mk_d/k_0$. Implicit in this result is that some scattered orders may switch from propagating to evanescent (and *vice versa*) depending on the wavelength and the grating period.

Here we choose α_{ill} such that the zero-order beam is near the one edge of the NA_{low} acceptance cone (Fig. 1.3(a)) and the E_2 beam is within the aperture on the opposite side of the acceptance cone.

Now the intensity at the image plane is:

$$I_{high} = |E_0|^2 + |E_1|^2 + |E_2|^2 + 2\left[|E_0 E_1| + |E_1 E_2|\right]\cos(k_d x) + 2|E_0 E_2|\cos(2k_d x) \quad (1.5)$$

The image part (middle term) is now the same as in Eq. 1.3 for the larger lens, within a factor of two. The constant terms and the dark field terms are different for the two optical systems (normal incidence illumination with *NA* lens and tilted illumination with NA_{low} lens). In this simple case, the imaging terms are identical to those obtained with the higher *NA* lens, although the dark field terms are different.

Notice that this is a single side-band system - either (E_0, E_1, E_2)or (E_0, E_{-1}, E_{-2}) are collected. The collected sidebands are shown in the gray-filled circle in Fig. 1.3(b); the frequencies within the conjugate symmetrical small circle offset in the opposite direction are restored as a result of the square law intensity response.

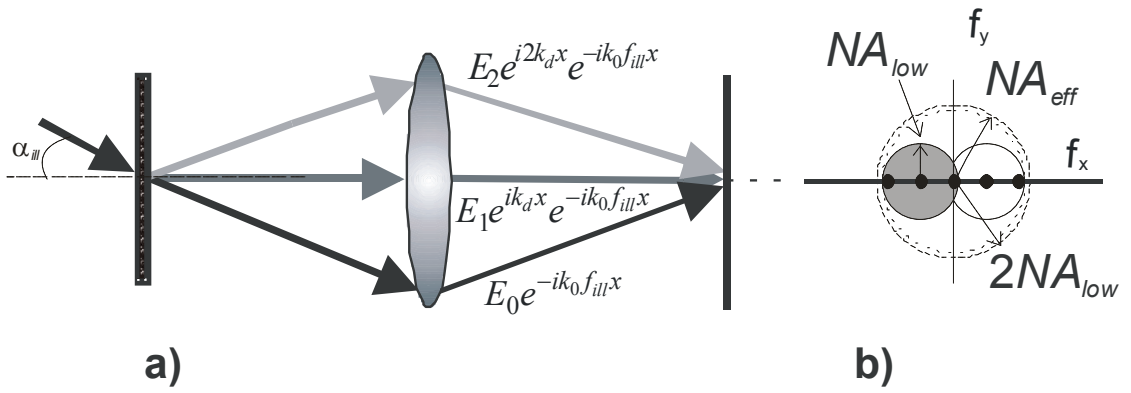

Fig. 1.3. Illumination tilt (a) – key to enhanced frequency coverage (b).

As will be discussed in more detail below, an issue with this configuration is that the image pattern shifts as the object is moved through focus, *i.e.* this optical configuration is not telecentric. Often this is addressed by illuminating with two mutually incoherent beams from opposite directions, α_{ill} and $-\alpha_{ill}$ to restore telecentricity; this is

known as dipole illumination. The circle of transmitted frequencies (gray-filled circle in Fig. 1.3(b)) is shifted by $\sin\alpha_{ill} = NA_{ill}$, so that the maximum collected frequency corresponds to an effective numerical aperture:

$$NA_{eff} = NA_{low} + \sin\alpha_{ill} = NA_{low} + NA_{ill}. \quad (1.6)$$

In other words, the effective aperture of the imaging system is a sum of both the illumination and collection apertures. Changing the angle of incidence, α_{ill}, shifts the spatial frequency coverage to different spatial frequency ranges. However the reader should not infer that NA_{eff} corresponds to the same frequency space coverage as a larger lens with an acceptance cone of NA_{eff} and normal incidence illumination. NA_{eff} refers only to the maximal transmitted frequency along the direction of the tilted illumination; the covered area in the transverse direction in spatial frequency space is still constrained by the smaller *NA*. Full frequency space information (large dotted circle in Fig. 1.3(b)) with radius NA_{eff} can be acquired with additional illumination beam offsets in other azimuthal directions (the azimuth is the angle φ from the *x*-axis in the *x*, *y* plane). As long as there is no coherence between the illumination beams (which would result in complex and undesirable interference effects), these can be applied simultaneously. For the simple grating structure, the optimum direction of the tilt to capture the most information is obvious; for arbitrary objects without a preferred direction, annular illumination, with incoherent illumination incident in a ring at a constant tilt angle around the edge of the pupil is often used. Thus, off-axis illumination can be used to collect the diffraction orders that fall outside of the collection *NA* of the optical system, up to frequencies of 2*NA*.Of course, because the offset has to be less than $\sin^{-1}NA$ to allow collection of the

zero-order transmission, the offset circles corresponding to the frequency coverage will overlap necessarily as shown in Fig. 1.3(b); this overlap represents unequal weighting of the overlapped spatial frequencies relative to singly covered frequencies that can impact the final image. In addition to varying the azimuthal angle, it is also possible to vary the offset or inclination angle of the illumination beam from the optical axis to cover additional regions of frequency space.

1.3.2 Coherent versus incoherent illumination

The imaging system is transparent for every scattered frequency within the acceptance cone, or entrance pupil, of the lens. For normal incidence illumination, it follows from Eqs. 1.2, 1.3 and Fig. 1.1 that the scattered electric fields are transmitted through the optical system with unchanged amplitude (and phase in the absence of lens aberrations) until the highest frequency is restricted by the entrance pupil (*NA*) of the system. Therefore, it is evident that the electric field transfer function (*ETF*) is a rectangular function (rect) in cross section with a cut off at *NA* as shown in Fig. 1.4(a). So, the *ETF* for an idealized lens and coherent illumination is just a circular (circ) function in two dimensions. Any source could be considered as 'perfectly coherent' if its coherence area is larger than the field-of-view of the objective lens.

Spatially incoherent illumination can be approximated as a superposition of mutually incoherent plane-waves with all possible *k*-vectors filling 2π steradians from normal to grazing incidence at all azimuth angles, which incorporates on-axis as well as all possible off-axis illumination directions at once. For each incident illumination direction, interference between the scattered beams forms an image with an offset spatial frequency

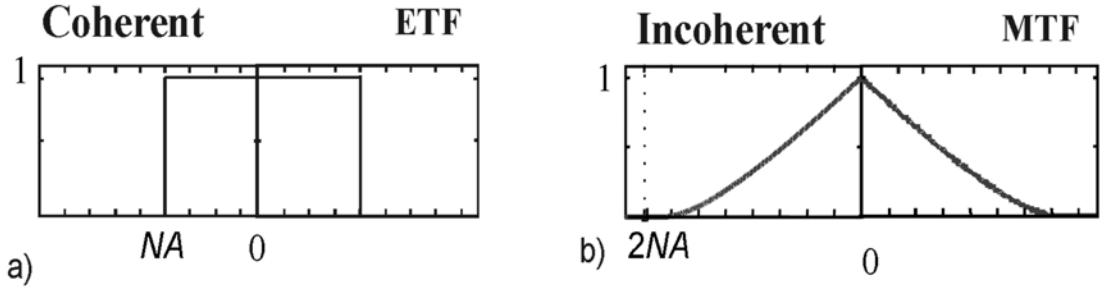

Fig. 1.4. Transfer functions: a) electric field transfer function (EFT) for coherent, normal incidence illumination; b) modulation transfer function (MTF) for conventional incoherent illumination imaging.

response similar to that shown in Fig. 1.3. Since the incident plane waves are mutually incoherent, so are the respective scattered beams and, therefore, each of these images are independent and the final image is a superposition of many incoherently related sub-images (e.g. intensities are added). For incoherent illumination, the optical transfer function for a circular aperture is the autocorrelation of the circular amplitude pupil function, called the modulation transfer function (*MTF*), and has the following form [Goodman 1998]:

$$MTF(f_i) = \frac{2}{\pi}\left[\cos^{-1}\left(\frac{f_i}{2NA}\right) - \frac{f_i}{2NA}\sqrt{1-\left(\frac{f_i}{2NA}\right)^2}\right]; \tag{1.7}$$

where f_i corresponds to the normalized spatial frequency. The *MTF* falls from 1 to 0 at twice the coherent cut off (Fig. 1.4(b)). Thus, for incoherent illumination, the spatial bandwidth extends to $2NA$, but with reduced fidelity at high spatial frequencies [Goodman 1998].

Incoherent illumination provides a linear relationship of the spectral intensity from the object to the image, in contrast to the coherent case, where the system is linear in electric field, up to the square-law detection step. Of course, we know from the wave

theory of optics that no source can be fully incoherent. Just as no far-field source can be focused to an optical spot smaller than approximately ½ the wavelength; similarly, the coherence area of any far-field source, restricted to propagating waves, is always larger than ~ λ/2. A necessary condition for Eq. 1.7 to apply is that the smallest feature of the object should be larger than the coherence area of the illumination. Nonetheless, Eq. 1.7 is a good approximation for many practical cases. The applicability condition is that the angular extent of the incoherent illumination should be greater than the sum of $\sin^{-1}(NA)$ and the angle corresponding to diffraction from the smallest features of the object. There has been much discussion in the optics literature of the practical limits of these ideas [Goodman 1985, Hopkins 1955].

Partial coherence refers to any illumination system between these coherent and incoherent limits. The discussion of partial coherence is often based on the numerical aperture of the combined source, NA_{src}, and illumination system, $NA_{ill\text{-}sys}$. For an extended source such as a tungsten filament, NA_{src}=1 is bigger than $NA_{ill\text{-}sys}$ but only $NA_{ill\text{-}sys}$ impacts the optical performance. For partial and incoherent illumination, there is a continuum of spatial frequencies spanning an extended range of angles incident on the object denoted as $NA_{ill\text{-}sys}$ in contrast to the maximum transmitted spatial frequency NA_{ill}. Most often for partially coherent illumination the center of the distribution of incident angles is normal to the object plane and $NA_{ill\text{-}sys}$ is equal in this case to NA_{ill} (Fig. 1.5 (a)); this is the context for the following discussion of the effects of partial coherence. Fig. 1.5 (b) shows the case of tilted illumination at an angle $\alpha_{ill} = \sin^{-1}NA_{ill}$.This case will reduce to coherent illumination as long as the spread in incident spatial frequencies $NA_{ill\text{-}sys}$ is close to zero. Other geometries are possible; two that are often used are annular illumina-

tion, where there is no illumination at normal incidence, but rather over a range of incident angles (inclinations from α_{min} *to* α_{max}) and at all azimuths (all φ) (Fig. 1.5 (c)), and quadrupole illumination, suitable for rectilinear (x, y) or Manhattan geometry objects as are often used in integrated circuits, where again there is a range of inclinations and φ is constrained to small ranges around $\pi/4$, $3\pi/4$, $5\pi/4$ and $7\pi/4$(Fig. 1.5 (d)). The quadrupole illumination can either be oriented at $\pi/4$ to the (x, y) axes, as shown, to provide a larger transfer function at intermediate frequencies, or at 0° to the (x, y) axes to provide higher maximum frequencies albeit at a smaller transfer function. The spread in incident spatial frequencies, $NA_{ill\text{-}sys}$, defines the degree of spatial coherence of the illumination system.

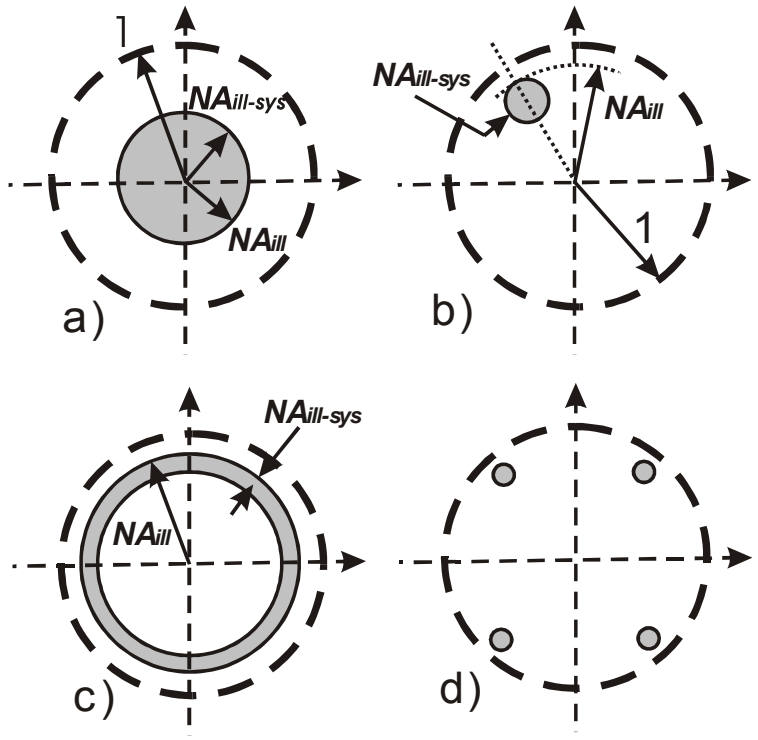

Fig.1.5. Alternate illumination schemes: a) partial coherent illumination with $NA_{ill\text{-}sys}= NA_{ill}$; b) tilted partial coherent illumination or tilted coherent illumination if $NA_{ill\text{-}sys}\sim 0$; c) annular illumination; d) quadrupole illumination.

To facilitate a more quantitative discussion, the ratio R = $NA_{objective}$ / $NA_{ill\text{-}sys}$ is often used [Goodman 1985]. Thus, R = 1 corresponds to matching the angular spreads of the illumination and collection optics, and R = ∞ corresponds to coherent illumination. There is a subtle difference between $NA_{ill\text{-}sys}$ and the NA_{ill} defined above in the context of coherent illumination, e.g. off-axis coherent illumination means $NA_{ill} > 0$, but $NA_{ill\text{-}sys} = 0$. On the other hand, of course, $NA_{ill\text{-}sys}$ is necessarily ≤ 1, as the idealized case of incoherent illumination, R → 0, includes near-field evanescent waves that are not available in a far-field system. The influence of the degree of partial coherence on the characteristics of the transfer function [Becherer and Parrent 1967] is shown in Fig. 1.6; there is little practical difference between the response for R ~ 1, matching the source and objective *NA*s, and fully incoherent illumination R = 0. In practical terms, an unfocused laser sourc

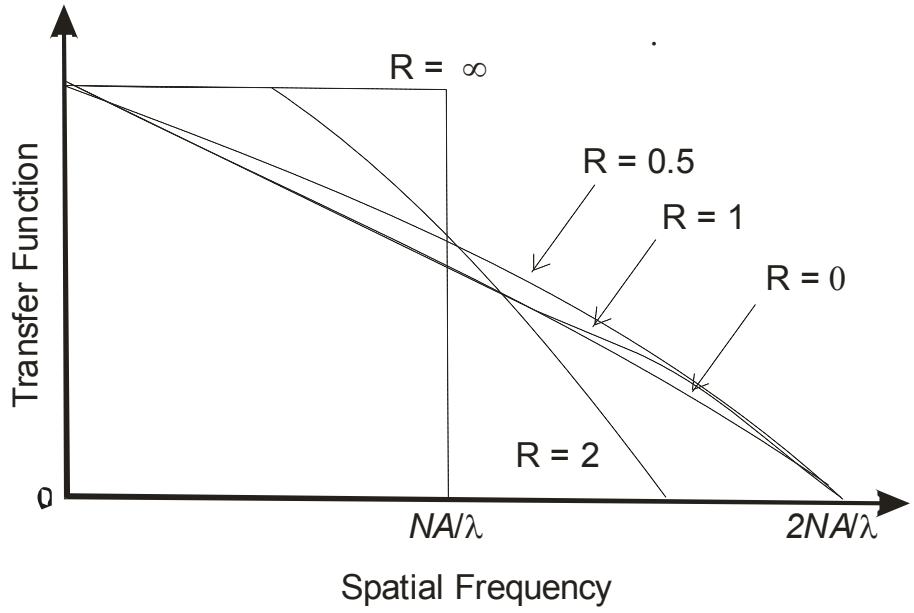

Fig.1.6. Apparent transfer functions for different degrees of partial coherence.

[Reprinted from Becherer and Parrent 1967]

provides coherent illumination, while an extended source such as a filament, coupled with an appropriate illumination system provides partially coherent or incoherent illumination. In lithography systems, where the limited bandwidth of the optical system requires a highly temporally coherence source (narrow linewidth), great pains are taken to eliminate spatial coherence ($R > 0$) to avoid speckle effects (interference between directly imaged light and scattered light within the optical system or flare). Note that the transfer functions of coherent and incoherent illuminations are not directly comparable, because of the difference in character between the electric field transfer function (the square law response is taken after applying the transfer function) and the modulation (intensity) transfer function. For comparison purposes, the apparent transfer function (ATF), which is the ratio of the output vs. input intensities of simple grating objects as a function of period, is used. This figure provides important insight into the behavior of optical imaging systems for different illumination conditions. The general trend is that higher values of R provide a more consistent transfer function across spatial frequencies, but cut-off at lower spatial frequencies. The optimal R is both subjective and dependent on the image pattern. An R between 0.75 and 0.5 provides a consistently higher image response than incoherent illumination ($R = 0$), while still providing some response to spatial frequencies beyond *NA*.

It is important to make a firm distinction between the frequency content within the pupil plane of the objective and that in the image plane. These are related by the square-law intensity response of the camera. Representations of the pupil plane for different illuminations are shown on Fig. 1.7 along with the frequency responses for a simple grating pattern. This figure is drawn for a somewhat more complex optical system

(known as a 4*f* optical system), where the pupil plane is easily identified, still with unity magnification for simplicity of representation. Both coherent (top half of object) and partially coherent illumination (bottom half of object) are shown. The diffraction from

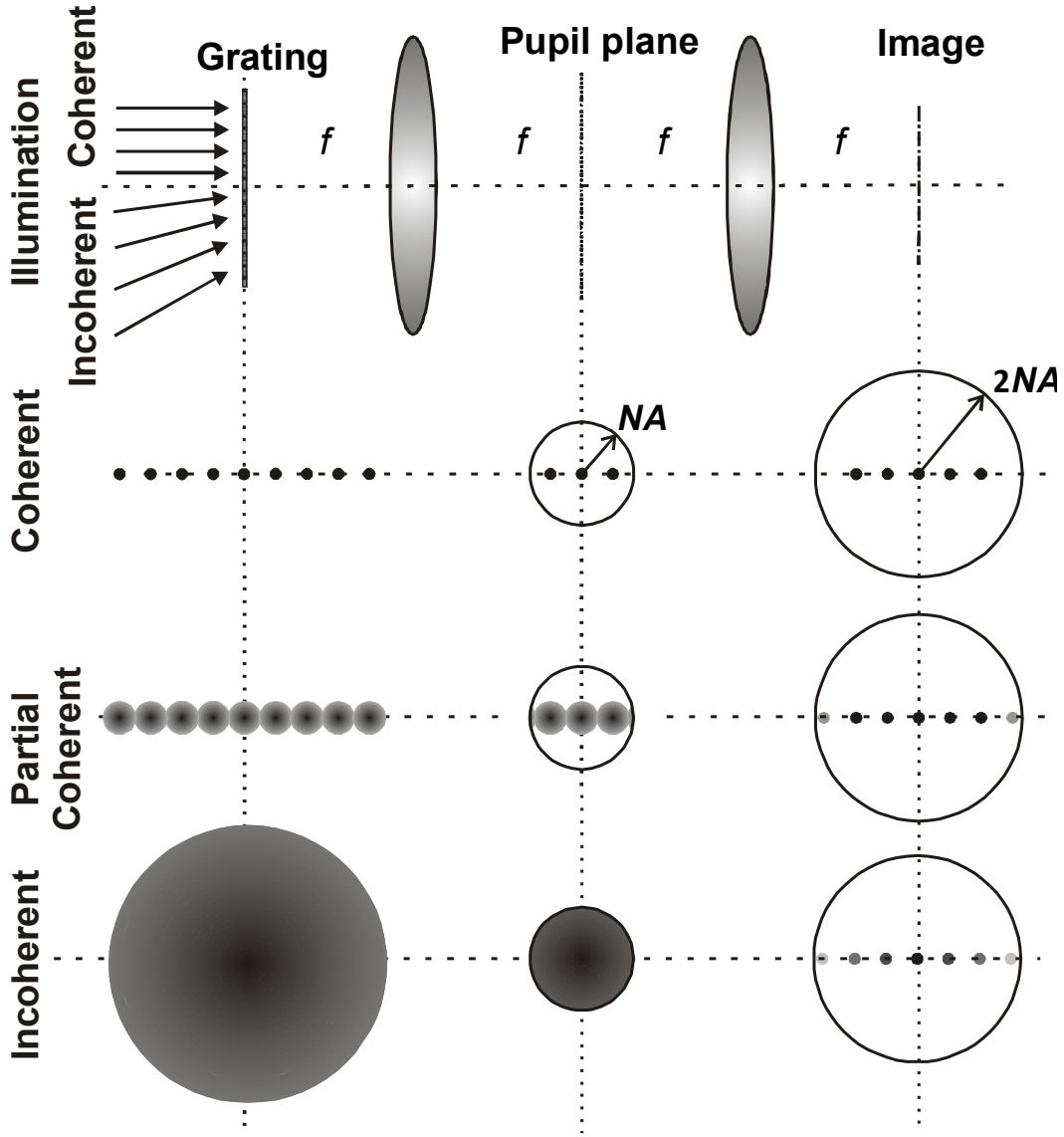

Fig. 1.7. Comparison of spectral content of optical system pupil plane and image Fourier plane.

the grating immediately gives rise to multiple orders at the object plane. For coherent illumination the 0, ±1, ±2, ±3, and ±4 orders are shown. The period of the grating is chosen so that only the 0 and ±1 orders are captured by the objective optical system and appear in the pupil plane. The representation shows, using a gray-scale, the amplitudes of the various orders that are focused to Airy disks in the pupil plane; there is a corresponding phase map that is not shown in this simple diagram. At the image plane, the square law intensity response results in an image containing frequencies corresponding to the 0, ±1 and ±2 spatial frequencies of the grating; the Fourier transform of this image is represented in the figure. The ±2 orders arise from the 'dark field' interference of the ±1orders transmitted through the pupil. The extent of the spatial frequency content of the image extends to $2NA$, while the pupil frequency content is limited to NA. For partially coherent illumination, each of the pupil plane regions are spread out as a result of the range of illumination angles. This results because in the pupil plane each plane wave corresponding to a specific coherent illumination angle focuses to a different, shifted Airy disk; the sum of all these Airy disks gives the spread out response corresponding to the partial coherence. In the image, each plane wave along with its corresponding diffracted beams image to the same grating features. The figure is drawn for R ~ 3. Notice that a small portion of the ±2 order diffraction information is captured by the optical system and this gives rise to additional higher spatial frequency terms in the image. Finally for incoherent illumination, the entire pupil is filled with each order, and the roll-off in the MTF is roughly represented by the gray scale of the image Fourier transform. Incoherent illumination gives very good signal to noise ratio with a reduced intensity transfer function at high frequencies. Coherent illumination can be plagued with

speckles due to interference associated with reflections from optical surfaces and to scattering from optical defects and dust particles. This noise can be partially reduced by decreasing the coherence length and subtracting the background recorded as an image of the illumination beam without an object [Voelz *et al*. 1997, Kuznetsova *et al*. 2007].

1.3.3 Definition of resolution specific to optical configuration

As mentioned above, a full discussion of resolution is a complex topic that is not in general amenable to a simple treatment. A resolution criterion is required for estimation of performance of the system and/or for metrology purposes. The achievable resolution is a function of the optical system, including the illumination scheme, and of the details of the object, so a simple definition of resolution applicable across all objects is not possible. Nonetheless it is useful to consider several of the most established and widely used short-hand characterizations of resolution.

In 1873, Ernst Abbe, then research director of the Zeiss Optical Works, understood that the ability of an optical system to resolve small features is directly connected to the ability of the system to transfer high spatial frequency information from the object to the image planes. He was the first to recognize the advantages of the off-axis illumination approach outlined above. In the context introduced above the smallest grating period accessible with a given objective corresponds to the case of the zero-order beam incident at one edge of the pupil and the first diffracted order at the opposite side of the pupil [Abbe 1873]:

$$d = \frac{\lambda}{2NA}; \quad \mathrm{Res} \sim \frac{\lambda}{4NA}; \tag{1.8}$$

Here the resolution is taken as the half pitch of the smallest period grating that can be

imaged through the optical system. This criterion (maximum transferred spatial frequency) is perfectly applicable in the case of 1-D structures and coherent illumination where there is a sharp cut-off in the band pass function at the edge of the pupil. However, the applicability of this simple criterion becomes more difficult if the transfer function is not constant across spatial frequencies, as in the case of incoherent illumination.

Now we address a simpler question. First, as have many before us, we restrict the object to a very simple structure, a pair of small ($<<\lambda$) apertures in a screen for a 2D structure or a pair of small lines for a 1D structure and ask the same question as Rayleigh [1879]: What is the smallest distance between a pair of objects where we can identify that there are two separate objects? We assume a perfect optical system without any aberrations and a large signal/noise ratio so no ambiguity is introduced by noise levels. Rayleigh suggested another metric, which states that the smallest resolvable distance between two point sources is the one that brings the maximum of one Airy pattern onto the minimum of the second [Rayleigh 1879]. The point spread function (PSF, which is the Fourier transform of the point source spectrum filtered by the optical transfer functions discussed above) of a circular pupil aperture is the Airy disk pattern, $[J_1(\pi NAr/\lambda)/(\pi NAr/\lambda)]^2$ where J_1 is the Bessel function of first order and r is the radial coordinate from the center of the spot, the first zero of $J_1$is located at $\pi NAr/\lambda = 1.22$, which determines the minimum resolvable separation of geometrical points d, given by the famous Rayleigh resolution criteria:

$$d = 2CD = 0.61\frac{\lambda}{NA}; \quad \text{Res} \sim \text{CD} \sim 0.31\frac{\lambda}{NA}, \tag{1.9}$$

where the *CD* or critical dimension, a concept borrowed from lithographic terminology, is the smallest resolvable linear dimension or half of the period. Comparing Eqs. 1.7 and

1.8, the resolution is a linear function of wavelength and inversely proportional to the numerical aperture in both cases. Note that Eq. 1.9 was derived for a particular case (incoherent illumination), a fixed pattern (two points of equal intensity), and a certain pupil shape (circular). Thus it can be only used quantitatively for this particular situation, but can serve as a qualitative, not quantitative, reference for comparison of optical systems.

Optical configurations for which the point spread functions (*PSF*) do not have zeros or obvious minima in the neighborhood of their central maxima (e.g., Gaussian *PSFs*) require generalization of this approach. A first attempt at such a generalization was undertaken by Rayleigh's contemporary, Sparrow, who reformulated the resolution as the distance for which the ratio of the value at the central dip in the composite intensity distribution to that at the maxima on either side is equal to 0.81. This corresponds to the dip in between the two $[\sin(\pi NAx/\lambda)/(\pi NAx/\lambda)]^2$ functions in the Rayleigh construct (Sparrow was working with lines in spectrographic applications. The dip is equal to 0.735 for two points) [Sparrow 1916]. However Sparrow recognized that even though a generalized Rayleigh criterion is capable of comparing different systems (at least in a qualitative sense), it is not suitable for quantitative metrology purposes because of its very high sensitivity to mutual intensity in the points. Indeed, the criterion should be applied with care even in the case of equal point (line) intensities and cannot be simply extended for more general cases. For example, taking three equal intensity equidistant lines (points) and varying the pupil aperture results in the intensity profiles shown in Figure 1.8. For a sufficiently large NA, that passes the spatial frequency corresponding to the spacing, the three lines are resolved. For very small NAs the three lines collapse into

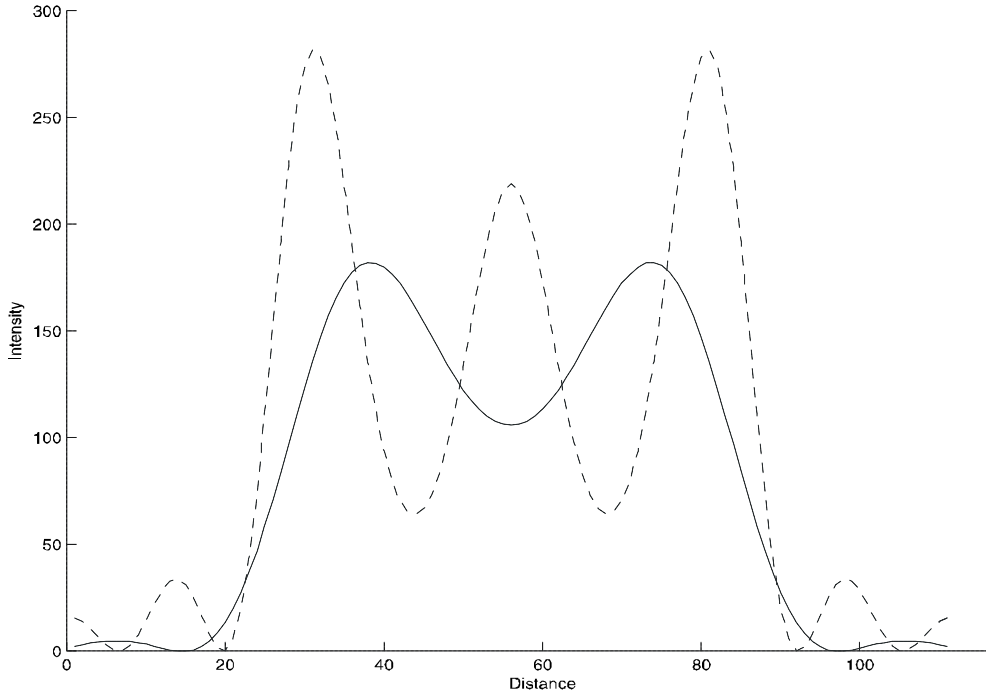

Fig.1.8. Example of a possible misinterpretation in application of the generalized Rayleigh resolution criterion (Three lines resolved (dotted); the same pattern after low-pass filtering (solid) shows only two lines with a dip that satisfies the resolution condition).

a single feature. However, at intermediate apertures, only two lines are apparent; in other words, while the dip satisfies the generalized Rayleigh condition, the three objects are represented by the optical system as two apparent objects and the resolution is clearly misrepresented by this criterion.

Sparrow suggested an alternative approach [Sparrow 1916]. Two PSFs should be moved towards each other from infinity. At large separation there will be a dip between the peaks. Finally, the separation, at which the dip disappears (second derivative become zero), should be considered as the resolution limit. This procedure works well even with differences in line/point intensities. However, it is not robust to system noise and is too

forgiving for cases with elevated PSF wings. All of these considerations are further complicated by extension to more complex arbitrary objects from simple point/line pairs. Similar issues plague any attempt at a generally useful definition of resolution for arbitrary patterns.

As the *NA* increases beyond the paraxial approximation, polarization effects influence the resolution [Richards and Wolf 1959, Raub *et al*. 2004, Köklü *et al*. 2009]. The two-dimensional PSF becomes roughly elliptical in the *x*-*y* plane. The interference of two tilted TE-polarized beams (transverse electric polarization, electric field perpendicular to the plane of incidence defined by the propagation direction and the normal to the image plane) is not influenced by the angle of tilt since the electric field vector remains the same independent of tilt. In contrast, the *E*-vector for TM-polarization (magnetic field perpendicular to the plane of incidence) continuously varies in direction with tilt. Both *x*- and *z*-components interfere independently with the corresponding vector components of the second interfering coherent beam with a 180° phase shift between the interference components. At a 45° tilt, the intensities are equal and the resulting contrast is zero; and for larger tilts the contrast is reversed. The resolution is higher (smaller focused spot size) for the TE direction.

1.3.4 Longitudinal resolution depends on illumination (focusing / defocusing)

The illumination scheme has a strong influence on the behavior of a defocused image and on the ability to separate features in the *z*-direction. To illustrate, first consider the defocusing associated with a dual side-band (telecentric) coherent optical system (Fig. 1.1, Eq. 1.2). Eq. 1.2 is written at focus (the image plane conjugate to the object plane)

where z is effectively zero and the propagation terms disappear. Complimentary (conjugate) orders from both sides (+1,-1; +2,-2; etc), beating with the zero order, form a pair of image gratings. For a thin (<<λ) amplitude (*e.g.* chrome on glass) object, every pair is mutually in phase (in focus at $z = 0$), i.e. the higher order image gratings are in phase with the lowest order grating. Defocusing causes the longitudinal phase terms (with variations in z) to change differently for each spatial frequency. The conjugate terms resulting from E_0E_1 and E_0E_{-1} now have opposite phase shifts, e.g. $e^{i\left[k_d x+\left(k_0-\sqrt{k_0^2-k_d^2}\right)z\right]}$ and $e^{-i\left[k_d x-\left(k_0-\sqrt{k_0^2-k_d^2}\right)z\right]}$, and they partially compensate each other. Thus the resultant intensity for a particular frequency initially reduces, goes to zero, and then reappears at multiple defocus planes. The z-direction periodicity is a function of the transverse period of that frequency component and the full image does not reappear (the different terms do not come into phase again at any focal position away from $z = 0$ except for the limiting case of only a single pair of ± 1 diffracted orders). This is easy to show by including the z-dependent terms in Eq. 1.2:

$$\begin{aligned} I_{image} &= 4\left|E_0E_1\right|\cos\left(k_d x\right)\cos\left[\left(k_0-\sqrt{k_0^2-k_d^2}\right)z\right] \\ &\quad + 4\left|E_0E_2\right|\cos\left(2k_d x\right)\cos\left[\left(k_0-\sqrt{k_0^2-\left(2k_d\right)^2}\right)z\right] \end{aligned} \tag{1.10}$$

Note, that the z-directed periodicities are different for the first and second order pairs. Hence, for a specific cut through the sample, there is only one conjugate image plane where all frequencies are in the correct phase relationship, *i.e.* there the image of this part of the object is in focus, at $z = 0$, the plane conjugate to the object plane as defined by the optical system. For other layers of the object, the frequencies have phase shifts with respect to each other that vary with the z-position away from focus and the image is

consequently blurred or more severely distorted.

The situation is more severe in the case of single-side-band imaging (Fig. 1.9). Here, the grating image shifts continuously to one side with defocus rather than disappearing and reappearing, e.g. instead of the separate cosine term, there is a continuous phase shift introduced into the pattern, e.g. instead of $\cos(k_d x)\cos\left[\left(k_0 - \sqrt{k_0^2 - k_d^2}\right)z\right]$, the variation is $\cos\left(k_d x + \left[\left(k_0 - \sqrt{k_0^2 - k_d^2}\right)z\right]\right)$. In this sense a single-side-band system has a quasi-infinite depth of focus. Choosing the correct focus even for a thin object becomes challenging in absence of *a-priori* knowledge of the object. In general, there is no possibility of sectioning a thick sample without additional information, which can be provided by using wide spectral range sources including short pulse, short coherence length, tunable lasers, tomography, and other techniques. Illumination with a short longitudinal coherence length source allows sectioning of the sample up to the scale of the coherence length. Short pulses and illumination with different wavelengths give the same possibility.

For incoherent illumination, which is always a telecentric double-side-band system, the picture is more complex. Here for every spatial frequency, a continuum of the beating pairs is built by the multiple off-axis illuminations, each pair with its own mutual phase shift (due to the different off-axis angles). The summed amplitude at a given spatial frequency still oscillates during change of focus with continuously reduced amplitude as shown in Fig. 1.9, curves (2-4) [Williams and Becklund 1989, Hopkins 1955]. So, if the object is out of focus, the MTF 'degenerates' and higher frequencies increasingly disappear as the sample is moved further from the objective focal plane.

Only the region around the conjugate image plane ($z = 0$) is 'in focus', and sec-

tioning of the sample is accomplished since only one layer of thickness corresponding to the depth of focus is visible; other layers almost vanish and don't perturb the focused region. Of course, this assumes that the object is weakly scattering and does not materially impact the propagation of the illumination beam. The depth of focus (Δz) is nearly proportional to the reciprocal of the area of the entrance pupil:

$$\Delta z = \frac{\lambda}{4n\left(1-\sqrt{1-NA^2}\right)} \tag{1.11}$$

In a weak scattering limit, so that the propagation of the fundamental beam is not strongly affected by the sample, 3D-sectioning is possible by longitudinal scanning of a thick sample in Δz steps.

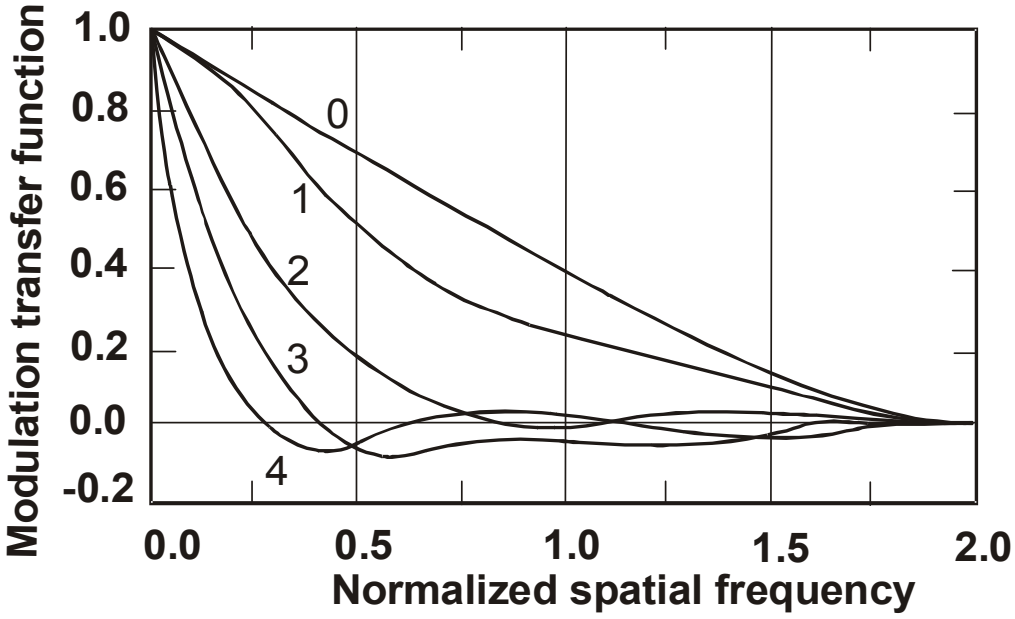

Fig.1.9. MTF curves for object planes in- and out of focus. The parameter is the normalized distance from focus in units of the depth-of-field [Reprinted from Proc. Royal Soc. (London), Hopkins 1955].

1.4. Enhancement techniques

Numerous additional techniques have been developed to enhance the images obtained with conventional microscopes. In particular, phase contrast and Nomarski techniques are often employed, particularly for low contrast biological samples. Phase-contrast microscopy was invented by Fritz Zernike (for which he received the 1953 Nobel Prize in Physics) [Zernike 1942]. For a sample with variations in thickness and/or in index of refraction, the E_1 and E_{-1} diffracted orders are not equal in phase, and information about the object is encoded in the phase difference between these pairs. This is especially problematic for colorless and transparent biological materials, as there is very poor image contrast associated with amplitude variations. Zernike suggested changing the phase of just the zero order, so that the phase difference for a particular pair can be balanced to enhance the contrast of image contours corresponding to a specific annulus in frequency space.

A related technique, phase shift interferometry (PSI), is a contemporary research topic. The gist is that by intentionally changing the zero-order phase in known steps it is possible after some digital analysis of the results to separate the amplitude and phase parts of the electric field in the image. The phase part contains combined information about both the average value of the index of refraction and the longitudinal position of the object in the *z*-direction. PSI is ideal for the investigation of reflective surfaces, where the longitudinal position corresponds to the surface itself. This position can be obtained with very high precision of about a few nanometers [Pitter *et al*. 2004, Dubois *et al*. 2001], and is the basis of the interferometers used to control stage position in micro-lithography steppers/scanners. Since this is an interferometric technique, the resolution is

not limited by the wavelength but rather by variations in the refractive index in the optical path during the multiple measurements (atmospheric variations) and by the signal/noise levels of the images. Sectioning of a thick sample is not possible by this technique.

Nomarski techniques are closely related to phase contrast microscopy. The basic principle is similar to the phase contrast microscopy technique but the implementation is different. A prism is used to split a polarized illumination beam into two slightly shifted plane waves that pass through the transparent phase object sample and are recombined interferometrically in a second prism before observation. This results in a differentiation of the image wherein regions of rapid phase variation are enhanced. Several texts provide a more detailed description of phase contrast and Nomarski microscopy [Born and Wolf 1999, Gu 2000, Murphy 2001].

1.4.1 Dark field microscopy

As noted above, dark field microscopy refers to the non-imaging terms that arise from interference between scattered waves other than the zero-order transmission (reflection) from the object. In general, there are two approaches to dark-field microscopy. In one approach, a block is used in the objective pupil to eliminate the zero-order light transmitted (reflected) from the object. This, of course, is only possible for coherent and partially-coherent illumination; for incoherent illumination, some of the zero-order transmission is necessarily transferred to the image plane. The frequency space content of the image is restricted to $2NA$. Assuming normal incidence illumination, the collected spatial frequency information is the same as that with conventional microscopy; however, dark

field microscopy offers contrast enhancement advantages similar to phase-contrast. The resulting square-law detection intensity pattern at the image plane is not truly an image, in the sense of a one-to-one correspondence of features of the image with features of the sample. This approach emphasizes higher frequencies (e. g. edges) and contains frequencies that are not necessarily present in the object (*cf.* Eq. 1.3).

An alternate approach to dark-field microscopy is to illuminate the object at angles beyond the lens *NA*; similar to the situation depicted in Fig. 1.3, but with the tilt increased so that the zero-order transmission is beyond the lens *NA*. In this case, higher spatial frequency scattered information is collected from the object, but the square-law response results in image frequencies again restricted to $2NA$; in other words, the high frequency content of the scattered light is down-shifted in the detection process. This technique provides an important starting point for the synthetic aperture approaches such as imaging interferometric microscopy, which is focus of this thesis. Often this illumination is in an annular pattern, similar to the annular illumination discussed above, but with all of the inclination angles of the illumination greater than the NA of the collection optical system.

1.4.2 Immersion microscopy

Immersion techniques to extend the frequency space coverage of microscopy [to NA~1.4-1.6; *i.e.* ~$\lambda/6$] are well established [Murphy 2001], but remain limited in application as a result of practical issues such as compatibility of immersion fluids with the sample. Traditional approaches with immersion fluids are restricted to *NA*s of ~1.4 by the available immersion fluids and the glass lens materials, as well as the difficulty of

fabricating high-*NA* aberration-corrected optics. Recently, a transmission microscopy approach using opposing immersion lenses and annular illumination has been demonstrated to have a resolution of ~λ/5 (90 nm) [Vainrub *et al*. 2006] and a commercial product is available [www.cytoviva.com].

1.4.3 Solid immersion microscopy

This approach uses a numerical aperture increasing lens (NAIL) placed on the substrate of an object to both illuminate with and collect scattered spatial frequencies at angles beyond the *NA* of the remote objective to reach the full linear systems limits of microscopy [Wu *et al*. 2000]. Full immersion will extend the frequency space coverage to $2n_{sub}/\lambda$. A resolution of λ/9 (145 nm with 1.3 μm illumination) was achieved by the optical set-up shown in Fig. 1.10 [Ippolito *et al*. 2000]. Spherical aberration is eliminated by the NAIL, but the large *NA* leads to a small field of view and other, higher order aberrations.

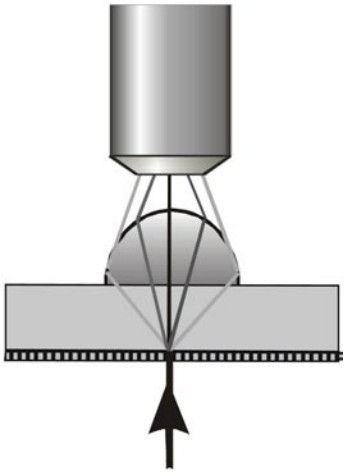

Fig. 1.10. High Resolution Subsurface Microscopy Technique

1.4.4 Near field microscopy

The highest spatial frequency information in the scattery of the object is contained in the near fields that are localized within distances of order of the wavelength or less from the object and are not accessible with far-field microscopy. The most straightforward approach is to build a small probe that can sample these fields and scan the probe to build up an image of the sample. With the enormous advances in scanning tunneling and atomic force microscopy, this has become both a feasible and a common approach. Relatively recent reviews are available [Courjon 2003, Novotny and Stranick 2006]. Both aperture-based and apertureless approaches have been explored. In the aperture-based approaches, a local light source, based for example on an optical fiber that has been stretched to the nanoscale and coated with a metal, leaving only the tip uncoated, is used as the probe. The primary difficulty with this approach is the limited amount of light that can propagate through the cut-off waveguide to the sample. In apertureless schemes a solid pointed metal probe is used either to scatter the local field from the sample or to illuminate the sample by exciting surface plasma waves that can propagate down the taper to the sample. Detection is by collecting the light scattered by the tip-sample geometry which varies with the sample optical topography. In all of these approaches it is important to account for the electromagnetic interaction between the tip and the sample. In effect, the tip perturbs the electromagnetic environment of the sample, changing the scattering/transmission characteristics. Near-field probes are serial scanning techniques which inherently require long times to build up an image, what is perhaps their greatest disadvantage.

1.5 Advanced directions in microscopy

Recently, many additional techniques have been introduced to enhance the resolution, either transverse or longitudinal, of conventional microscopy. Many of these rely on the inherent nonlinearity associated with two-photon processes (fluorescence) and with additional nonlinearities enabled by saturation and multi-photon excitation. These are somewhat outside of the scope of this thesis and are mentioned for completeness, along with references for further exploration. Codification of many of these techniques has recently been presented [Heintzmann and Ficz 2006, Hell 2007, Hell 2009].

Most of these schemes were developed for fluorescent materials, but there are some serious limiting issues associated with conventional fluorescence microscopy, particularly of biological samples. One of these is photobleaching of the fluorescent label (chromophore) [Gensch 2004] due to the bright illumination, which causes fluorescent dyes to fade within minutes of continuous irradiation. In addition to photobleaching, phototoxicity is also a problem [Hopt and Neher 2001]. Excited fluorescent dye molecules generate toxic free-radicals. Thus, biologists must limit the scanning time or light intensity to keep the specimen alive.

Some of these problems were solved with multi-photon microscopy [Denk *et al*. 1990]. Multi-photon absorption was predicted by Maria Göppert-Mayer in 1930 [Göppert-Mayer reprinted 2009], and a proof-of-principle experiment was performed in the 1960s using continuous-wave laser sources. Multi-photon fluorescence microscopy allows imaging in highly absorbing media, which increases detection sensitivity, image contrast, and enables full-frame video-rate fluorescence lifetime imaging, to reduce considerably the generation of phototoxic products. The resolution in this case is more

limited with a given fluorophore as compared to confocal imaging [Hell *et al*. 1992, Rudolph *et al*. 2003].

1.5.1 Confocal Microscopy

A technique called confocal imaging was first proposed by P. Nipkow and pioneered by M. Minsky who made the first scanning confocal microscope at Harvard University in 1957 [Wilson 1990]. Confocal microscopy is typically applied to fluorescent samples and provides both enhanced depth resolution and improved rejection of scattered light from adjacent objects [Webb 1996, Pawley 2006]. In contrast to the imaging techniques described above, confocal microscopy uses a point source, typically from a laser, to illuminate a single point on the object. The fluorescence from this point is then passed through a conjugate aperture in the collection system; this discriminates against light emitted from planes of the object that are away from the focus, since they are not reimaged at the conjugate aperture, and dramatically improves the longitudinal resolution. The object is then scanned in all three spatial directions to build up an image. This is a very powerful technique that has found much acceptance, particularly in biological imaging. The method allows scanning a series of thin optical 'slices' through the thickness (*z*-direction) of the specimen. In practice, the best transverse resolution of a confocal microscope is about 0.2 μm, and the best axial resolution is about 0.5 μm. Confocal microscopy has also been used for semiconductor diagnostics, particularly for determining the carrier diffusion length in semiconductors, by shifting the collection aperture relative to the input spot and monitoring the spatial decay of the photoluminescence [Fong and Brueck 1992, Fong *et al*. 1994].

1.5.2 4PI, I5M Microscopy

In conventional microscopy, the longitudinal resolution, along the optical or *z*-axis is significantly poorer than the transverse resolution; e.g. the depth-of-field is much larger than the transverse resolution. This limitation is addressed by increasing the solid angle (*NA* of the illumination source). The extreme is coherent illumination with a coherent optical source from both top and bottom sides with high-*NA* (immersion) lenses, known as 4π microscopy [Nagorni and Hell 1998]. To reduce optical scattering effects, two-photon fluorescence is often the observed quantity. Since a coherent laser source is used, this is a confocal configuration, the imaging is point by point, and the sample is scanned across a 3D focal volume. In 1999, interference microscopy (*I5M*) was demonstrated based on a novel interferometric technique in which the sample is observed and/or illuminated from both sides simultaneously using two opposing objective lenses and an incoherent source of illumination. Separate interference effects in the excitation light and the emitted light give access to higher resolution (~100 nm) axial information about the sample than can be achieved with conventional widefield or confocal microscopes [Gustafsson *et al*. 1999]. Since this is a wide field measurement, scanning is only in the *z*-direction, but additional artifacts are often present in the image [Bewersdorf *et al*. 2006].

1.5.3 Structured illumination fluorescence microscopy

Lateral resolution that exceeds the classical diffraction limit by a factor of two (λ/3.3) was achieved by using spatially structured illumination in a wide-field fluorescence microscope by Gustafsson [2000]. A sample was illuminated with a series of excitation light patterns, which encoded normally inaccessible high-resolution information into the

observed image. Additional nonlinearities associated with saturation extended the resolution to ~λ/10 [Gustafsson 2005].

1.5.4 Stimulated Emission Depletion (STED) and Ground State Depletion (GSD)

Even more impressive results have been obtained by STED microscopy [Hell *et al*. 1994]. The basic concept is to illuminate a fluorophore with two beams. One is a low intensity source that excites fluorescence. Since the spot size is limited by diffraction, so is the resolution, as discussed above. The second beam is a donut mode at a different frequency that deactivates the fluorescence through stimulated emission at a longer wavelength (to a higher level of the ground state manifold). Once again the definition of the donut hole is limited by diffraction. However, the depletion 'saturates,' the fluorescence only survives in regions where the second beam intensity is below a threshold value; increasing the intensity of the second beam provides a dramatically improved resolution, limited only by the accuracy of the "null" at the center of the donut. In an initial report, resolution of 33 nm (λ/23) was achieved [Marcus and Hell 2002]. This is accomplished by exciting the molecules with a femtosecond pulse and subsequent depletion of the excited state with red-shifted, picosecond-pulsed, counter-propagating, coherent light fields. Ground state depletion is a related technique wherein the molecular ground state is shifted to a long-lived "dark" state, for example a triplet, by the saturating donut-shaped pulse. Recently, the resolution was increased to λ/50 (15 – 20 nm) [Donnert *et al*. 2006]. In a recent review article, Hell [2007] proposed a revision to the Rayleigh criteria that applies to a number of nonlinear microscopies:

$$R \approx \frac{\lambda}{2NA\sqrt{1 + I_{\max}/I_s}} \tag{1.12}$$

Here, I_{max} is the maximum intensity of the saturation beam and I_s is the characteristic saturation intensity that quenches the fluorescence. For both STED and GSD, the resolution is ultimately limited by the quality of the null in the donut beam; once the intensity in the null exceeds the saturation intensity, all of the photoluminescence is quenched and no image remains. An example of applying STED to a solid state microscopy problem, the distribution of color centers in diamond, was presented by Rittweger *et al*. [2009].

1.5.5 Photoactivated Localization Microscopy (PALM) and Stochastic Optical Reconstruction Microscopy (STORM)

Both of these related techniques take advantage of improved localization, by fitting the centroid of an isolated PSF, rather than resolution or distinguishing between two overlapping PSFs [Betzig *et al*. 2006, Rust *et al*. 2006, Hess *et al*. 2006]. The basic idea is to use one illumination source to "turn-on" fluorophores that are separated by distances greater than the optical resolution. Then take a number N of images of the same fluorophores, and by fitting them achieve a centroid definition of $\sim \lambda / 2NA\sqrt{N}$, deactivate the fluorophores by some saturation mechanism (perhaps by blinking of quantum dots) and excite another set. Repeat multiple times until a full image is developed. This process is quite lengthy, taking many hours for typical biological entities and is not suitable for real-time observations. Though recent development of advanced algorithms for high-density localization of active molecules is a promising approach to solve that issue [Huang *et al*. 2011, Lidke 2012].

1.5.6 Nanophotonics – Plasmonics, Nano-Antennas and Metamaterials

The extraordinary enhancements observed in surface-enhanced Raman scattering (SERS) with colloidal Ag nanoparticles, up to 10^{15}, provide ample evidence of the strong field enhancements (nano-antennae) that are available with localized surface plasma wave resonances of complex structures [Moskovits 1985, Campion and Kambhampati 1998]. This has been an active research field for over 30 years, yet we still do not have reproducible SERS structures that can reliably reproduce these exciting results. The SERS enhancement is a nanoscale electromagnetic effect associated with localized surface plasma waves confined by sub-wavelength composite, metal-dielectric structures; the difficulties have been in fabricating samples and in maintaining their SERS properties under environmental assault (chemical contamination).

Recently there has been considerable activity on nano-antennas particularly associated with semiconductor lasers for producing intense, near-field, sub-wavelength resolution sources [Cubukcu *et al.* 2006, Rao *et al*. 2007]. Magnetic storage is a specific, large-scale application that is driving much of this activity, since the available storage density is directly related to the available laser spot size (the reason blu-ray disks hold more information than conventional, red-laser-based, DVD optical media). This work has grown out of the observation of enhanced transmission through an array of sub-wavelength apertures in a metal film [Ebbesen *et al*. 1998] that has led to extensive research efforts at both understanding and applying this phenomenon [Coe *et al. 2*008]. The general picture that has emerged is that the periodic hole array allows coupling (phase-matching) between incident radiation and surface plasmon waves that propagate along the metal film (either top or bottom surface). The transmission is also impacted by

coupling to the localized modes of the holes. Surface plasma waves inherently have larger wave vectors than the incident plane waves and so can be applied to sub-wavelength imaging. Near the cut-off temporal frequency for the surface plasmon waves, this compression can be large and offers the possibility of strongly enhanced resolution [Vedantam *et al. 2*009]. Semiconductor lasers with nano-antennas employ related phenomena to concentrate the laser output in a sub-wavelength spot.

Metamaterials are novel, man-made, sub-wavelength nanostructures that offer optical properties not available from natural materials and have generated enormous interest recently [Engheta and Ziolkowski 2006, Cai and Shalaev 2009]. A great deal of attention has been paid to the possibility, and realization, of negative permeability (negative μ) and of related negative-index materials (NIM) with both negative permeability and negative permittivity (Re $\mu < 0$ and Re $\varepsilon < 0$) [Shalaev 2007] (so far to wavelengths as short as the near-IR, but not into the visible due to the poorer visible optical properties of metals). Much of this scientific excitement has been driven by the possibility of NIM-based "perfect lenses" made from NIM that operate without any transverse spatial-frequency band pass limitation [Pendry 2000]. This improved resolution is necessarily restricted to near-field domains for flat lenses and is limited by materials, fabrication and impedance-matching constraints [Smith *et al. 2*003].

Related hyperlenses, which take advantage of non-planar metamaterial/plasmonic variations to generate magnification and thus to convert the evanescent fields at the object to propagating fields at the image, have demonstrated resolution to ~ $\lambda/3$ [Liu *et al.* 2007, Lee *et al. 2*007] and to $\lambda/7$ [Smolyaninov *et al*. 2007]. The geometric constraints associated with the hyperlens severely restrict the field-of-view, to date to only a few

times the resolution. In the case of a 2D, planar, hyperlens structure [Smolyaninov *et al*. *2*007] the image is necessarily restricted to a 1D line image. To date, these are exciting initial scientific demonstrations, but not routine techniques for large-area microscopic investigations.

1.5.7 Digital Holography

Digital holography is a promising method for overcoming the conventional microscopy resolution limit. Digital holography allows reconstruction of both the amplitude and the phase of imaged objects. The scattered light from the sample is mixed in the Fourier plane with a reference wave. Of course, the diffracted orders have to propagate to the detection plane, which limits the resolution to $>\lambda/4$. The resulting hologram is recorded with a CCD camera; then the object wavefront is reconstructed numerically using the Kirchhoff–Fresnel propagation equations [Haddad *et al*. 1992, Schnars and Jüpter 1994, Grilli *et al*. 2001, Schnars 1994]. Phase-shifting digital holography (PSDH) uses a series of images with a variation of the phase of the reference beam to obtain the complex amplitude at the plane of the CCD [Yamaguchi and Zhang 1997, Guo and Devaney 2004, Decker *et al*. 1978]. PSDH has also been used for three-dimensional microscopy [Yamaguchi *et al*. 2001, Zhang and Yamaguchi 1998], encryption [Lai and Neifeld 2000], and wavefront reconstruction [Lai King and Neifeld 2000].

1.6 Synthetic aperture approaches

A significant resolution improvement is obtained using holographic synthetic aperture methods. This is often referred to as “superresolution,” which is a bit of a misnomer. The

resolution is indeed better than that provided by the generalized Rayleigh (or any other) criteria, but this is the result of effectively stitching together an effective pupil aperture that is larger than the physical *NA*, as will be described below; within this new larger aperture the standard resolution constraints apply. The synthetic aperture can be as large as 2 in air and 2*n* in an immersion medium, in the normalized units ($2\pi/\lambda$) defined above, with corresponding Abbe half-pitch limits of $\lambda/4$ and $\lambda/4n$, independent of the NA (cf. Eq. 1.5).

As an analogue to Synthetic Aperture Radar (SAR), the holographic synthetic aperture methods are based on the generation of a synthetic aperture by combining different sub-images recorded at different camera positions to construct a larger digital hologram [LeClerc *et al*. 2001, Massig 2002]. The resolution improvement increases with the number of recorded sub-images, as long as each sub-image covers additional (and exclusive) portions of the available spatial frequency space [Zalevsky and Mendlovic 2002, Zalevsky *et al*. 1999, Toraldo di Francia 1955, Toraldo di Francia 1969, Cox and Sheppard 1986, Lukosz 1967, Shemer *et al*. 1999, Sun and Leith 1992, Françon 1952, Lohmann and Parish 1964, Zlotnik *et al*. 2005, Kartashev 1960]. The basis of super-resolution is to produce a synthetic enlargement in the system aperture without changing the physical dimensions of the lens or the illumination wavelength [Toraldo di Francia 1955, Shemer *et al*. 1999, Sun and Leith 1992]. Many approaches are based on a certain *a-priori* knowledge about the object, such as its time independence [Shemer *et al*. 1999, Sun and Leith 1992, Françon 1952], polarization independence [Lohmann and Parish 1964, Zlotnik *et al. 2*005], or/and wavelength independence [Kartashev 1960] allowing additional information to be accessed. All of these parameters are involved in information

capacity theory [Toraldo di Francia 1955, Toraldo di Francia 1969, Cox and Sheppard 1986], which gives an invariance theorem for the number of degrees of freedom of an optical system. This theorem states that it is not the spatial bandwidth but the information capacity of an imaging system that remains constant. Thus, it is possible to extend the spatial bandwidth by encoding or decoding the additional information onto unused parameters of the imaging system. As examples, time independence of the object allows for sequential recording of sub-images with different optical configurations and polarization independence allows for simultaneous recording of sub-images with orthogonal polarizations and complementary frequency space coverage.

1.7 Development and advantages of imaging interferometric microscopy

Imaging interferometric microscopy (IIM) allows resolution to the linear systems limit of a half-pitch of $\lambda/4$ in air. A related concept had been introduced earlier for lithographic image formation (imaging interferometric lithography or IIL) [Chen and Brueck 1999, Chen and Brueck 1998, Brueck and Chen 1999, Smolev *et al*. 2006]. A natural approach was to apply some of the techniques invented for higher resolution lithography to high-resolution measurement tools [Schwarz *et al*. 2003].

Subsequent to the initial publication of the IIM concept [Schwarz *et al*. 2003)], Alexandrov *et al.* [2005, 2006] introduced an alternate, but related, concept wherein the images were recorded directly in the Fourier plane. This procedure can increase the system information capacity for a given camera, but also leads to ambiguity of phase determination and possible information loss for highly periodic images due to the restricted dynamic range of the CCD camera. In order to determine the correct phase for

image reconstruction it is necessary to have a reference object, which is impossible in this case. In more recent reports [Alexandrov *et al*. 2007, Hillman *et al*. 2009] the recording camera is shifted away from the Fourier plane (defocused) to increase the available dynamic range of the recorded intensities. Multiple images (90) were recorded with image rotation in order to extract phase information from overlapped images and the *NA* was increased from 0.13 to 0.61. An alternate system based on illumination with multiple wavelength sources to cover different regions of frequency space was introduced [Alexandrov and Sampson 2008].

The experiment described in ref. [Schwarz *et al*. 2003] was reproduced at a wavelength of 532 nm by Price *et al*. [2007] with a 100x objective (*NA*=0.59) to show an improvement in the effective numerical aperture from 0.59 to 0.78 and by Mico *et al*. [2007] with NA_{low} = 0.14 extended to NA_{eff} = 0.45. With a setup similar to that of Schwarz [2003], a vertical cavity surface-emitting laser (VCSEL) array was used as a source of light for the off-axis illumination, providing a simple optical system that is switched by either turning on individual VCSELs or by relying on their mutual incoherence to record all of the offset images in a single step [Micó *et al*. 2004, Micó *et al*. 2006a, Micó *et al*. 2006b]. In the initial paper [Micó *et al*. 2004], the authors used five sources simultaneously to increase the system spatial frequency bandwidth. Later, Mico *et al.* [2006a] extended the optical system of initial work [Micó *et al. 2*004] for two-dimensional (2D) objects. The recording process is by interference of each frequency band with a complementary set of reference plane waves in parallel. The benefit of this system is improved modulation speed, which leads to more rapid image synthesis. Moreover, any desired synthetic coherent transfer function can be realized at fast rates by

changing the electrical drive of the VCSEL array. However, the holograms for the different band passes are incorrectly overlapped, and so the combined image is distorted; this could be resolved by designing the laser array to match specifically to the optical system. Other authors have implemented spatially incoherent illumination sources for a continuum of independent off-axis illuminations, along with a pinhole in the pupil plane for blocking the dark field, to increase the resolution by incoherent-to-coherent conversion (MTF to ETF) with maximum achievable effective aperture of unity [Leith *et al*. 1987, Leith 1990].

Another method uses a collection of mutually incoherent point sources at different lateral positions to provide tilted, spherical-wave illuminations for the object, since every point source gives a spherical wave with a different origin [Micó *et al*. 2006c]. In this case, the input object was illuminated at off-axis illumination angles higher than the *NA* of the microscope objective [Micó *et al*. 2006c, Sheppard and Hegedus 1998]. In this way a resolution improvement by a factor of 3 was shown to be achievable using off-axis illumination with a maximum illumination angle equal to the *NA* of the imaging lens. The angle of illumination is limited by $NA_1 + NA_2$, where NA_1 is the numerical aperture of the optical elements between the VCSEL and a sample, and NA_2 is the numerical aperture of the imaging system. In later experiments [Micó *et al*. 2008, Granero *et al.* 2009], a grating near the Fourier plane was moved during image acquisition for phase recovery. In following papers, they discussed the possibility of axial resolution, showing an example of 3D images of swine sperm [Micó *et al*. 2008a, Micó *et al*. 2008b].

Interferometric Synthetic Aperture Microscopy (ISAM) [Tyler *et al.* 2007, Tyler *et al.* 2008, Davis *et al.* 2008] is aimed at increasing the 3D volume of the image beyond

the traditional depth-of-field, rather than increasing the transverse resolution. In ISAM, a sample is illuminated by a series of femtosecond laser pulses that make a point-by-point scan of a transverse plane. The scattered field interferes with an original pulse and is dispersed by a grating. The resultant spectral content is used to compute the contribution from various depths. This way, longitudinal information from the 3D image is extracted without mechanical refocusing. The axial resolution comes from the low coherence length of the short pulse, which only allows interference when the path lengths of the sample and reference beams are matched in length.

1.8 Overview of our achievements and directions of future development for IIM.

Our group has well established history of working on the problem of higher resolution using IIM technique. The initial demonstration of advantages of off-axis illumination was done by Schwarz *et al.* [2003]. Later Kuznetsova, Neumann and Brueck [2007] significantly increased the scale of the synthetic aperture by using multiple off-axis illumination which required development of filtering algorithms and procedures for multiple sub-image phase correction. Then we achieved resolution limit of aerial linear optical systems in far-field (NA ~ 1) by tilting an objective plane and restoration of images using developed algorithms [Kuznetsova *et al.* 2008]. Further enhancement in resolution was achieved by solid immersion techniques [Neumann *et al.* 2008b]. Radical modification of the scheme of reference beam reinjection demonstrated advantages of structural illumination eliminating the need for an extended interferometer encompassing the objective lens [Neumann *et al.* 2008a]. We developed phase correction algorithms which are required for the full-immersion extension [Kuznetsova *et al.* 2012]. All these

techniques along with experimental demonstrations are described in Chapter 2.

Chapter 3 contains conclusions and ideas for future work, such as using materials with high refractive indices, enhancements in hardware and in algorithms and technique for 3D imaging.

Chapter 2. Imaging Interferometric Microscopy

IIM allows one to resolve structures not accessible in a conventional illumination setup, while using a low *NA* microscope objective and thus keeping the large working distance, depth of focus and field of view associated with the lower *NA*. The goal of this dissertation was to extend optical resolution limits by application of synthetic aperture and solid immersion technique to imaging interferometric microscopy as well as to provide robust algorithm for image reconstruction. An off-axis, interferometric arrangement allowed us to take on-axis and off-axis illumination sub-images. A single mode fiber was used to deliver the reference beam around the lens to the Fourier plane to interfere with the diffracted image orders. As we show below, this concept can extend the IIM resolution to the linear systems limits of optics, to spatial frequencies of $2k_0$ in air and $2nk_0$ in a medium of refractive index n. In the same sense as the Abbe limit, these limits correspond to the highest spatial frequency terms that can propagate through the respective media. Any higher resolution information corresponds to near fields and demands close proximity ($<<\lambda$) to the object.

2.1 Initial configuration and optical arrangement for IIM

As was shown above (Fig. 1.3), it is possible to increase the effective *NA* using off-axis illumination to capture the second order scattering information, E_2; it was important in that example to pass the E_0 component through the lens as well. This sets an upper limit on the off-axis illumination angle. With larger tilt angles of the illumination beam (extreme off-axis illumination, where the extreme refers to the fact that the zero-order

beam is outside the lens *NA)*, higher order information can be passed through the lens. As discussed above, this is one approach to dark-field illumination. In the IIM configuration, a zero-order beam is reintroduced at the image plane using additional optics to provide the appropriate divergence, amplitude, phase and angle of incidence for image formation (Fig. 2.1(a)). Frequency space coverage for this case is shown in Fig. 2.1(b). Effectively this involves constructing a Mach-Zehnder interferometer with the objective inserted in one arm of the interferometer. The optics are arranged to provide the same characteristics of the zero-order (reference) beam that would have been available if the lens NA were sufficiently large to collect it directly. If the illumination angle is such that the higher

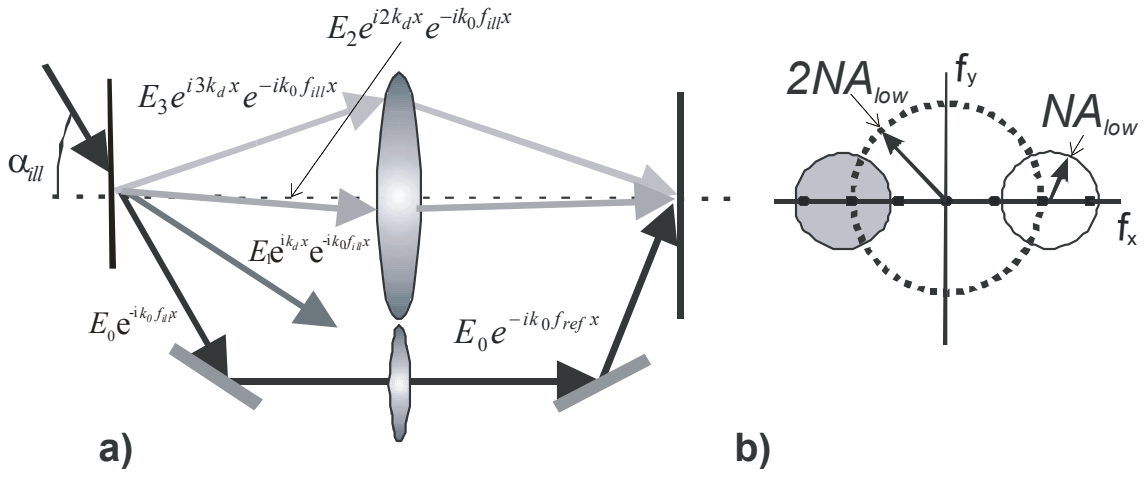

Fig. 2.1. a) High-frequency imaging setup. The extreme off-axis illumination allows the high orders to be transmitted through the lens and interfere with the zero order that is passed around the lens, b) Frequency space coverage: gray circles=high frequency images, dashed circle=dark field.

terms E_2 and E_3 are collected, and a reference beam is added with additional optics, the intensity in the image plane is:

$$
\begin{aligned}
I_{high} &= \left| E_0 e^{-ik_o f_{ref} x} + E_2 e^{i(2k_d - k_0 f_{ill})x} + E_3 e^{i(3k_d - k_0 f_{ill})x} \right|^2 \\
&= |E_0|^2 + |E_2|^2 + |E_3|^2 + 2|E_0 E_2| \cos\left\{ \left[2k_d - k_0 \left(f_{ill} - f_{ref} \right) \right] x + \varphi_2 \right\} \\
&+ 2|E_0 E_3| \cos\left\{ \left[3k_d - k_0 \left(f_{ill} - f_{ref} \right) \right] x + \varphi_3 \right\} + 2|E_1 E_2| \cos\left\{ \left[k_d - k_0 \left(f_{ill} - f_{ref} \right) \right] x + \varphi_2 - \varphi_1 \right\}
\end{aligned}
\quad , \quad (2.1)
$$

where $f_{ill} \equiv \sin\alpha_{ill}$ is the normalized frequency shift due to the inclined illumination (high frequencies are shifted by the inclined illumination and are captured by the lens), and f_{ref} is the normalized frequency shift due to reference beam inclination (which shifts the frequencies back to their original values). The φ's are the respective phases of the diffracted beams. The incident angle of the reference beam is adjusted so that $f_{ref} = f_{ill}$, so that these offsets cancel in the sub-image:

$$
\begin{aligned}
I_{high} &= \left| E_0 e^{-ik_0 f_{ref} x} + E_2 e^{i(2k_d - k_0 f_{ill})x} + E_3 e^{i(3k_d - k_0 f_{ill})x} \right|^2 \\
&= |E_0|^2 + |E_2|^2 + |E_3|^2 + 2|E_2 E_3| \cos\left(k_d x + \varphi_3 - \varphi_2 \right). \\
&+ 2|E_0 E_2| \cos\left(2k_d x + \varphi_2 \right) + 2|E_0 E_3| \cos\left(3k_d x + \varphi_3 \right)
\end{aligned}
\quad (2.2)
$$

The corresponding frequencies are shown by the black dots in Fig. 2.1(b); high frequency space coverage for this case is represented by the gray circle, while the dashed circle corresponds to the dark field region and the black dots correspond to grating frequencies. Notice that as a result of the extreme off-axis illumination, the frequency content now extends beyond the 2*NA* limit set by the optical system. Thus the synthetic aperture can be extended beyond the limits set by the optics in the Rayleigh/Abbe sense. However, the low frequencies, and in particular the E_1 term, are missing. This is a high frequency sub-image; combining it appropriately with a normal-incidence-illumination (low-frequency) image provides a more complete representation of the object.

IIM is based on the incoherent (intensity) addition of several coherent sub-images.

Combining the two sub-images from normal incidence and off-axis illumination (Figs. 1.2 and 2.1, respectively) results in the following response, which consists of a spatially constant base line, an image part and a dark field (Eq. 2.2). The intensity of the high frequency image has been multiplied by two to compensate for the collection of only a single sideband. The off-axis dark field is easily measured by blocking the reference beam and is subtracted from the off-axis sub-image before combining with the low frequency sub-image:

$$\begin{aligned} I_{total} = I_{low} + 2(I_{high} - I_{high,dark}) = 3|E_0|^2 + 2|E_1|^2 + 4|E_0E_1|\cos(k_d x + \varphi_1) \\ + \left[4|E_0E_2|\cos(2k_d x + \varphi_2) + 2|E_1|^2\cos(2k_d x + 2\varphi_1)\right]. \\ + 4|E_0E_3|\cos(3k_d x + \varphi_3) \end{aligned} \quad (2.3)$$

Again, this is a single sideband system; the sideband not collected by the optical system is restored as a result of the square law intensity response. Clearly, in this simple case it is possible by measuring the spatial frequencies, intensities and phases, to reconstruct the image (e. g. to determine d, E_0, E_1, E_2 and E_3). However, the reference beam in our experimental setup is transmitted around the lens, so it has an arbitrary amplitude and phase. So more precisely, the intensity distribution of the high frequency image is (setting $f_{ref} = f_{ill}$):

$$\begin{aligned} I_{high} = \left|AE_0e^{-i\varphi_{ref}}e^{-ik_0f_{ref}x} + E_2e^{i(2k_dx+\varphi_2)}e^{-ik_0f_{ill}x} + E_3e^{i(3k_dx+\varphi_3)}e^{-ik_0f_{ill}x}\right|^2 = |AE_0|^2 + |E_2|^2 \\ + |E_3|^2 + 2|AE_0E_2|\cos(2k_dx - \varphi_{ref} + \varphi_2) + 2|AE_0E_3|\cos(3k_dx - \varphi_{ref} + \varphi_3) \end{aligned}, \quad (2.4)$$

where A is a reference attenuation factor, φ_{ref} is the arbitrary phase shift of the reference beam, and φ_i is the phase of the corresponding high frequency beam. Using a reference object and adjusting the phase of the reference beam by adjusting the length of the

reference optical path, the system can be adjusted in such a way that $\varphi_{ref} = 0$ in order to match the phases (e. g. x-positions) of the low and high frequency sub-images. Neutral density filters are used to adjust A so that $|E_0| \sim |E_2|$ in order to have the maximum image contrast (optimum signal-noise ratio). Then the intensities of the sub-images are adjusted electronically by comparing with the reference object. The net result is a resolution corresponding to a larger NA lens. For example, an optical system with He-Ne laser illumination (633 nm) and with an $NA_{low} = 0.4$ objective acts as a low pass filter that limits the frequency space to a maximum frequency corresponding to a half-pitch of ~790 nm ($\lambda/2NA_{low}$). The resolution can be improved by using extreme off-axis illumination, providing an effective NA ($NA_{eff} = 3NA_{low}$) as discussed above. If the illumination offset is chosen at $2NA$ to provide continuous coverage along the x-axis, the effective $NA_{eff} = 3NA_{low}$, and the half-pitch resolution is enhanced to 263 nm. The zero-order transmission is shifted outside of the imaging pupil plane, with the additional interferometric reintroduction of the zero-order beam to the Fourier plane on the low-NA side of the lens in order to restore the original frequencies. A schematic of the experiment is shown in Fig. 2.2(a). The incident angle of the zero-order α_{ref} is adjusted such that the spectral content is shifted back to the original high frequencies. Changing α_{ill} together with α_{ref} leads to different frequency coverage. A rotation stage can be used to extend the azimuthal coverage across the f_x, f_y plane.

The possible frequency space coverage is shown in Fig. 2.2(b), where the circle in the middle represents the low frequency image and the circles on the sides represent high frequency images. The circles along coordinate axes contain information about features

oriented along the major axes. We need additional coverage in between axes for arbitrary structures (yellow circles are shown as an example in Fig. 2.2(b)). The Fourier transform is symmetric, to the extent that the object is phase-invariant (a thin object <<λ). As noted above, the imaging is single side-band; the square law (intensity) response of the image formation process restores the conjugate frequency space components, resulting in the two symmetric circles in Fig. 2.2(b) for each sub-image. As before, it is possible to restore telecentricity by combining sub-images from opposing tilt angles in pairs.

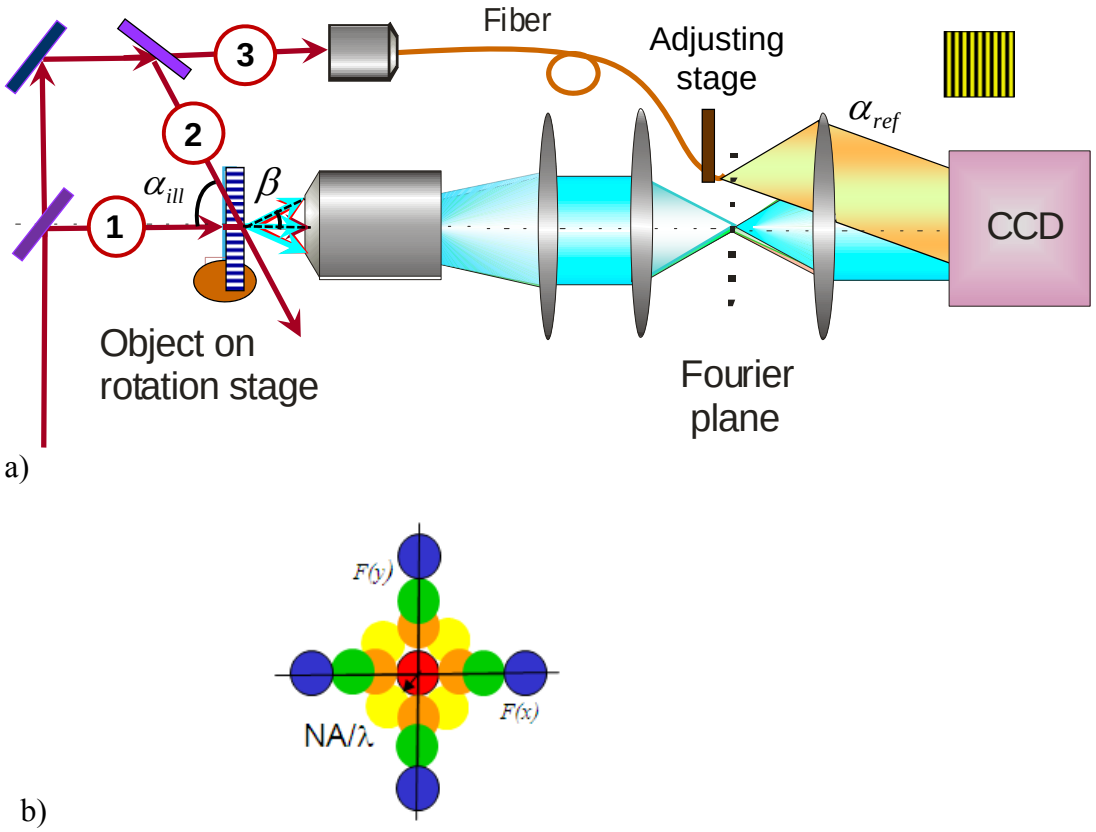

Fig. 2.2. a) Optical arrangement for imaging interferometric microscopy: $\beta = \sin^{-1}(NA)$, α_{ill} is the illumination beam angle, and α_{ref} is the angle of the reference beam relative to the image plane,

b) Frequency space coverage for an experiment with 5 sub-images.

Beam 1 in Fig. 2.2(a) (2 and 3 are blocked) is used for on-axis illumination. Beams 2 (extreme off-axis illumination) and 3 (reference) when 1 is blocked are used for high-frequency sub-images. It is convenient to use a single-mode fiber for beam 3 to simplify the optical arrangement and provide a clean reference beam. The exit aperture of the fiber is placed in the pupil of the imaging optics; the position of the fiber sets f_{ref} and the path length sets φ_{ref}. There is a requirement that the optical length of path 3 be the same as that of path 2 combined with the collection optical path length to within the source longitudinal coherence length. For the long-coherence-length HeNe laser used in the demonstration experiments, this requirement is easy to realize. For a shorter coherence length source, care is necessary to ensure that this condition is met. The dark fields and the background/reference images should be subtracted from the stored high-frequency image in order to get the high-frequency image with only the imaging contribution (interference between zero-order and diffraction beams). Thus, the effective numerical aperture is extended to $3NA$.

We use a Manhattan structure (x, y) object (Fig. 2.3 (a)) as an example to show the possibility of tiling frequency space and reconstructing the object. The resulting frequency coverage for this structure with lines of width 500 nm is shown in Fig. 2.3(b). If we use a NA = 0.4 objective and a He-Ne laser (λ =633 nm) the circles in the center correspond to the spatial frequencies 0.4 and 0.8 normalized to k_0, for coherent and incoherent illumination, respectively (Section 1.3.2), which define the range of possible captured frequencies by conventional illumination. The spatial frequency 0.8 also corresponds to the dark field. The set of shifted circles of radius NA_{low} = 0.4 for the case when α_{ill}=53° extends the radius to $3NA$ = 1.2 in the x- and y-directions or a minimum

resolution half pitch of ~260 nm [Schwarz *et al.* 2003].

Additional frequency space coverage is available with a second pair of off-axis sub-images, represented by the outer set of shifted circles (Fig. 2.3(c)), with a larger tilt of the illumination plane wave, approaching grazing incidence. The maximum frequency coverage (as follows from Eq. 1.5) extends to $1+NA = 1.4$. However, in corresponding experiments the inclination angle was limited to 80° [sin(80°) = 0.98] to the object plane due to high reflectivity from substrate at steeper angles and increasing wave front distortion associated with substrate thickness variations, so the experimental extension was to $0.98+NA = 1.38$ which allowed resolution of a Manhattan structure with lines of 240-nm width using the same $NA = 0.4$ objective (Fig. 2.3(c)). Clearly, the frequency-space coverage of the outer circles captures the fundamental frequency components of the image [Schwarz *et al.* 2003]. The problem of frequency coverage overlap can be solved by filtering images either optically with apertures in the Fourier plane or electronically by taking Fourier transforms of the sub-images, appropriately filtering, and retransforming.

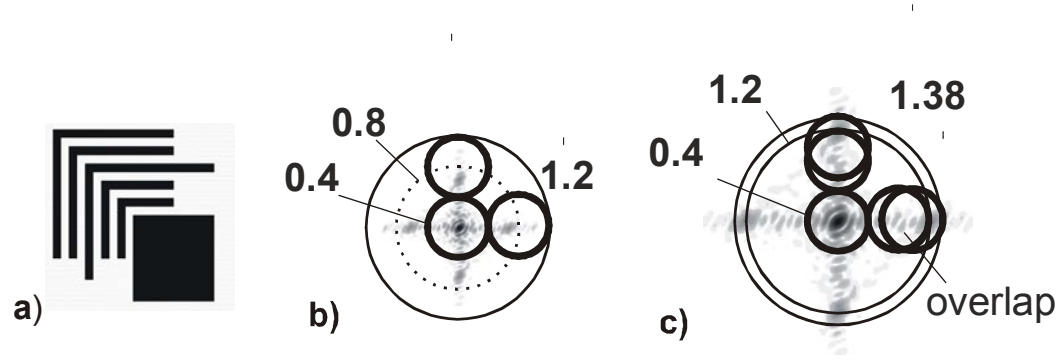

Fig. 2.3. a) Manhattan geometry pattern used for image resolution exploration consisting of five nested "ells" and a large box. b) Intensity Fourier space components of the pattern, mapped onto the frequency space coverage of the imaging system. Lines and spaces of the "ells" are 500 nm. c) Lines and spaces of the "ells" are 240 nm.

For some sample structures with a frequency peak at the edge of the collection limit some higher frequency sidebands of the image are not collected, which causes distortions, such as extra features arising from a hard cut-off in frequency space due to the Gibbs effect [Smith 2007]. This effect can be reduced by apodized filters [Tridhavee *et al.* 2005] applied in the physical Fourier plane or electronically.

The reference beam in the experimental set-up is transmitted around the lens, so it has an arbitrary amplitude and phase, which has to be adjusted according to the formula (2.4). A reference object is required to assist in setting the angle, amplitude and phase of the reference beam. This object should be as close as possible to the object being imaged. In our initial demonstrations, where we knew *a priori* the object, we used the known object as a self-reference. For higher contrast it is important to choose the object position in such a way that the polarization is parallel to the main image features in each image (TE polarization) [Nesterov and Niziev 2005].

The experimental results with a Manhattan geometry structure (line width 500 nm) and a He-Ne laser used for illumination are shown in Fig. 2.4. The low frequency image after dark field and background subtraction, and after filtering is shown in Fig. 2.4(a). The individual nested-ell lines are not resolved. The off-axis illumination sub-image of the horizontal features after the same subtraction procedure is shown in Fig. 2.4(b); the vertical features are similar. The reconstructed image obtained by adding the three images is shown in Fig. 2.4(c). The image taken using a conventional microscope with incoherent white light and NA=0.9 is shown in Fig. 2.4(d). Note that the extra features appearing at the bottom of horizontal lines are due to corrosion and lifting of the chrome features. This demonstrates that IIM is indeed imaging arbitrary structures and is

not limited to simple geometries.

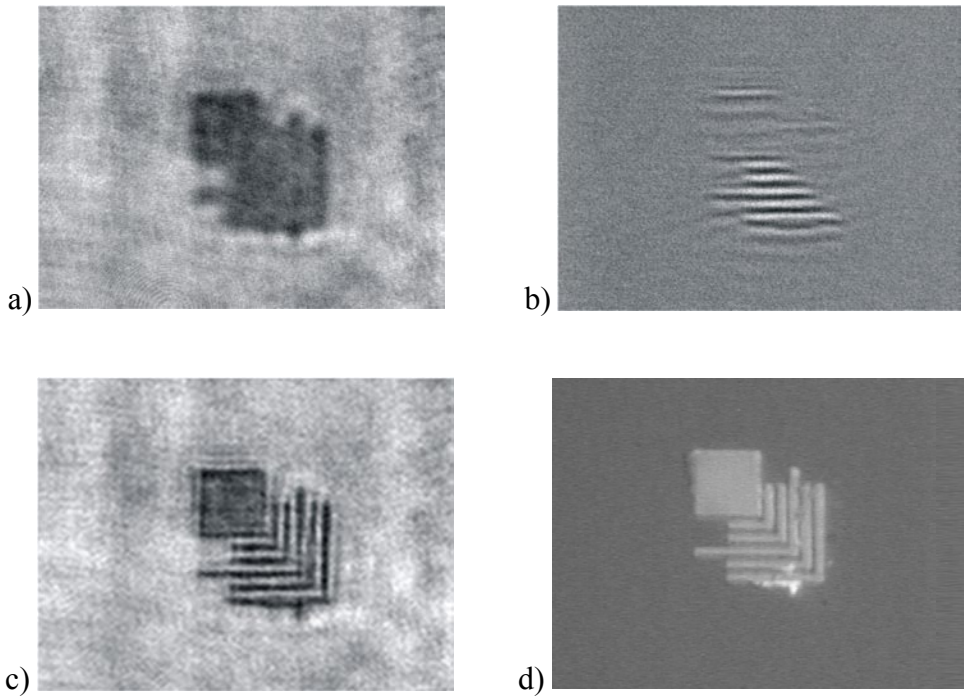

Fig.2.4. a) On-axis image after dark-field and background subtraction, b) high-frequency image of horizontal structures after dark-field and reference image subtraction, c) filtered reconstructed image, d) image taken by a conventional incoherent-illumination microscope with *NA* = 0.9. Reprinted from Schwartz *et al.* 2003.

A major advantage of imaging interferometric microscopy (IIM) compared with imaging interferometric lithography (IIL) is that the partial images can be electronically manipulated, whereas in the lithography case the images are chemically stored in the photoresist and are not individually accessible. This relates back to the major trends identified in the introduction, particularly the availability of high pixel count digital imaging sensors and the high speed computation necessary for manipulating the image information.

2.2 Concepts associated with a tilted object plane

Off-axis illumination allows an increase in NA_{eff} to (1+NA) with the optical axis normal to the object plane (position *a* in Fig. 2.5), but there is additional higher frequency (larger angle) scattering to the side of the objective towards the incident, off-axis beam. This information can be captured by tilting the object plane or equivalently, tilting the objective (shown as the offset objective at position *b* in Fig. 2.5) [Kuznetsova *et al.* 2007, 2008]. Notice that for offset in frequency space by more than 3NA there is a separation between the imaging terms and the dark field terms, which are limited to spatial frequencies less than 2NA. So, the dark-field terms are easily removed electronically by taking the Fourier transform of the sub-image, filtering appropriately in spatial frequency space and transforming back to real space.

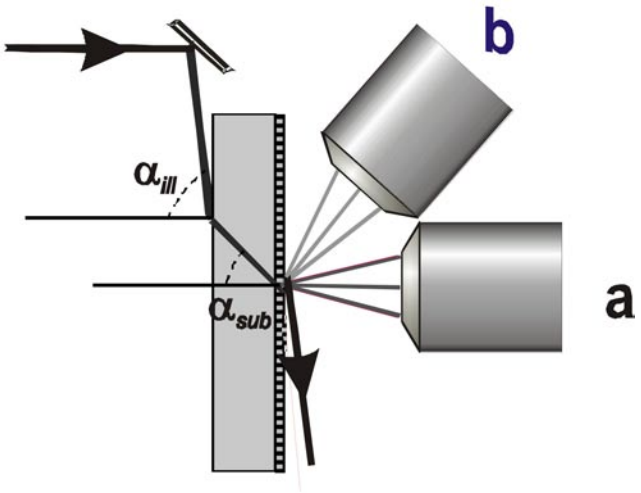

Fig. 2.5. Optical arrangement using a) off-axis illumination, b) off-axis illumination and tilted object to enhance the frequency space information.

In order to obtain an effective aperture for this case we have to add the object plane tilt

angle θ_{tilt} to the angle corresponding to the objective *NA* in equation (1.6). The modified formula is:

$$NA_{eff} = \sin\left(\sin^{-1}(NA) + \theta_{tilt}\right) + \sin\left(\alpha_{ill}\right). \tag{2.5}$$

The highest possible spatial frequencies (~ 2/λ) are captured with a grazing incidence illumination and with an object plane tilt of $\pi/2 - \sin^{-1}NA$ (~ 66.42° for *NA*=0.4), but the constraints of the optical system, both physical and optical (aberrations), restrict the tilt and thus limit the frequency-space coverage to slightly less than 2/λ. As a result of the non-paraxial optical system, the extent (minimum to maximum spatial frequency) of the captured frequency range in the direction along the tilt decreases as the tilt increases. In the orthogonal direction the range is invariant to the tilt, so the covered frequency region becomes elliptical rather than circular.

An example of frequency space coverage using a *NA* = 0.4 objective, tilt ~ 39° and an incident beam angle tilt of 80° with respect to the normal to the object plane is shown in Fig. 2.6 superimposed on the frequency space intensity plot for an object with 180-nm lines with the same structure as shown in Fig. 2.3(a). In this case, the second pair

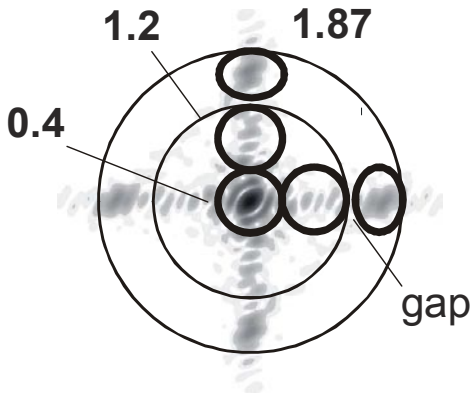

Fig. 2.6. Frequency space coverage with a tilted objective.

of off-axis exposures with the object tilted extends the frequency space coverage out to ~1.87. An image restoration procedure is required to adjust the measured spatial frequencies from the laboratory frame (tilted main optical axis) to the normal image frame for full-image reconstruction. There is a small gap of ~3% of frequency space between the inner circles and outer ellipses. So, the optimum *NA* to cover the frequency space with two offset images and 39° tilt would be ~0.415, but it is worthwhile investigating other combinations of *NA* and tilting angles for optimum results.

Tilting decreases the field of view from the perspective of geometric optics because only a small portion of the image is in focus. However, this is a consequence of the optical system, and can be addressed by the spatial frequency correction as discussed below.

2.3 Impact of conical diffraction on IIM

Intuitive understanding of grating diffraction starts from consideration of a plane that contains the grating wave vector and the surface normal. For example, for normal incidence illumination, the diffraction orders are observed in this plane to the sides of the transmitted (reflected) beam in accordance with the grating equation (*e.g.* $k_{x,j} = \frac{2\pi}{d} j; k_y = 0; \text{and } k_{z,j} = \sqrt{k_0^2 - k_{x,j}^2}$). For an off-axis illumination in that plane, the variations in $k_{z,j}$ are not apparent in the image and the diffraction order spots (e.g. beams corresponding to the diffraction orders) are separated by $\sin(k_{x,j}/k_0)L$. Here d is the period of the grating, j is the diffraction order, and L is the distance from the object to the image plane. For off-axis illumination in the k_y direction, the diffraction spot positions again are not affected, and determination of its positions is straightforward with calculating of the

vectors $k_{x,j}$ and k_{y0} ($k_{x,j} = \frac{2\pi}{d} j; k_y = k_{y0}$; and $k_{z,j} = \sqrt{k_0^2 - k_{x,j}^2 - k_{y0}^2}$).

However, if the observation plane normal is tilted away from the object normal in the *x,z* plane (Fig. 2.7), the spot position becomes dependent on $k_{z,j}$. This is known as conical diffraction since the multiple diffraction spots describe a conic section in the *x*', *z*' plane. Analysis of this case shows that imaging with a tilted object plane (in the *x*-*z* plane) can be extended to the general conical diffraction case, since the tilt couples the *z*-component of propagation vector into the observed frequency position in the pupil plane. Thus, in biaxial imaging system, the image frequencies are shifted from their original positions and they need to be reseted for proper representation of image.

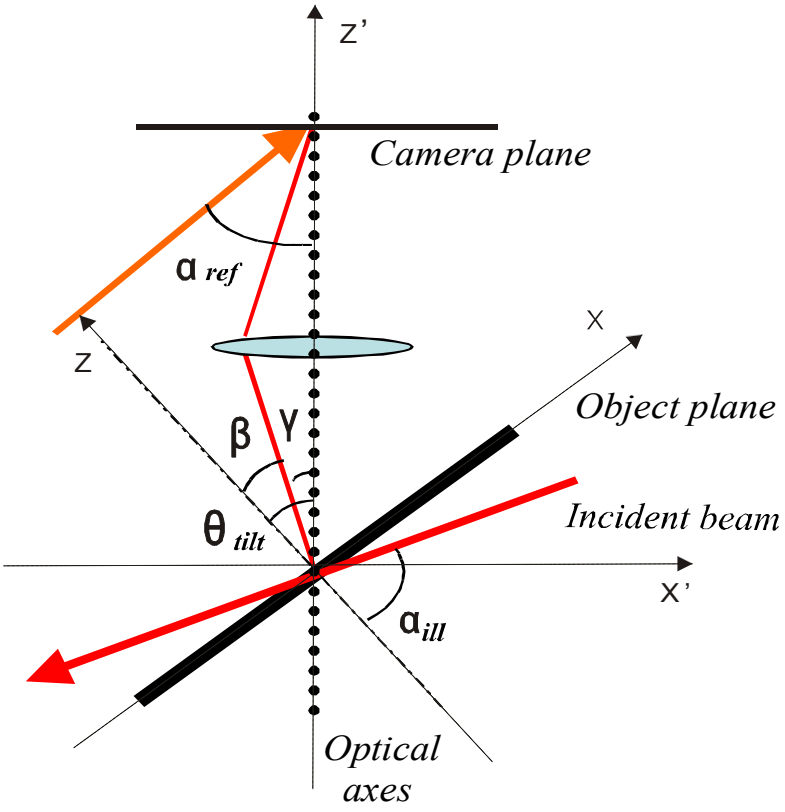

Fig. 2.7. Optical arraignment with tilted object and 0-order reintroducing

Using Eq. 2.5 we can reset the displaced frequencies:

$$f_x = (f_{xobs} - f_{ref})\sqrt{1 - f_{tilt}^2} + \sqrt{1 - f_y^2 - (f_{xobs} - f_{ref})^2}\, f_{tilt} + f_{ill}, \tag{2.6}$$

where f_x - frequency in the *x*-direction; f_{xobs} - observed frequency; f_y - frequency in y-direction; $f_{ill} = \sin(\alpha_{ill})$ - angle of illumination; and $f_{tilt} = \sin(\theta_{tilt})$ - angle of the plane tilt. The reference beam is adjusted to a known selected frequency f_{sel} of a reference object, and other frequencies should be recalculated from Eq. 2.6. Here f_{ref} can be obtained from Eq. 2.6 for the case when $f_{xobs} = f_x = f_{sel}$.

$$f_{ref} = \sin\left[\theta_{tilt} - \sin^{-1}(f_{sel} - f_{ill})\right] + f_{sel}. \tag{2.7}$$

The need for this frequency correction is a direct consequence of the non-paraxial effects that map the observed spatial frequencies of the diffracted fields from the object to the image spatial frequencies in a nonlinear fashion. Correcting this distortion also provides restoration of the field of view. This is illustrated in Fig. 2.8, which shows the *x*-offset high frequency partial images of two adjacent test structures (the one on the left is the object with 180-nm line width, while the one on the right is the 170-nm line width test structure; overall each structure is about 20 half pitch wide (3.6 μm) and the separation is 12 μm). Note that these are the high spatial frequencies in the *x*-direction, similar to the high-*y* frequencies of Fig. 2.4(b) but in different direction. The full image of this Manhattan structure is available only upon combining all of the sub-images. The optical system was adjusted so that for the experimental image the smaller (right-hand) structure was approximately in focus while the larger (left-hand) structure was behind the focal plane due to the tilt and substantially blurred. The distorted image (Fig. 2.8(a)) was restored using Eq. 2.3 and shown in Fig. 2.8(b), which is in a good agreement with a

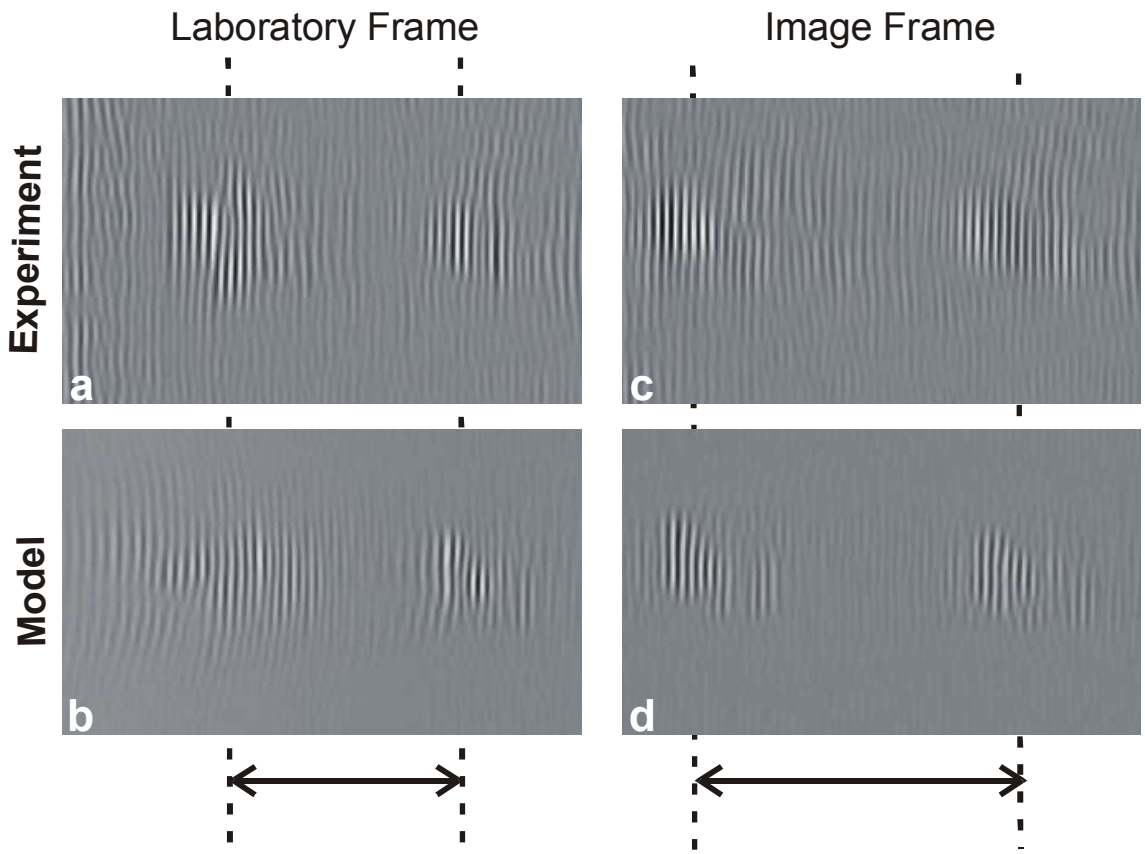

Fig. 2.8: Experimental (a, c) and simulation (b, d) results showing the impact of the frequency restoration on the high frequency partial image. The dotted lines are guides for the eye, showing the significant shift of the out-of-focus object (left) in the laboratory frame.

corresponding model (Fig. 2.8(c,d)). The dotted lines and arrows show the significant shifting of the positions of the intense features accompanying the transformation from the laboratory frame to the image frame and restoring the overall field of view. The final reconstructed images are shown in Fig. 2.9. As expected, the reconstruction procedure restores both images and clearly improves the field of view that was limited by the tilt of the object plane relative to the focal plane. There are also extra features due to the noise in the system, which is magnified during the restoration procedure. This method requires

very precise knowledge of the object tilt and incident illumination offset in order to obtain high-quality, extended-field images.

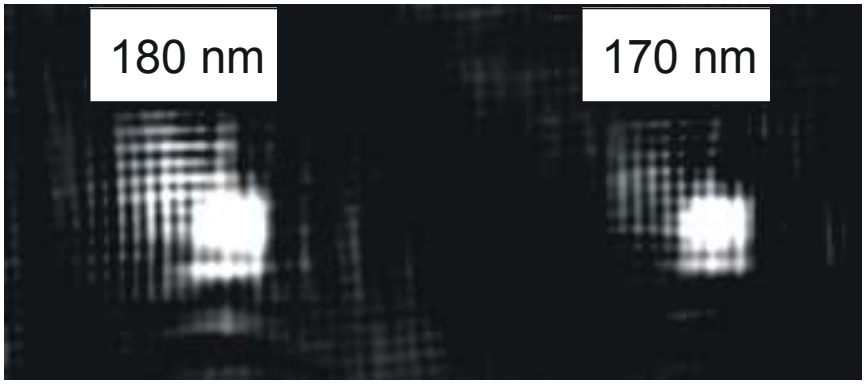

Fig. 2.9. Reconstructed image: 180 nm and 170 nm structures.

2.4 Structured illumination for backward compatibility with existing microscopes

2.4.1 Premises and theoretical adjustments for structured illumination

The implementation of IIM presented above requires an interferometer around the objective lens and access to the back pupil plane (Fig. 2.2(a)). While this is straightforward in an optics laboratory, it is difficult to retrofit to an existing microscope. A structured illumination approach, in which the object is illuminated by two coherent beams, moves the interferometer to the front of the sample [Neumann *et al.* 2008a]. Another method to obtain the same result is to use a zero-order beam reinjected before the objective using a beamsplitter or other optical element (grating).

Both methods provide a frequency offset for all image information transmitted through the low-*NA* objective lens. The result is analogous to the intermediate frequency used in radio frequency communications, the recorded image information is at the low

frequencies allowed by the objective lens. Procedures for extracting the image information and shifting it back to the true image high frequencies are described and proved below.

Two major advantages of this approach are:

a) because reduced or no access is required to the image pupil plane this approach is much more amenable to implementation on existing microscopes, which typically do not allow image pupil plane access without major changing in the optical system, and

b) the recorded images are at low spatial frequencies which reduces resolution requirement for the imaging camera (e. g. a smaller camera pixel count is sufficient as compared with the previous demonstrations).

Another advantage of this method in comparison with conventional IIM is greater phase stability due to the possibility of a much more compact interferometer that no longer has to include the objective lens and other optics, thus eliminating associated source of flare and speckles.

We already discussed conventional IIM with an extreme off-axis illumination beam (extreme is defined as illumination at an angle beyond the *NA* of the objective lens) and a coherent reference beam, equivalent to the zero-order transmission, reinjected into the objective lens Fourier plane using an optical fiber (Fig. 2.10(a)). As it is easily seen, this is equivalent to constructing a Mach-Zehnder interferometer with one arm including the objective lens and requiring access to the image pupil plane. This can be difficult in an existing microscope system where the pupil plane is not generally available and auxiliary optics are required. A second, coherent local-oscillator illumination beam at an offset angle just within the objective *NA* is introduced in addition to the extreme off-axis

illumination to obtain the high frequency partial image (Fig. 2.10(b)) [Neumann *et al.* 2008a]. As seen in the figure, this results in building the interferometer in front of the object where there is more convenient access and shorter path lengths are

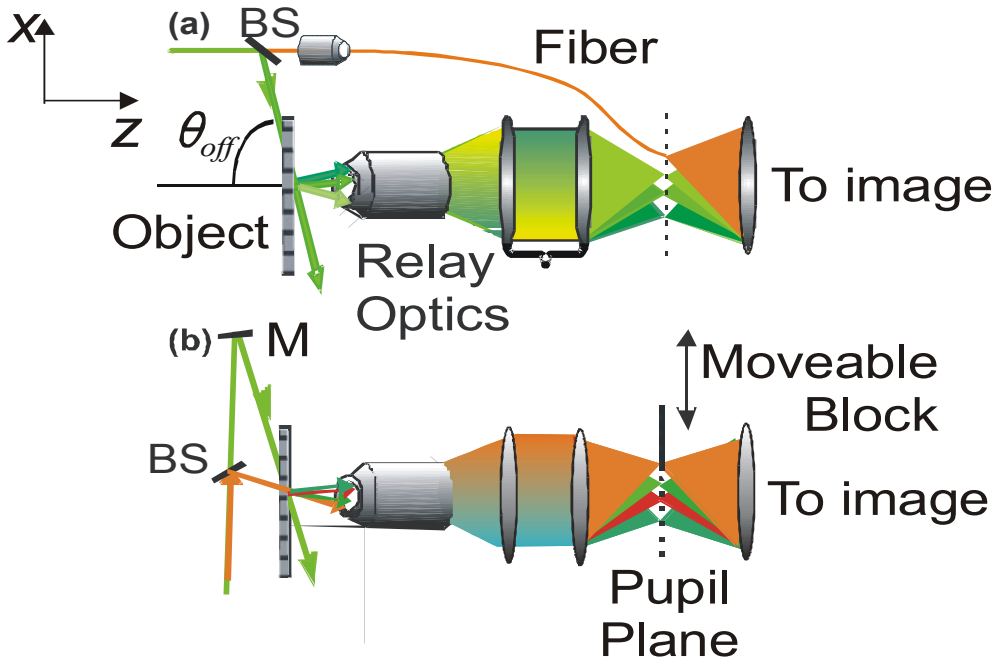

Fig. 2.10. Optical arrangements for (a) conventional IIM with an interferometer that includes the objective lens, and (b) structured illumination with the interferometer in front of the object.

possible. The interference between this local-oscillator beam and beams diffracted from the off-axis illumination beam and passing through the objective provides the high frequency information for the image. However, since the zero-order and the diffracted beams all pass through the low-*NA* objective, the image information is at low frequencies, less then $2NA/\lambda$, e.g. it is in a shifted laboratory frame, and signal processing is necessary to restore the correct image frequencies. In addition, there are dark field terms arising from the interference between the diffracted orders from both illumination beams

that must be eliminated. The optical and signal processing procedures necessary to achieve the final image are discussed below.

Now we begin with a mathematical description, first of the extreme off-axis coherent illumination microscopy image of the previous IIM experiment (Fig. 2.10(a)) [Kuznetsova *et al.* 2007] and then extend this mathematical treatment to the structured illumination experiment. Please note that the previous mathematical description started with Eqs. 1.2-1.5 and continued with Eqs. 1.10 and 2.1-2.4 is a subset of the following mathematical description. The subset, where a certain object with evident Fourier plane features (grating) was chosen, helped to explain working principals of IIM in the most simple and efficient way. In contrast, the following description applies to an arbitrary object. The notations are changed to avoid confusion.

The total transmission through an arbitrary object (assumed to be periodic on large scale to allow Fourier sums rather than Fourier integrals) illuminated by a tilted (off-axis) plane wave is given by:

$$A'_{0,0}\exp\left(-i\omega_{off}x\right)e^{i\gamma_{0,0}^{off}z}+\sum_{k,l\neq 0}T(k\omega_x-\omega_{off};l\omega_y)A_{k,l}\exp\left[ix\left(k\omega_x-\omega_{off}\right)+il\omega_y y\right]e^{i\gamma_{k,l}^{off}z}, \quad (2.8)$$

where *x, y* and *z* are orthogonal spatial coordinates, $\omega_{off}=2\pi\sin\left(\theta_{off}\right)/\lambda$ is the spatial frequency offset arising from the off-axis illumination at angle θ_{off} (assumed in the *x*-direction), the prime on the $A'_{0,0}$ refers to the re-injected 0-order, ω_x, ω_y are the discrete spatial frequency increments of the Fourier summation, $\gamma_{k,l}^{off}\equiv\left[\left(2\pi n/\lambda\right)^2-\left(k\omega_x-\omega_{off}\right)^2-\left(l\omega_y\right)^2\right]^{1/2}$ with *n* being the refractive index of the transmission medium (equal 1 for air), $\{k,l\}$ is the set of integers, for which $\left(\gamma_{k,l}^{off}\right)^2>0$, that is the

range of integers for which the diffracted beams (ω_x , ω_y) are within the band pass of the medium and are propagating in the *z*-direction away from the object. A scalar electromagnetic model is adequate since the *NA* of particular sub-image is relatively modest. For high synthetic aperture and transverse-electric-field-polarized (TE) light the model is still valid. Transverse magnetic field polarization will cause reducing of image contrast and resolution. The transmission function of the optical system $T(k\omega_X ; l\omega_Y)$ is a simple band pass function:

$$T(k\omega_X ; l\omega_Y) = \begin{cases} 1 \; for \; \sqrt{(k\omega_X)^2 + (l\omega_Y)^2} \le \omega_{MAX} = \dfrac{2\pi NA}{\lambda} \\ 0 \; else \end{cases} \tag{2.9}$$

Taking the square of expression (2.8) provides the intensity on the imaging camera:

$$\begin{array}{l} \left|A'_{0,0}\right|^2 + \ldots\ldots\ldots\ldots\ldots\ldots\ldots\ldots\ldots\ldots\ldots\ldots\ldots\ldots\ldots\ldots\ldots\ldots\ldots\ldots\ldots\ldots\ldots\ldots\ldots\ldots(\text{dc offset}) \\ \sum\limits_{k,l\neq 0} A'_{0,0} A^*_{k,l} T\left(k\omega_x - \omega_{off} ; l\omega_y\right) \exp\left[ik\omega_x x + il\omega_y y\right] e^{i\left(\gamma^{off}_{0,0} - \gamma^{off}_{k,l}\right)z} + c.c. + \ldots(\text{imaging}) \\ \sum\limits_{k.l\neq 0} \sum\limits_{',k',l'\neq 0} A_{k,l} T\left(k\omega_x - \omega_{off} ; l\omega_y\right) A^*_{n',l'} T\left(k'\omega_x - \omega_{off} ; l'\omega_y\right) \times \\ \qquad\qquad \exp\left[i(k-k')\omega_x x + i(l-l')\omega_y y\right] e^{i\left(\gamma^{off}_{k,l} - \gamma^{off}_{k,l}\right)z} \quad \ldots\ldots\ldots\ldots\ldots\ldots\ldots(\text{dark field}) \end{array} , \tag{2.10}$$

where the three terms on separate lines correspond to a constant term (top line), to the imaging terms (second line) and to the dark field cross-correlation image (bottom lines). Subtracting the dark field terms (by taking an image with the reference zero-order blocked so that only the third term survives) provides a sub-image that accurately captures the spatial frequency components transmitted through the optical system. Note that the imaging terms (middle line) are at the correct frequencies and that the offset illumination angle has cancelled out of the expression except for the filter transmission functions. Changing the illumination angle (and the angle of reintroduction) changes the

offset allowing recording of a different region of frequency space.

Now consider structural illumination where there are two coherent illumination beams, one at the same offset as in the previous example (extreme off-axis, corresponding frequency shift denoted as ω_{off} and corresponding longitudinal wavenumber denoted as γ^{off}). The other beam comes at the maximum offset allowed by the lens $\omega_{off} \lesssim NA/\lambda$ denoted as ω_{NA} in the equation (and the corresponding γ^{NA}).

Then the fields are:

$$\begin{aligned} &A_{0,0}\exp\left(-i\omega_{off}x\right)e^{i\gamma_{0,0}^{off}z}+\sum_{k.l\neq 0}A_{k,l}\exp\left[i\left(k\omega_x-\omega_{off}\right)x+il\omega_y y\right]e^{i\gamma_{k,l}^{off}z}+\\ &B_{0,0}\exp\left(-i\omega_{NA}x\right)e^{i\gamma_{0,0}^{NA}}+\sum_{p,r\neq 0}B_{p,r}\exp\left[i\left(p\omega_x-\omega_{NA}\right)x+ir\omega_y y\right]e^{i\gamma_{p,r}^{NA}z} \end{aligned} \tag{2.11}$$

and squaring while taking advantage of the fact that the $A_{0,0}$ beam is not transmitted to the objective image plane while the $B_{0,0}$ beam is transmitted through the lens gives:

$$\left|B_{0,0}\right|^2+ \tag{2.12(a)}$$

$$\left\{\begin{aligned}&\sum_{p,r\neq 0}B_{0,0}B_{p,r}^{*}T\left(p\omega_x-\omega_{NA};r\omega_y\right)\exp\left[i\left(p\omega_x x+r\omega_y y\right)\right]e^{i\left(\gamma_{0,0}^{NA}-\gamma_{p,r}^{NA}\right)z}+c.c.+\\&\sum_{p,r\neq 0}\sum_{p',r'\neq 0}B_{p,r}B_{p',r'}^{*}T\left(p\omega_x-\omega_{NA};r\omega_y\right)T\left(p'\omega_x-\omega_{NA};r'\omega_y\right)\exp\left[i\left(p-p'\right)x+i\left(r-r'\right)y\right]e^{i\left(\gamma_{p,r}^{NA}-\gamma_{p',r'}^{NA}\right)z}\end{aligned}\right\}+ \tag{2.12(b)}$$

$$\left\{\sum_{k,l}B_{0,0}A_{k,l}^{*}T\left(l\omega_x-\omega_{off};n\omega_y\right)\exp\left[-i\left(k\omega_x-\omega_{off}+\omega_{NA}\right)x-ik\omega_y y\right]e^{i\left(\gamma_{0,0}^{NA}-\gamma_{k,l}^{off}\right)z}+c.c.\right\}+ \tag{2.12(c)}$$

$$\sum_{k,l}\sum_{k',l''}A_{k,l}A_{k',l'}^{*}T\left(k\omega_x-\omega_{off};l\omega_y\right)T\left(k'\omega_x-\omega_{off};l'\omega_y\right)\exp\left[i\left(k-k'\right)\omega_x x+i\left(l-l'\right)\omega_y y\right]e^{i\left(\gamma_{k,l}^{off}-\gamma_{k',l'}^{off}\right)z}+c.c. \tag{2.12(d)}$$

$$\begin{aligned}&\sum_{k,l}\sum_{p,r\neq 0}A_{k,l}B_{p,r}^{*}T\left(k\omega_x-\omega_{off};l\omega_y\right)T\left(p\omega_x-\omega_{NA};r\omega_y\right)\times\\&\qquad\exp\left[i\left(k-p\right)\omega_x+i\left(\omega_{NA}-\omega_{off}\right)x+i\left(l-r\right)\omega_y\right]e^{i\left(\gamma_{k,l}^{off}-\gamma_{p,r}^{NA}\right)z}+c.c.\end{aligned} \tag{2.12(e)}$$

The first and the second (in the upper bracket) terms {2.12(a), 2.12(b)} are just the result

of the off-axis illumination at the edge of the pupil. This sub-image can be measured independently by blocking the extreme off axis beam, and subtracted from the composite sub-image. The third term 2.12(c) is the one we want, the image terms from the extreme off-axis illumination beating against a zero-order beam from the second illumination beam; because the zero-order beam is not at the correct angle to reset the frequencies to match the object frequencies (adjusted for magnification) there is a shift between the observed and the actual image plane frequencies that requires signal processing to reset (e.g. we are evaluating the Fourier components at an intermediate frequency). The fourth term 2.12(d) is the dark field from the extreme off-axis illumination. Finally the last term 2.12(e) is the combined dark field from the two illumination beams.

Two approaches to eliminating the unwanted dark-field terms are presented. The first one requires blocking just the second illumination zero-order beam without obstructions to the other diffracted information. This can be done by adding a moveable block at the edge of the objective pupil as shown in Fig. 2.10(b). A flow chart schematic of the procedure is shown in Fig. 2.11. The object is illuminated by two beams: one at an extreme off-axis angle (beyond the objective $\sin^{-1}(NA)$) and one (local oscillator) with an angle close to $\sin^{-1}(NA)$, such that its 0-order transmission is captured by the objective lens (Fig. 2.11(a)). By blocking only the 0-order we obtain the dark field image which can be subtracted from the image formed by interference of all orders from both beams {2.12(b), 2.12 (d), and 2.12 (e)}. Then we record the low frequency image obtained by the local oscillator object illumination with and without the 0-order blocked (Fig. 2.11(b)). We subtract the low frequency image without dark field from mixed image and restore high frequency image by shifting frequencies in Fourier space (Fig. 2.11(c)). The

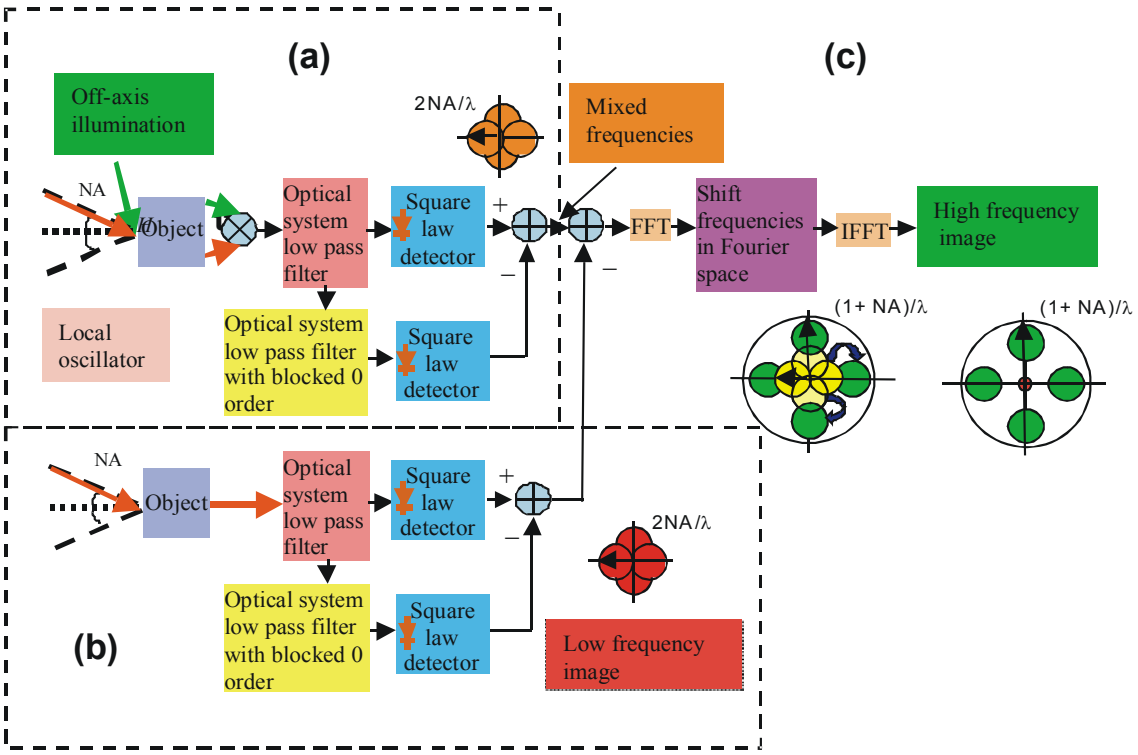

Fig. 2.11 Schematic of structural illumination and restoration algorithms: a) the object is illuminated simultaneously by two coherent beams: one at an extreme off-axis angle (green) and the other (local oscillator, orange) at an angle of ~$\sin^{-1}(NA)$ to the normal. High frequencies diffracted from the extreme off-axis illumination are mixed with low frequencies from the local oscillator and with dark field, the dark field of the image is sequentially obtained by blocking the 0–order beam in the image pupil plane and subtracted from image, b) the object is illuminated by local oscillator only; the low frequency image without dark field of local oscillator is obtained, c) the low frequency image is subtracted from high/low frequency mixture. Then frequencies are shifted in Fourier space to original positions and the total image can be reconstructed by standard IIM procedures: combining high and low frequency images.

reconstructed image can be obtained by combining high frequency images with the low frequency images recorded in necessary directions and with on-axis image as it was done in all previous IIM configurations. This procedure also includes the orthogonal

spatial direction for the Manhattan geometry test object; additional sub-images are necessary for objects with arbitrary structure. Appropriate filtering to deal with overlaps in frequency space coverage should be applied as has been discussed previously.

A second method to obtain the same result is to use a zero-order beam reinjected before the objective using a beam splitter (Fig. 2.12). The beam splitter is located between the object and the objective lens, eliminating all of the diffracted beams associated with the local oscillator, $B_{p,r} = 0, \forall p, r \neq 0$, and simplifying Eq. 2.12. We subtract the dark field image (recorded with blocked reference beam) and reference beam image (recorded with blocked illumination beam) using the same procedure described in Ref [Kuznetsova *et al.* 2007] and then restore high frequency image by shifting frequencies in Fourier space (Fig. 2.11) [Neumann *et al.* 2008a].

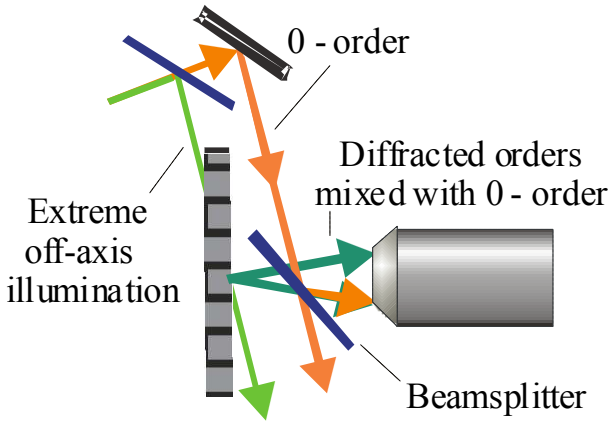

Fig. 2.12. Structured illumination with extreme off-axis illumination beam (green) and reference beam (orange) injected between object and objective lens.

Both methods have advantages and issues. The first arrangement requires access to the pupil plane of the system, which can be nontrivial. The second method does not contain

the first, second and fifth terms {2.12(a), 2.12(b), 2.12(e)}, so no access to the pupil plane is required, but it does require a beam splitter between the object and the optical system which reduces the system working distance. Also, there is a possibility of introducing aberrations, especially if the beam splitter is at an angle to the optic axis; aberrations can be minimized by using a thin pellicle beam splitter. Other approaches to address the issues are discussed in Chapter 3.

Interferometric methods require setting the phase relationship between the interferometer beams. This phase can be set in real time by observing the image of a reference object while adjusting the phase of one of the illumination beams. An alternative is to record images with an arbitrary phase shift and to evaluate the correct phase using signal processing approaches, again with the use of a reference object. Mean square error (MSE) methods can be applied for higher precision in setting this phase. Even without the use of a reference object, the recorded image has higher contrast at the correct phase point, very analogous to the higher contrast observed in an image at focus, but this is a somewhat subjective evaluation and is certainly pattern dependent. The use of a reference object is a more reliable indicator of the correct phase. In this configuration, it is particularly straightforward to use phase-shifting dark-field retrieval [Tamaguchi *et al.* 2001, Kreis *et al.* 2005] as an alternative to blocking the reference zero-order for eliminating the dark-field terms.

2.4.2 Experimental results with sstructural illumination

For our experiments we used an NA = 0.4 objective with a He-Ne laser illumination source (λ = 633 nm) so that the Rayleigh resolution was limited to ~ 950 nm. The results

of a structural illumination experiment with 240 nm critical dimension (*CD*, equivalent to half pitch (HP), e.g. linewidth for the equal line:space structures) along with the corresponding simulations are shown in Fig. 2.13. The mixed image obtained as the result of the two-beam illumination and corresponding to the all terms of Eq. 2.12 is shown in Fig. 2.13(a,b); Fig. 2.13(c,d) is the image after subtraction of the dark field and low frequency image, and Fig. 2.13(e,f) is the restored high frequency image.

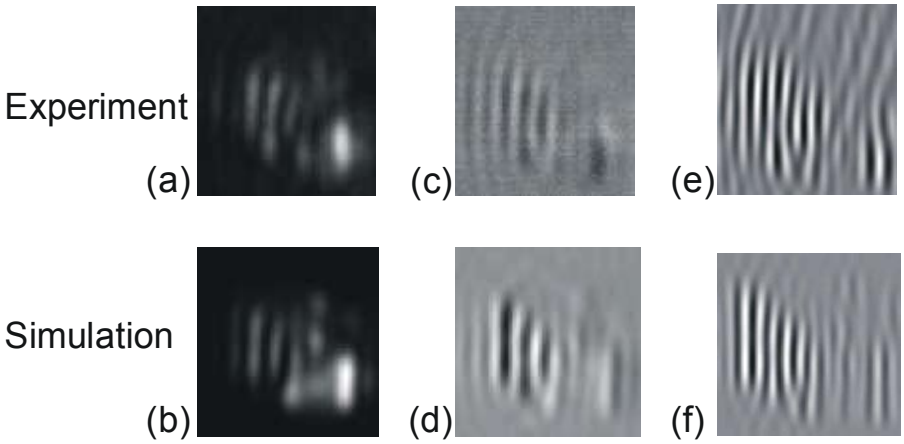

Fig. 2.13 (a,b) the mixed image corresponding to the interference of the low and high frequency images, (c,d) the image after subtraction the dark field and low frequency image, and (e,f) the restored high frequency image.

The reconstructed image of 260- and 240-nm CD structures, within the same image field, obtained by this method is shown in Fig. 2.14(a). Figure 2.14(b) is a crosscut of the image through 260 nm 240 nm structures compared with a crosscut of the corresponding simulation. A total of four offset images, two each in the *x*- and *y*-directions, with θ_{ill} = 53° and 80° were used along with a 0.4 *NA* objective. As discussed previously [Kuznetsova *et al.* 2007, 2008], this configuration provides resolution about 240 nm CD.

present Manhattan geometry structure has spectral content concentrated along the x- and y-directions, so the offset illuminations were restricted to those directions. It would be a simple matter to add additional frequency-space coverage for arbitrarily shaped structures by taking additional sub-images with rotation of the object around the (*x, y*) axes. The spatial frequency content of the image covers a wide range as a result of the large box (at 10x of the used CD) included in Manhattan structure.

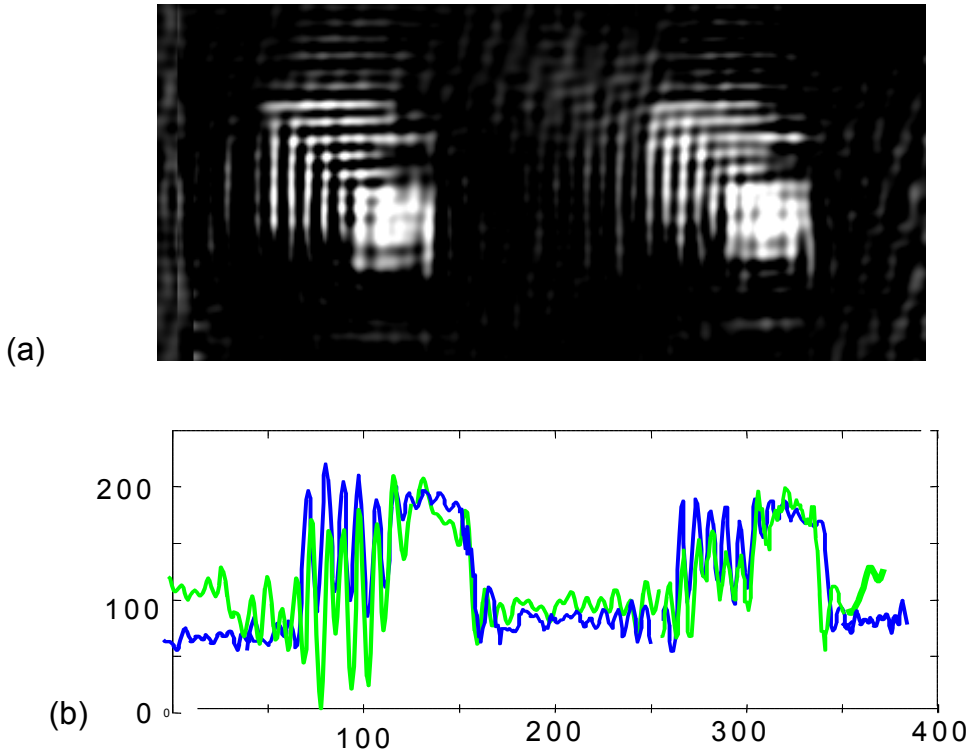

Fig. 2.14 a) Reconstructed image of 260- and 240-nm CD structures obtained using the optical configuration of Fig. 2.10(b); b) crosscut of the image (green) compared with a crosscut of corresponding simulation (blue).

The reconstructed image of the same structures obtained by the method with the beam splitter is shown in Fig. 2.15(a) and a crosscut of the image with corresponding simulation is shown in Fig. 2.15(b).

The quality of the experimental results for both methods is quite comparable. The first method retains a long working distance, but requires access to the imaging system pupil for blocking 0-order. The second does not require any modification to the traditional microscopy components, but has reduced working distance due to the beam splitter in front of the objective.

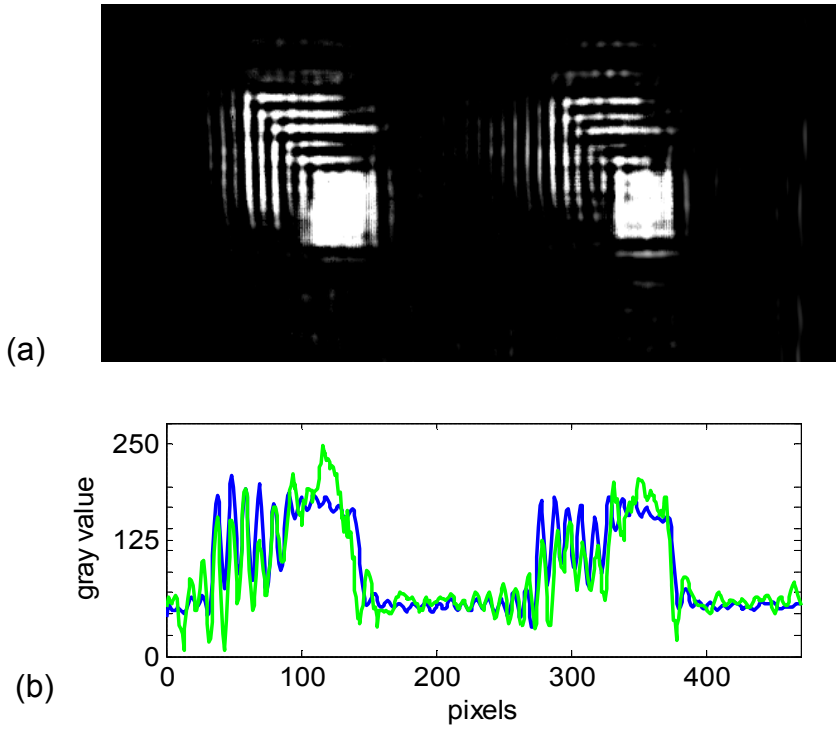

Fig. 2.15 a) reconstructed image of 260- and 240-nm CD structures (reinjection of zero-order between object and objective lens (Fig. 2.12), b) crosscut of the image (green) compared with a crosscut of corresponding simulation (blue).

There are some extra features in experimental results as compared to the modal due to the lack of precision in mutual phase determination between the sub-images and speckle effects from the coherent illumination. These features can be reduced by using improved arrangements and lower coherence sources. There are other possible alternatives; the

optimum choice will depend on the specifics of the object and the constraints of specific optical systems. Extension of the structural illumination IIM to the tilted object case is straightforward, so that the resolution extends to ~ $\lambda/4$ and to ~ $\lambda/4n$ with immersion. Specific application areas of interest include semiconductor manufacturing metrology and biosensors.

2.5 Half Solid Immersion IIM

The next contribution to resolution extension was obtained by evanescent illumination from a high-index substrate (total internal reflection illumination). The advantage of restricting the excitation volume within an evanescent field decay length has been explored intensively in surface studies providing ~ 10-fold enhancement of the axial resolution [Axelrod 2001]. A lateral resolution enhancement for fluorescence microscopy has been achieved with standing evanescent waves [Cragg and So 2000].

2.5.1 Optical configuration for half-solid immersion

The IIM optical arrangement [Neumann *et al*. 2008a] with an extreme off-axis (dark-field) illumination beam and a coherent reference beam, reinjected into the objective lens Fourier plane using an optical fiber, is illustrated in Fig. 2.16(a). Here, instead of off-axis illumination in air (Fig. 2.16(b)), we use illumination propagating beyond the total-internal reflection (TIR) angle in the transparent substrate in the same set up (Fig. 2.16(c)). The evanescent wave associated with the TIR extends beyond the substrate into the sample region where it is scattered by the subwavelength sample structure into propagating waves that provide information on the details of the object at spatial

frequencies up to $(n_{sub}+NA)/\lambda$ (Fig. 2.16(c)) and up to $(n_{sub}+1)/\lambda$ with a tilted optical axis (Fig. 2.16(d)). The object spatial information is contained in the amplitude and phase of the scattered fields at wavevectors corresponding to the difference between the illumination and collection wavevectors. An interferometric introduction of the zero-order diffracted beam (reflection or transmission as appropriate) in the back Fourier plane of the objective completes the optical scheme.

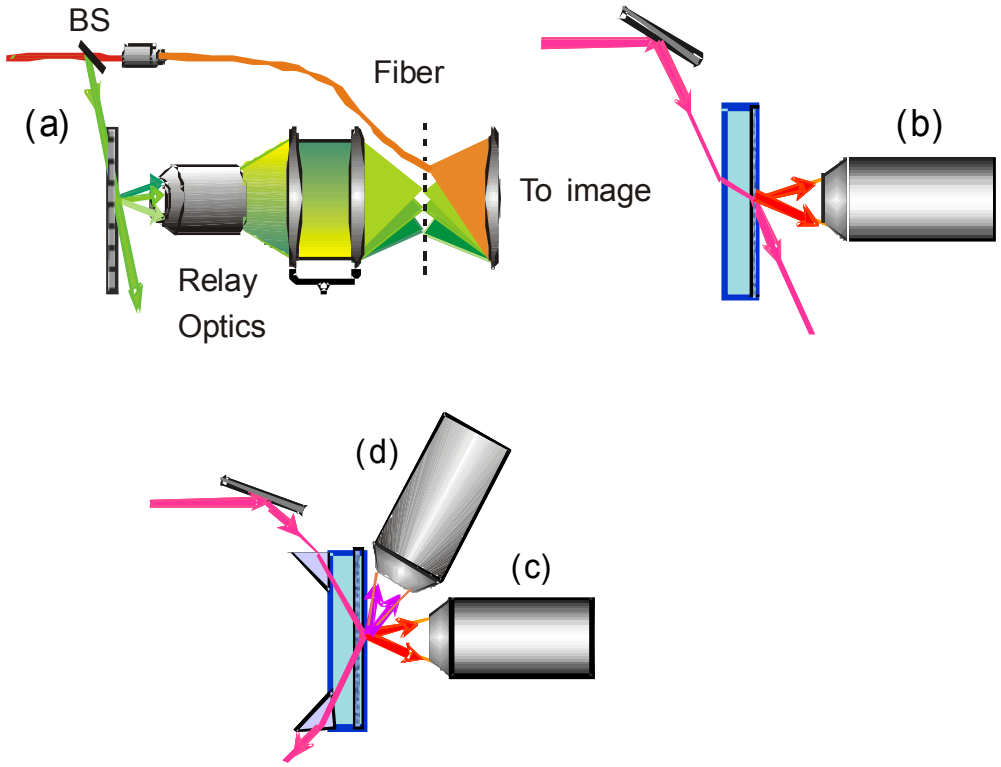

Fig. 2.16 Optical arrangements for IIM. a) IIM with a zero-order reference beam interferometrically reinjected in the back-pupil plane. b) Expanded view of illumination and detection configuration; c) Illumination through substrate to enhance the spatial frequency coverage; d) Rotated optical axis to col-

The Fourier intensity transform of the test pattern (Fig. 2.17(a)) for a linewidth (critical dimension or CD) of 180 nm is shown in Fig. 2.17(b) and for a CD of 150 nm in Fig.

2.17(c). The circles in Figs. 2.17(b,c) correspond to the bandpass limits of various microscopy configurations. The circle in the center of Fig. 2.17(b), with a radius of $NA/\lambda = 0.4/\lambda$, corresponds to the Abbé-limit spatial frequency range captured with on-axis coherent illumination ($NA_{ill} = 0$). The inner set of shifted circles in Fig. 2.17(b) (only single sidebands are shown for clarity; the complex conjugate regions are covered as well) corresponds to IIM with off-axis illumination beams at $\alpha_{ill} = 53°$ in the *x*-, *y*-directions that extend the frequency coverage to a radius $3NA/\lambda \sim 1.2/\lambda$. Additional frequency space coverage (second pair of circles) is available using evanescent wave illumination extending the frequency space coverage to a radius of $(n_{sub}sin(\alpha_{ill})+NA)/\lambda \sim 1.87/\lambda$ (with $\alpha_{ill} = 76°$) without tilt of the microscope optical axis.

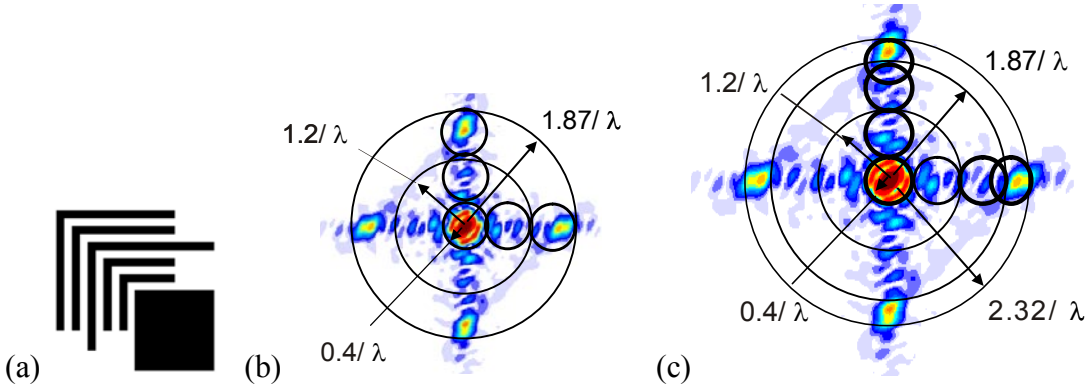

Fig. 2.17. Frequency-space visualization of IIM. a) Manhattan structure test pattern; scaled to different sizes as indicated; b) frequency space coverage for the structure with CD = 180 nm which is resolved for the configuration of Fig. 2.16(b); c) frequency space coverage for the structure with CD = 150 nm which requires the optical axis tilted configuration of Figure 2.16(d).

The third pair of off-axis sub-images in Fig. 2.17(c) corresponds to the tilted optical

axis. This frequency region is elliptical rather than circular, due to non-paraxial and conical diffraction effects associated with the off-axis optical system [Kuznetsova *et al.* 2007, 2008].

The tilted optical system, Fig. 2.16(d), is manifestly non-paraxial and the spatial frequencies measured in the laboratory frame have to be corrected before assembling a final composite image as it was described in details previously. The resolution limit now depends only on the refractive index of the substrate. For a glass substrate with n_{sub} = 1.51 and an NA = 0.4 objective, the $NA_{eff} \leq 1.91$ (geometry of Fig. 2.16(c)), allowing resolution of 166-nm half-pitch grating structures with λ = 633 nm. NA_{eff} is extended to ≤ 2.51 for the tilted optical-axis geometry of Fig. 2.16(d) with a corresponding minimum half-pitch extended to 126 nm. These resolution limits apply to simple grating structures (which have narrow Fourier spectra). For more complex structures such as the test pattern experimentally demonstrated, the pattern-dependent resolution is somewhat lower as a result of the need to capture additional information in the sidebands around the main diffraction peaks.

Extension to higher-index materials is straightforward and will provide extensive further resolution enhancement. For example, GaP has an index of 3.3 at 633 nm, and the spatial bandwidth therefore extends to $NA_{eff} \leq 4.3$ (half-pitch resolution to λ/8.6). In contrast to probe-based NSOM approaches, the IIM arrangement does not require close approach of a probe tip to the sample as the object scatters the evanescent illumination, coupled through the substrate, into propagating diffracted waves that are collected in a standard, full-field microscope configuration.

2.5.2 Experimental demonstration for half-solid immersion

The experimental result for an object containing both 180- and 170- nm CD structures in a single large-field image is shown in Fig. 2.18(a). The 180-nm CD object is within the bandwidth capabilities of this optical system while the 170-nm CD object has significant spatial frequencies that extend beyond the optical system bandwidth and so is not fully resolved. The five nested "ell" shapes are distinguishable for the 180-nm CD, but not for the 170- nm CD. The positions of the two objects are correctly restored by the image restoration procedure as is evident from the good positional overlap between the experimental and theoretical cross-cuts in Fig. 2.18 (b).

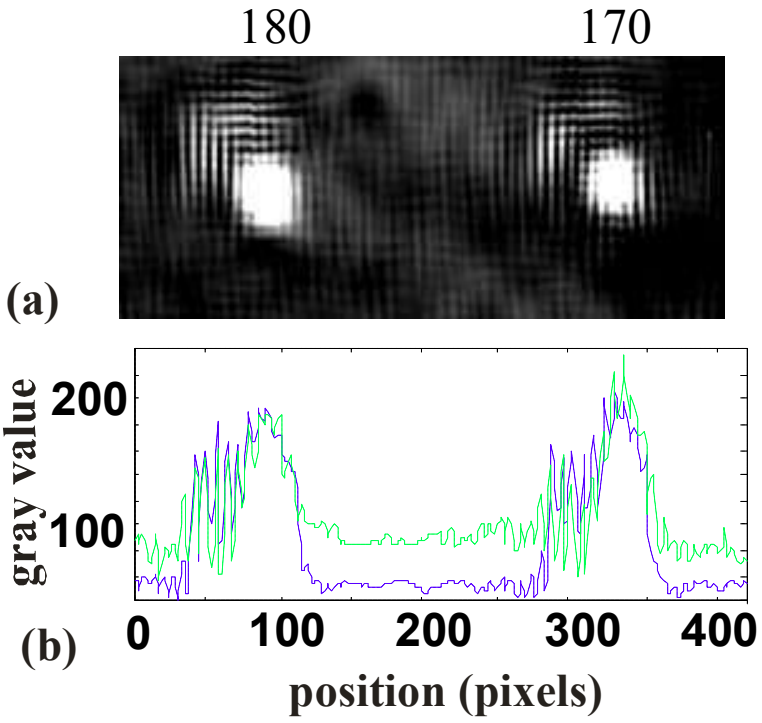

Fig. 2.18. IIM with evanescent illumination and normal (untilted) collection. a) Reconstructed image of 180- and 170-nm CD structures b) a crosscut (green) compared with a crosscut of corresponding simulation (blue).

By including tilt of the optical axis, additional spatial frequencies are accessible and the resolution becomes independent of *NA*. Ideally, we should be able to resolve 126-nm grating structures using a n_{sub} =1.51 glass substrate and a tilt angle of θ = $90° - \sin^{-1}(NA) = 66°$. Experimentally, we used an illumination angle (in the glass), α_{ill}, of 76° and a tilt angle of 35° and achieved $N_{eff} = n_{sub}\sin(a_{ill}) + \sin\left(\theta + \sin^{-1} NA\right) \sim 2.32$ (which allows 137 nm half-pitch grating resolution) and resolution of patterns with 150-nm CD features which is beyond the half-pitch linear systems limit in air of λ/4 ~ 158 nm, clearly demonstrating the evanescent coupling.

In order to decrease the influence of the camera pixel discretization on this high frequency image, the reference beam was adjusted to provide lower intermediate frequencies on the imaging camera which were reconstructed computationally [Neumann *et al.* 2008a]. The high frequency reconstructed image is shown in Fig. 2.19(a), model in Fig. 2.19(b) and crosscut comparison is in Fig. 2.19(c). The final result is shown in Fig. 2.19(d) along with the corresponding model, Fig. 2.19(e), and the crosscut comparison in Fig. 2.19(f). Very good agreement is achieved.

The overall quality of the image (even in the model) is not as well-defined as for the 180-nm image. Inspection of Fig. 2.17(b, c) shows the reason. Scaling of the frequency space coverage to get an equivalent image resolution requires both increasing the high frequency coverage along the principal axes, which we have accomplished, and addition-al coverage away from the principal axes, which we have yet to add. For the smaller pattern, the frequency content spreads away from the major axes and less of the important frequency information is captured in the present configuration. Additionally, Gibb's effects resulting from the hard cutoff in frequency response in a region with strong

spectral content, and the required precision in setting and measuring the tilt and illumination angles make it more difficult to obtain high-quality extended-field images as the frequency coverage is increased. The noise of the system causes problems for combination of the image from seven (or more) sub-images. We will address these problems in future work.

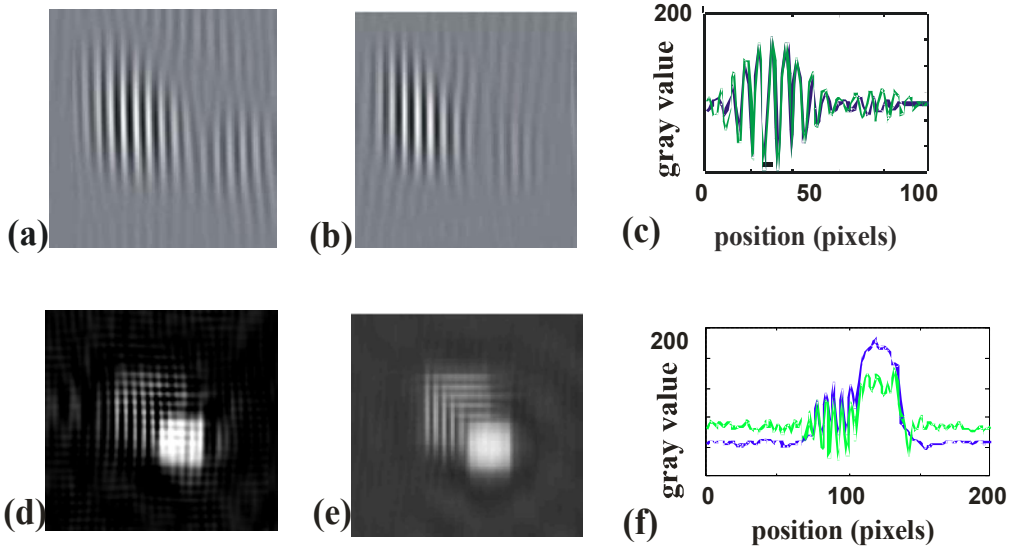

Fig. 2.19. IIM of a 150 nm structure using evanescent illumination and a tilted optical system.

a)High-frequency image obtained by evanescent wave illumination and tilted optical system; b) high-frequency image simulation and experiment; c) experimental and simulation cross-cuts of the high-frequency sub-images; d) experimental composite (full) image; e) simulation full image; f) experimental and simulation cross-cuts of the full images.

Evanescent illumination can be combined with structural illumination [Neumann *et al.* 2008a] eliminating the need for access to the back focal plane. This moves the interferometer to the front of the objective lens and makes IIM readily adaptable to existing microscopes. Structural illumination is roughly equivalent to recording the

spectral information at an intermediate frequency; additional computation is required to reset the frequencies. As noted, we have already taken advantage of this frequency shifting to reduce the camera pixel size and count requirements.

2.6 Full solid immersion

2.6.1 Optical configuration for full solid immersion

The full immersion extension is conceptually straightforward which is capable for further increase of the NA_{eff} up to $2n$ (up to 10 for Si and Si/Ge alloys) and the corresponding half-pitch resolution to 25nm ($\lambda/20$). We envision using a simple set of prisms or gratings to extract and conventional, air-based lenses to capture the information. As is always the case, there is a trade-off between the number of sub-images and the physical NA of the objective lens. This is the same spatial frequency space that is accessed by the solid immersion techniques discussed above. Each technique has comparative advantages that need to be further explored.

Using only a modest $NA = 0.4$ lens at $\lambda = 633$ nm and an object supported on a substrate with refractive index n, we have demonstrated a half-immersion imaging resolution with evanescent wave illumination to a maximum spatial frequency of $(n+NA)/\lambda$ with the objective normal to the substrate and up to $(n+1)/\lambda$ with a tilted objective [Neumann *et al.* 2008b]. We note in passing that tilting the objective lens, and correcting for the non-paraxial distortions introduced by that, is a cumbersome operation. We look for ways to make it easier to collect the spatial frequency information between $(n+NA)/\lambda$ and $(n+1)/\lambda$ as well as to extend the spatial frequency coverage towards $2n/\lambda$ by adding a grating coupler on the side of the substrate opposite the object. Phase and

intensity matching of the sub-images is achieved electronically using a reference object containing spatial frequencies within each recorded sub-image.

The illumination and collection configurations for half-immersion and full-immersion are shown in Fig. 2.20(a). The illumination laser beam is coupled into the substrate (using a prism, a grating or end fire coupling) and the object is illuminated by an evanescent wave. Image frequencies up to $(n+NA)/\lambda$ can be captured with an objective normal to the substrate surface (Fig. 2.20(a), objective A), and frequencies up to $(n+1)/\lambda$ with tilt of the objective off of the optic axis (Fig. 2.20(a), objective B). The evanescent waves from higher frequency content of the object are coupled back into the substrate by the boundary conditions at the substrate interface, and for spatial frequencies between $(n+1)/\lambda$ and $2n/\lambda$ propagate in the substrate at angles beyond the angle for total internal reflection. For a flat interface, the information at these spatial frequencies is not accessible, but the scattered light can be decoupled by a grating on the side of the substrate opposite to the object and redirected to an objective on the grating side, opposite the sample (Fig. 2.20(a), objective C). This optical system (the required coherent reference beam is not shown) leads to frequency aliasing as a result of the grating diffraction. While this can be corrected with the reference beam, it is usually preferable to offset the sub-image spatial frequencies to lower intermediate frequencies to reduce the pixel size and density requirement on the collection system focal plane and restore the actual frequencies computationally before combining sub-images. In addition, there are phase errors (aberrations) associated with the collection system which includes partial propagation both in the high-index substrate and in air. The treatment of these spatial frequency and phase corrections is discussed below.

The corresponding frequency space coverage is shown in Fig. 2.20(b). Normal incidence illumination and collection from the sample side is the traditional coherent illumination configuration represented by the small red circle with frequency space coverage to NA/λ. Illumination at an angle of $2NA/\lambda$ provides the offset orange circles with frequency space coverage to $3NA/\lambda$. For a Manhattan geometry object, two sub-images providing coverage in the x,y directions are typically used, additional sub-images, indicated by the lighter orange circles (at 45° to the principal x,y axes) can be added for additional off-grid frequency space coverage. The illumination and sample-side collection scheme of Fig. 2.20(a) allows increasing the spatial frequency coverage to $(n+NA)/\lambda$

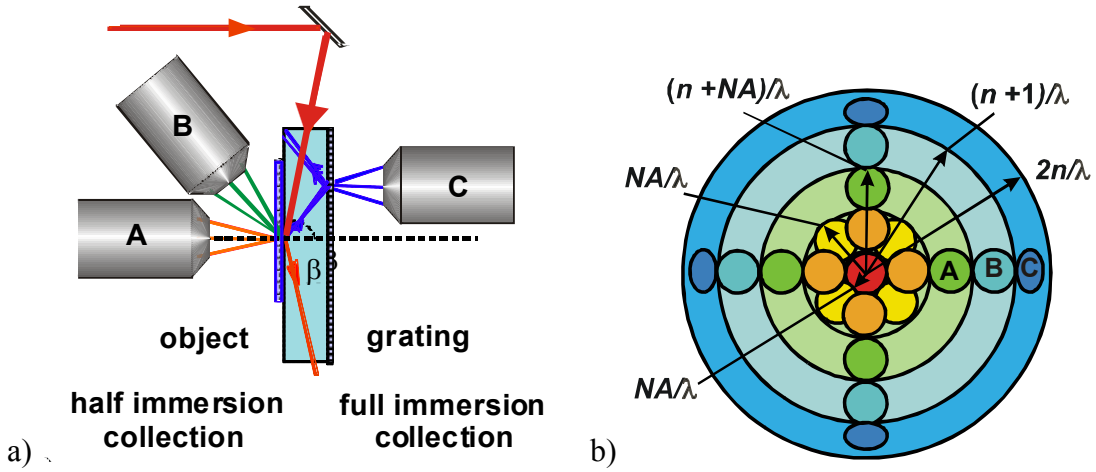

Fig. 2.20. a) Illumination and collection configurations: A - objective normal to the substrate surface, image frequencies up to $(n+NA)/\lambda$ can be captured; B - objective with tilt off from the optic axis, frequencies up to $(n+1)/\lambda$; C – objective on the side of the substrate with grating, frequencies between $(n+1)/\lambda$ and $2n/\lambda$; b) spatial frequency space coverage with regions collected with various geometries indicated.

(green circles). Collection with a tilted objective allows frequency space coverage up to $(n+1)/\lambda$. Finally, the substrate side collection discussed in this subchapter extends the

frequency space coverage to the linear systems limit of $2n/\lambda$ with a corresponding Abbe half-pitch of $\lambda/4n$.

As has been discussed in previously, the intensity, angle and phase of the reference beam have to be chosen to match all sub-images to the on-axis image [Neumann *et al.* 2008b]. For this purpose we used a reference object covering a small part of the field of view (FOV) in order to determine the correct intensity ratio, frequency shift and phase. These offset frequencies were then corrected in the image processing before the sub-images were combined.

One more preamble is necessary before tackling the image reconstruction. The description that follows has elements of ray tracing (looking at the propagation of scattered rays corresponding to specific spatial frequencies) and of Fourier optics (based on "infinite" plane wave propagation). The solution to this duality is to consider "wave packets" with center spatial frequencies that correspond to the direction of propagation and with a spatial extent that corresponds to the field-of-view, which is assumed to be much larger than the individual scattering objects within the field, but much smaller than the diameter of the lens. This of course corresponds to a broadening in the pupil plane and Fourier planes from the delta functions associated with plane waves to diffraction patterns corresponding to the finite field of view.

2.6.2 Full immersion frequency space coverage

The goal of this investigation is to explore the collection of additional scattered information at spatial frequencies beyond $(n+NA)/\lambda$ by collection from the back side of the substrate using one or more gratings to redirect this information into an objective lens. It

is clear from the geometry of Fig. 2.21 that the spatial frequency coverage of each sub-image depends on the thickness and refractive index of the substrate as well as on the field-of-view (*FOV*) and *NA* of the objective lens. For thicker substrates, the relevant information is spread across a wider area requiring a larger *FOV*. This may require multiple spatially displaced sub-images to extract all of the information (a synthetic *FOV*). If the available information extends beyond the $2NA/\lambda$ bandwidth of the collection optics, multiple gratings are required (a synthetic aperture). The minimum collected spatial frequency (angle α_1 in Fig. 2.21) sets the period *d* of the extraction grating:

$$d = \frac{\lambda}{n \sin \alpha_1 + NA} \tag{2.13}$$

If this frequency equals the maximum available from half immersion without a tilted

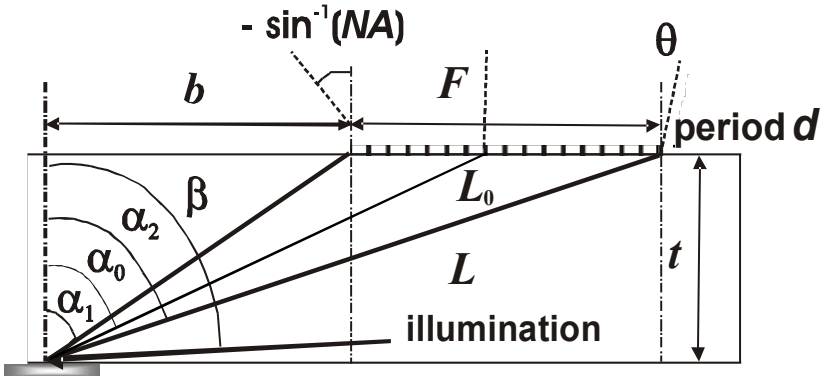

Fig. 2.21. Geometry shows access to collection high frequencies propagating in the substrate that correspond to small features.

objective, $(n+NA)/\lambda$, then:

$$d = \frac{\lambda}{2NA}. \tag{2.14}$$

This takes a scattered wave in the substrate corresponding to

$$k_{\alpha_1} = k_0 NA = nk_0 \sin\alpha_1 = nk_0 \sin\left[\sin^{-1}\left(NA/n\right)\right] \tag{2.15}$$

into a wave propagating in air at an angle $-\sin^{-1}(NA)$. Here, $k_0 \equiv 2\pi/\lambda$. Note that provided $NA > 0.33$, higher diffraction orders from the grating are outside the NA of the collection optics and do not interfere with the image; we consider an $NA = 0.4$ in the modeling. Over the range of spatial frequencies collected in each sub-image the diffraction efficiencies are roughly constant, thus allowing intensity compensation by sub-image matching procedures [Kuznetsova *et al.* 2007, Neumann *et al.* 2008a]. Our setup is free of the complications connected with multiple diffraction orders from gratings in comparison to the methods proposed by Lukosz [1967] and Sentenac et al. [2006]. In our case the gratings provide extraction of information out of the immersion media but not diffraction of near-field high-spatial frequency components directly from the object. There can be variations in diffraction efficiency as the various higher order beams, in both the substrate and in air, switch from evanescent to propagating waves. These are easily dealt with empirically by adjusting the amplitudes of the relevant portions of each sub-image independently, either by physically restricting the collection NA appropriately, or by separately addressing the regions of the sub-image electronically.

Progressively higher spatial frequency components impinge on the grating at larger horizontal displacements from the object and are diffracted at increasing angles, until the scattered beam at a displacement of $b + F$ from the object centerline is diffracted at an angle of $+\theta$ in air. The distance F corresponds to the FOV of the objective lens, which we take as focused on the grating surface, or to the width of the grating if it is smaller than the FOV. Provided $\theta \le \sin^{-1}\left(NA\right)$, the entire spread of scattered light incident on the grating is collected by the objective lens. From the geometry of Fig. 2.21, several

important relationships are readily derived:

$$\sin(\alpha_1) = \frac{NA}{n} = \frac{b}{\sqrt{b^2 + t^2}};\ b = t\left[\left(\frac{n}{NA}\right)^2 - 1\right]^{-1/2} \tag{2.16}$$

and

$$\begin{aligned}\sin(\alpha_2) &= \frac{b+F}{\sqrt{(b+F)^2 + t^2}} = \left[1 + \left(\frac{b+F}{t}\right)^{-2}\right]^{-1/2} \\ &= \left\{1 + \left[\frac{F}{t} + \left(\left(\frac{n}{NA}\right)^2 - 1\right)^{-1/2}\right]^{-2}\right\}^{-1/2}\end{aligned} \tag{2.17}$$

and the corresponding minimum half pitch is:

$$HP_{\min} = MAX\left\{\begin{array}{l}\dfrac{\lambda}{2(n+3NA)}; \\ \dfrac{\lambda}{2n\left\{1 + \left\{1 + \left[\dfrac{F}{t} + \left(\left(\dfrac{n}{NA}\right)^2 - 1\right)^{-1/2}\right]^{-2}\right\}^{-1/2}\right\}}\end{array}\right\} \tag{2.18}$$

The upper expression of Eq.2.18 is valid when the full *NA* of the objective lens is filled by the diffracted beams from the grating, e.g. the grating width *F*, and the optical FOV and NA are such that $\theta \geq \sin^{-1}(NA)$. If the angular spread is restricted by the field of view, or equivalently by the width of the grating, the lower expression pertains. An additional constraint is that $3NA < n$, since only spatial frequencies that can propagate in the substrate can be collected. The limiting behavior of HP_{min} is readily evaluated from this expression. For small *NA* where the full angular width of the lens is filled, the upper expression applies. For all interesting cases, $NA/n \ll 1$; that is the lens *NA* is much less than the refractive index of the immersion medium. For large fields of view or thin

substrates, $F/t >> NA/n$, $HP_{\min} \rightarrow \frac{\lambda}{n\left[4-(t/F)^2\right]}$. Thus, HP_{min} is always larger than the optics linear systems limit. The upper limit in Eq. 2.18 takes over before this result; thus the *NA* of the lens is filled in just a single sub-image. Additional gratings at smaller pitches of $\lambda/2(i+1)NA$ [i = 1,2,3,…] allow access to higher spatial frequency components of the image up to the linear systems limit of $\lambda/4n$. In the opposite limit, NA/n <<1 and $F/t << NA/n$, $HP_{\min} \rightarrow \frac{\lambda}{2\left(n+NA+\frac{nF}{t}\right)}$. The resolution is always somewhat improved over the starting point of half-immersion with the collection system optical axis normal to the object plane. In this case the linear systems limit of $\lambda/4n$ can be approached with a synthetic *FOV*, e.g. multiple sub-images with the collection optical system displaced to collect the higher spatial frequencies that are lost by the limited *FOV* with the same grating, and again, with multiple gratings (synthetic aperture), it is possible to extend the resolution close to the $\lambda/4n$ limit, as long as signal/noise ratio is sufficient to enable sub-image reconstruction into a full image.

Resolution (*HP*) restrictions as a function of substrate refractive index for *NA* = 0.4, 0.8, 1.2, fixed field of view (F = 32 μm) and substrate thickness (t = 50 μm) obtained from Eq. 2.18 are shown in Fig. 2.22. There is a point of transition for each curve (solid to dotted). The solid lines correspond to the upper expression of Eq. 2.18; the dotted lines to the lower part. In the dotted region additional sub-images are required to synthesize a larger FOV. Once the lens *NA* is filled, an additional grating is required to extract higher spatial frequency information and alias it into the lens *NA,* e.g. to synthesize a larger *NA*.

The combination of restrictions induced by substrate properties and synthetic ap

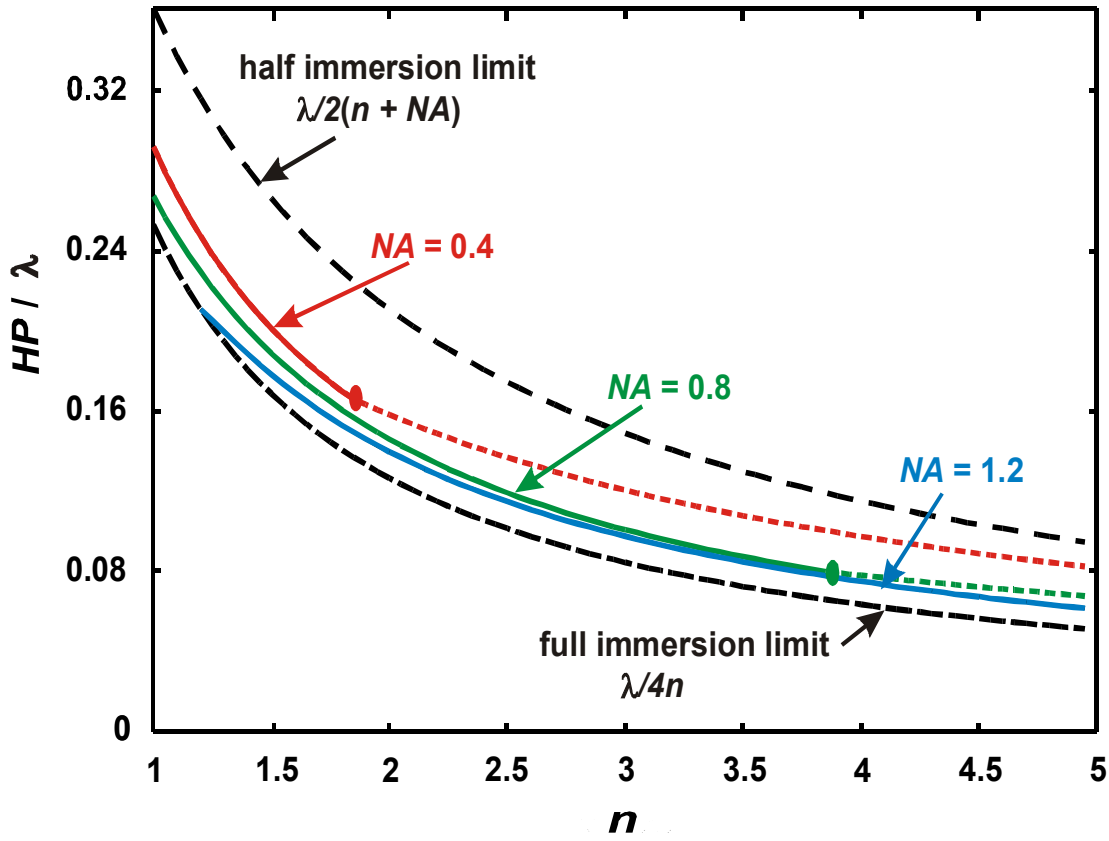

Fig. 2.22. Resolution restriction: normalized *HP* versus index of refraction for different *NA* (0.4, 0.8, 1.2), fixed substrate thickness t =50 μm and field of view 32 μm. Solid lines – dependence described by the lower part of Eq. 2.18, dashed lines- – dependence described by the upper part of Eq. 2.18.

erture (multiple of NA = 0.4) for a fixed field of view (F = 32 μm) with varying substrate thickness are shown in Fig. 2.23. The curves correspond to substrate thicknesses of 10, 30, 100 and 300 μm with break points denoted by the transitions from dashed to dotted lines by curves of synthetic *NA* restrictions. Here, $\lambda/[2(n+3NA)]$ corresponds to upper part of Eq. 2.18. The restrictions $\lambda/[2(n+5NA)]$ and $\lambda/[2(n+7NA)]$ appear by synthetic aperture extension with 1 and 2 additional aperture intervals along each spatial direction using adapted gratings for each interval as described above.

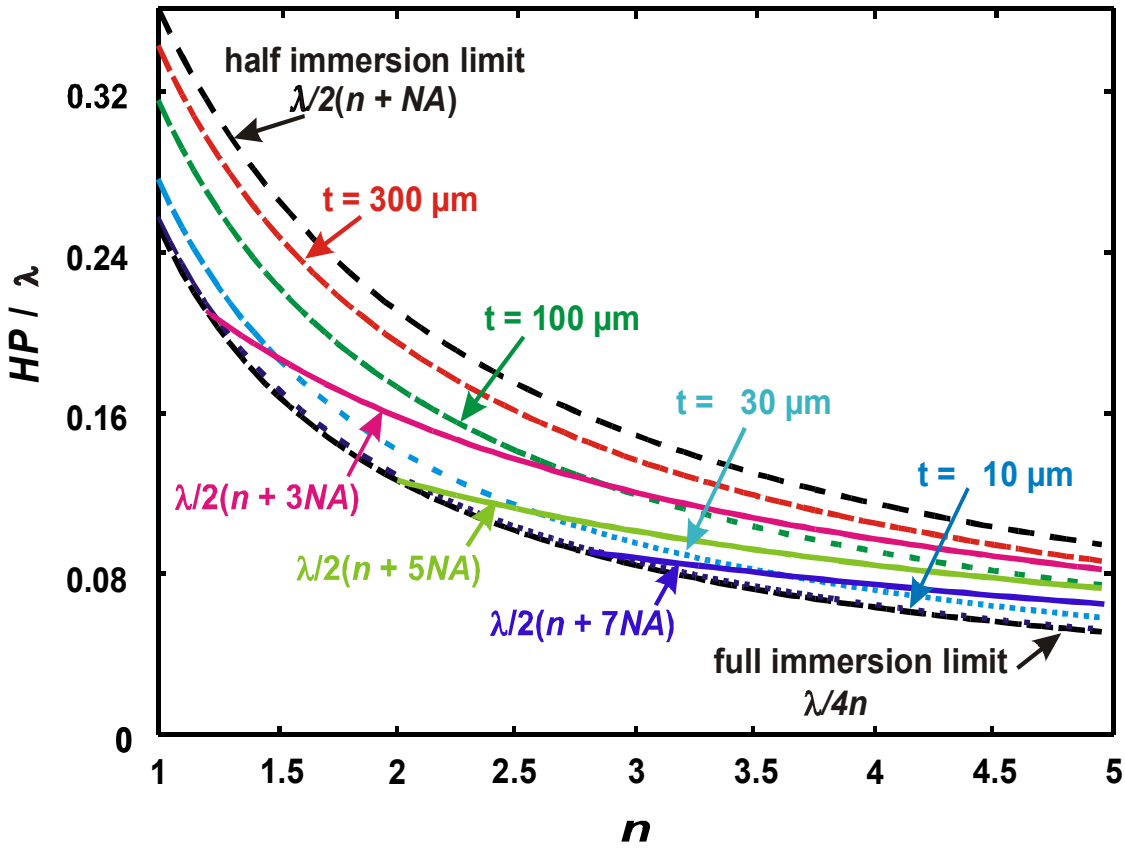

Fig. 2.23. Resolution restriction: normalized *HP* versus index of refraction for different substrate thickness (10, 30, 100, 300 µm) calculated with $NA = 0.4$, $F = 32$ µm in different synthetic aperture steps: long dashed lines are curves inside of synthetic aperture up to $\lambda/[2(n+3NA)]$, dashed lines are curves described by the upper part of Eq. 2.18.

We can infer from Figs. 2.22 and 2.23 that, for a single sub-image, a small *NA* optical system can give useful resolution extensions only for materials with low index of refraction. In order to reach high resolution using materials with high *n* we need either additional sub-images using multiple gratings or an objective with higher *NA*. A larger *FOV* objective enhances the resolution but typically is associated with lower *NA,* which again requires additional sub-images. A compromise between *FOV* and *NA* has to be found for the chosen substrate thickness and index of refraction to minimize the total

number of sub-images. These models do not include the impact of a finite signal-to-noise ratio (S/N). As the signal becomes more dispersed with thicker substrates, the S/N decreases and stochastic contributions to the image become more significant limiting the ability to accurately combine the sub-images and construct a composite image.

2.6.3 Full immersion image reconstruction

An initial experiment was conducted using a 1-mm thick glass substrate optically coupled to a second 1-mm thick microscope slide with a metal decoupling grating of period 560 nm. Thus the total thickness (object to grating) was 2 mm. The results showed the possibility of resolution of a periodic structure. The image consists of a repeated pattern of several parallel lines with a spacing of 240 nm within a trapezoidal envelope. The pattern is repeated at a spacing of 3.6 μm in both directions. A SEM image is shown in Fig. 2.24(a). The *x*-direction high frequency image was recorded and is shown in Fig. 2.24(b). The high frequency image contains much of the information about the original pattern: the repeated pattern is evident as is the clustering of lines in each repeat unit.

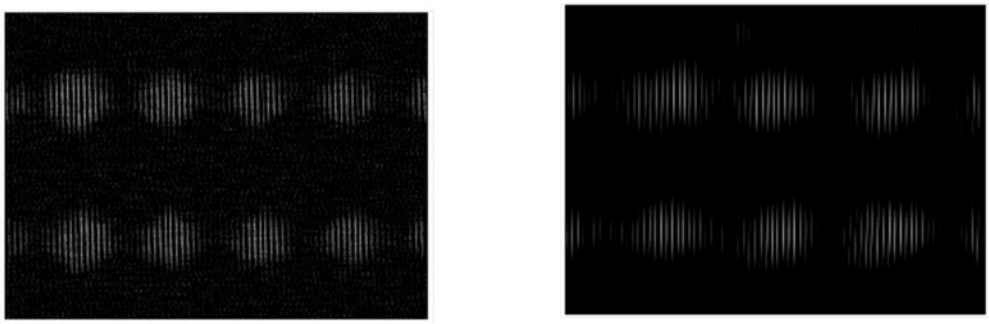

Fig. 2.24. a) SEM image of periodic structure, *HP*= 120 nm; b) IIM sub-image for t = 2 mm and decoupling grating half-pitch of 280 nm.

However, the image is distorted due to the geometry of propagation in the substrate [Fig. 2.21] and requires a restoration procedure before the proper image can be recovered. Clearly there are fewer clusters at the same transverse scale (3 vs. 4) in the distorted image, the relative spacing between the line clusters is changed and there are additional lines in the clusters, though the line pitch remains the same .

The distortion of the image is a result of the propagation in the substrate and depends on the optical path in the substrate, e.g. on the substrate refractive index and thickness. The optical configuration was shown in Fig. 2.20(a)(objective C), with the collection lens focused onto the grating surface. Since an aberration-free optical system has no phase error between conjugate planes, *e.g.* the grating surface and the camera focal plane, the only phase variations we need to consider are for propagation in the substrate (Fig. 2.21). For analytical simplicity, we consider a one dimensional case; the calculations are readily extended to two dimensional objects. Let L and L_0 be optical paths of an arbitrary and of the central ray in the substrate, α and α_0 are the angles of the corresponding rays to the substrate normal. θ is the angle of the arbitrary ray to the optical axis after diffraction from the grating and exiting the substrate (the ray must be captured by the objective in air and for convenience is shown as a marginal ray).

The angle α_0 of the ray in the substrate which is redirected along the optical axis in air is:

$$\sin\alpha_0 = \frac{\lambda}{nd} = \frac{2NA}{n}; \tag{2.19}$$

The marginal ray inclined at the angle α_2 to the normal in the substrate and an angle θ in air after scattering by the grating is described by:

$$\sin\alpha_2 = \frac{1}{n}\left(\frac{\lambda}{d} + \sin\theta\right) \tag{2.20}$$

Then the path lengths in the substrate are:

$$L_0 = \frac{t}{\cos\alpha_0} = \frac{t}{\sqrt{1-\sin^2\alpha_0}} = \frac{t}{\sqrt{1-\left(\frac{\lambda}{nd}\right)^2}} \tag{2.21}$$

$$L = \frac{t}{\cos\alpha_2} = \frac{t}{\sqrt{1-\sin^2\alpha_2}} = \frac{t}{\sqrt{1-\left[\frac{1}{n}\left(\frac{\lambda}{d}+\sin\theta\right)\right]}} \tag{2.22}$$

and the phase difference between the arbitrary ray and the central ray is

$$\Delta\varphi = \varphi - \varphi_0 = \frac{2\pi nt}{\lambda}\left[\frac{1}{\sqrt{1-\left[\frac{1}{n}\left(\frac{\lambda}{d}+\sin\theta\right)\right]^2}} - \frac{1}{\sqrt{1-\left(\frac{\lambda}{nd}\right)^2}}\right]. \tag{2.23}$$

The rays in Fig. 2.21 are k-vectors of the plane waves propagating at angles θ corresponding to the image spatial frequencies f_x. So, the phases at each spatial frequency can be corrected in Fourier space using the distortion phase function provided by the 2D generalization of Eq. 2.23. Clearly that distortion phase function (Eq. 2.23) provides only a relative phase correction. The constant term (the phase shift introduced by the central ray optical path) will be automatically corrected later by the sub-image phase-matching procedure required in IIM, since this constant term is indistinguishable from arbitrary constant term introduced by the phase of the reference arm of the Mach-Zehnder interferometer inherent in IIM.

Simulation of the impact of this phase distortion on the image with nested-L structure and a delimited grating with CD =120 nm (Fig. 2.25) is shown in Fig. 2.26. The high spatial frequency (between NA/λ and $3NA/\lambda$) filtered image of the model is shown in Fig.

2.25(b). The image is expanded, *e.g.* additional features appear on both sides of object due to lack of compensation in these regions as a result of the optical bandwidth limit. This is just the familiar Gibbs effect associated with an abrupt cut-off in frequency space.

a) b)

Fig. 2.25. a) model CD = 120 nm structures, b) *x*-direction high frequency image.

The high frequency image after the application of the phase aberrations for a substrate thickness of 1 μm [5 μm] is shown in Fig. 2.26(a) [Fig. 2.26(b)] (crosscut Fig. 2.26(c) [Fig. 2.26(d)]). There is additional walk-off of the intensity vs. position as a result of the spreading of the image intensity. The reason for this spread is the progressive walk-off of higher spatial frequency components (phase distortions) as they propagate across the substrate. Here, the additional features appear non-symmetrically to the illumination side. Also, unlike the Gibbs effect, no information is lost in general. The step from Fig. 2.25(b) to Fig. 2.26(a,b) is completely deterministic and is easily inverted by taking the Fourier transform of the laboratory frame image, applying the inverse of Eq. 2.23 and retrans-forming back to the image frame, providing all information is captured and there are no S/N limitations. The spatial extent of the image spectrum expands with increasing substrate thickness (compare Fig. 2.26(a) and 2.25(b)). The intensity spread extension beyond the objective field of view leads to the loss of information which results in

reduction of the image quality after restoration. This information can be accessed with a synthetic FOV, e.g. shifting the objective lens to acquire additional sub-images with an extended grating at the same pitch.

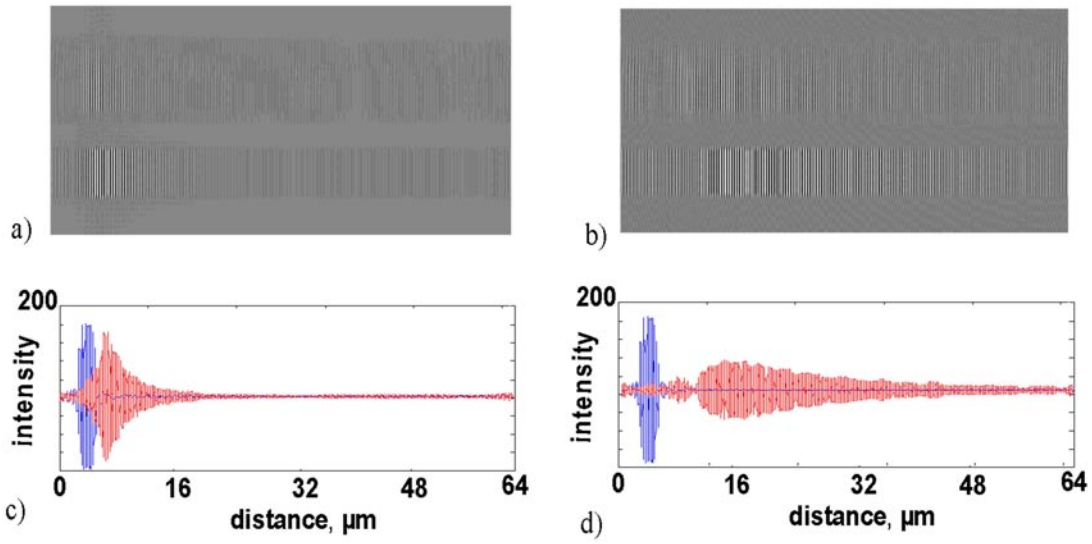

Fig. 2.26. Difference in expansion of spectral package (120 nm features) for different substrate thicknesses (n =1.5, F= 64 μm): a) t = 1 μm, image expansion ~ 3 times; b) t = 5 μm, image expansion ~ 10 times; comparison of filtered image crosscuts (blue) with crosscuts of images (red) distorted by substrate propagation with: c) t = 1 μm; d) t = 5 μm.

Without shifting the objective lens, the loss of information is equivalent to the reduction of captured range of frequencies ($NA_{sub} < NA$) for a single sub-image, which is a function of the *FOV*. To evaluate this degradation of the image bandwidth in a single image, consider again Fig. 2.21, but now in a configuration where the grating is chosen so that a particular HP_c is along the optical axis, e.g. fix the optical axis (center) frequency rather than the low-frequency marginal ray. The dependence of the angular bandwidth, $2NA_{sub}$, versus the *FOV* is easy to obtain from Fig. 2.21. The *FOV (F)*

normalized to the slab thickness is:

$$\frac{F}{t} = \tan\alpha_2 - \tan\alpha_1 \tag{2.24}$$

On the other hand, the marginal angles for a particular NA_{sub} can be written as function of an angle $\sin\alpha_c$ of the center frequency, corresponding to the chosen HP_c.

$$\sin\alpha_2 = \sin\alpha_c + NA_{sub} \tag{2.25}$$

and

$$\sin\alpha_1 = \sin\alpha_c - NA_{sub}, \tag{2.26}$$

where, for an illumination angle $\sin\beta$:

$$\sin\alpha_c + \sin\beta = \frac{\lambda}{2nHP_c} \tag{2.27}$$

Combining Eqs. 2.24-2.26 gives an implicit relation for the optical system parameters

$$\frac{F}{t} = \frac{\sin\alpha_c + \frac{NA_{sub}}{n}}{\sqrt{1-\left(\sin\alpha_c + \frac{NA_{sub}}{n}\right)^2}} - \frac{\sin\alpha_c - \frac{NA_{sub}}{n}}{\sqrt{1-\left(\sin\alpha_c - \frac{NA_{sub}}{n}\right)^2}} \tag{2.28}$$

This dependence shown in Fig. 2.27 for several HP_c normalized by n and λ $\left(g = \frac{nHP_c}{\lambda}\right)$ allows us to define NA_{sub} of each sub-image and to estimate the number of sub-images which are necessary to cover most of the available spatial frequency space (along a specific direction).

We can see from Fig. 2.27 that, in order to prevent the loss of information, we need an objective with a bigger *FOV* or additional spatially shifted sub-images to build a synthetic *FOV*. These conclusions are qualitatively the same as those drawn from Figs. 2.22 and 2.23.

Examples of images shown in Fig. 2.26 restored using a FOV of 16 μm are shown with corresponding crosscuts (red) in comparison with the undistorted image (green) and differences between the restored and filtered crosscuts in Fig. 2.28. Fig. 2.28(a) is obtained from Fig. 2.26(a), and Fig. 2.28(b) from Fig. 2.26(b). It is clear that the sub-image in Fig. 2.26(a) for a 1 μm thick substrate is extended less than the sub-image in

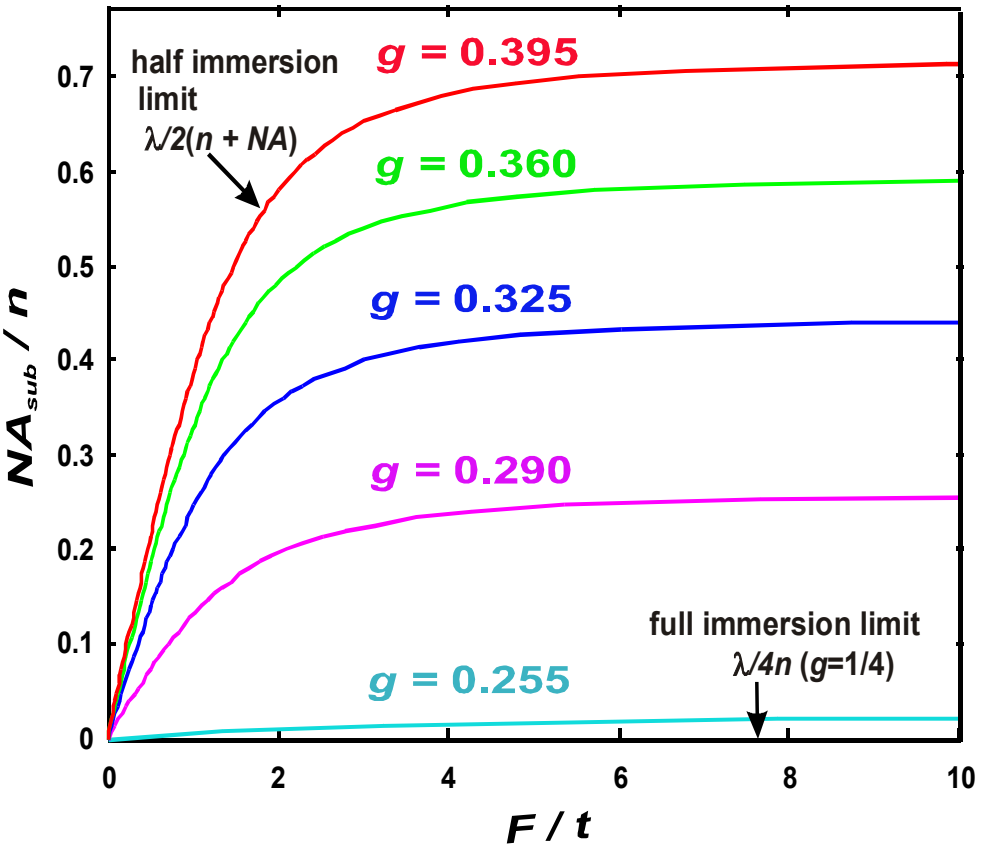

Fig. 2.27. Synthetic aperture guideline: normalized sub-image bandwith $2NA_{sub}$ versus normalized FOV for different extracting gratings represented by center frequency HP_c $\left(g = \frac{nHP_c}{\lambda}\right)$

Fig. 2.26(b) for a 5 μm thick substrate and the quality of restored image in Fig. 2.28(a) is

higher than in Fig. 2.28(b). Quality of images was estimated by MSE method comparing original high resolution image with restored images [Frieden 1983]. Extension of

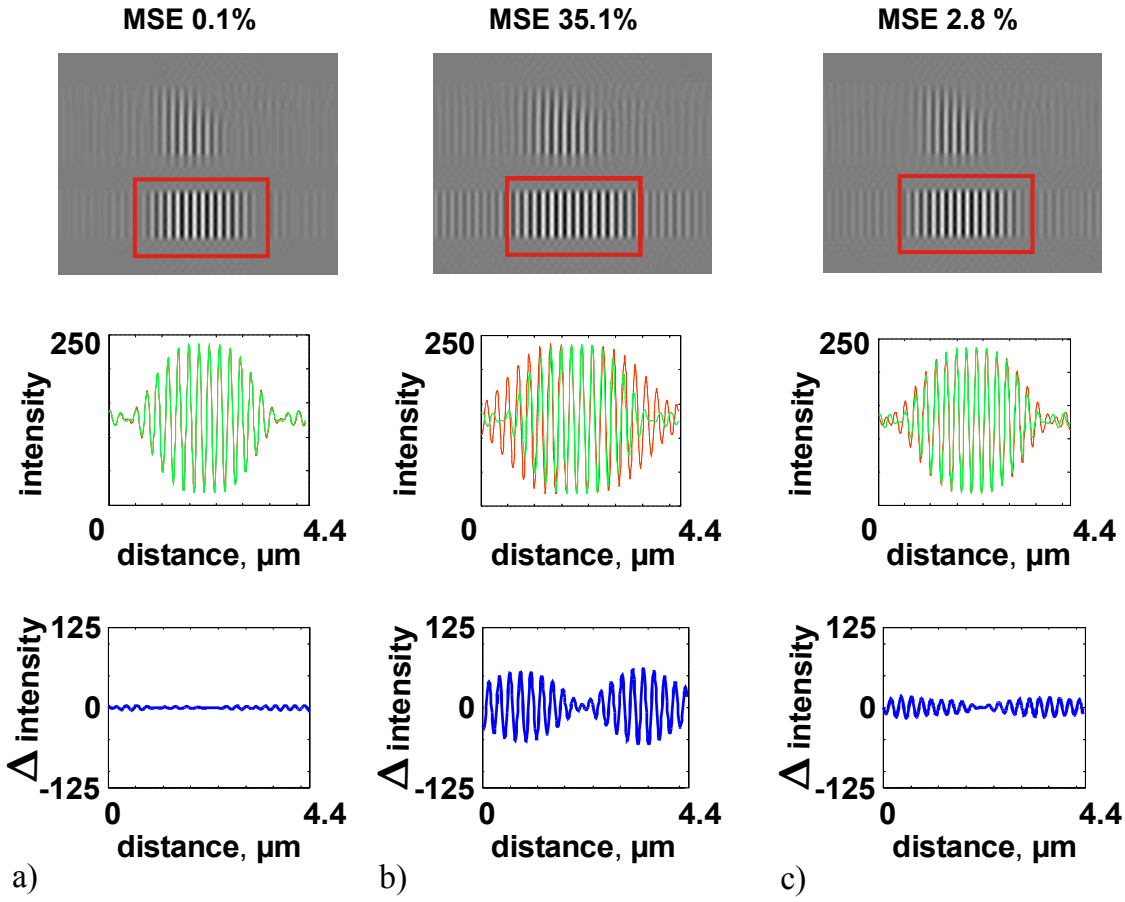

Fig. 2.28. Restored images (CD=120 nm, n = 1.5), crosscuts and crosscut differences: a) t = 1μm, F= 16 μm – quality of the resorted image is good, b) t = 5 μm, F= 16 μm, quality of the resorted image is poor due to increased substrate thickness; c) t = 5 μm, F=32 μm, quality of the resorted image is improved as the result of increasing field of view.

recorded field of view to 32 μm for the image in Fig. 2.26(b) improves the quality of restored image (Fig. 2.28(c)), showing the complex interrelationships between the resolution, *FOV*, *NA,* substrate thickness and the refractive index.

For an additional perspective on the ability to restore these images, the restored images with different *HP* were compared with the filtered high frequency images using a *mean square error* (MSE) metric. A simple ten-line grating pattern was chosen for MSE analyses (inside of the red square) and normalized to a gray field (Fig. 2.29). The curves of MSE versus *HP* for a λ = 633 nm, n = 1.5 substrate thicknesses of 0.5, 1, 3, 5, 10 μm and a restoration *FOV* of 32 μm are shown. For a comparable MSE procedure, it is important to have the spectral content of the image filtered similarly. Thus, we ensure

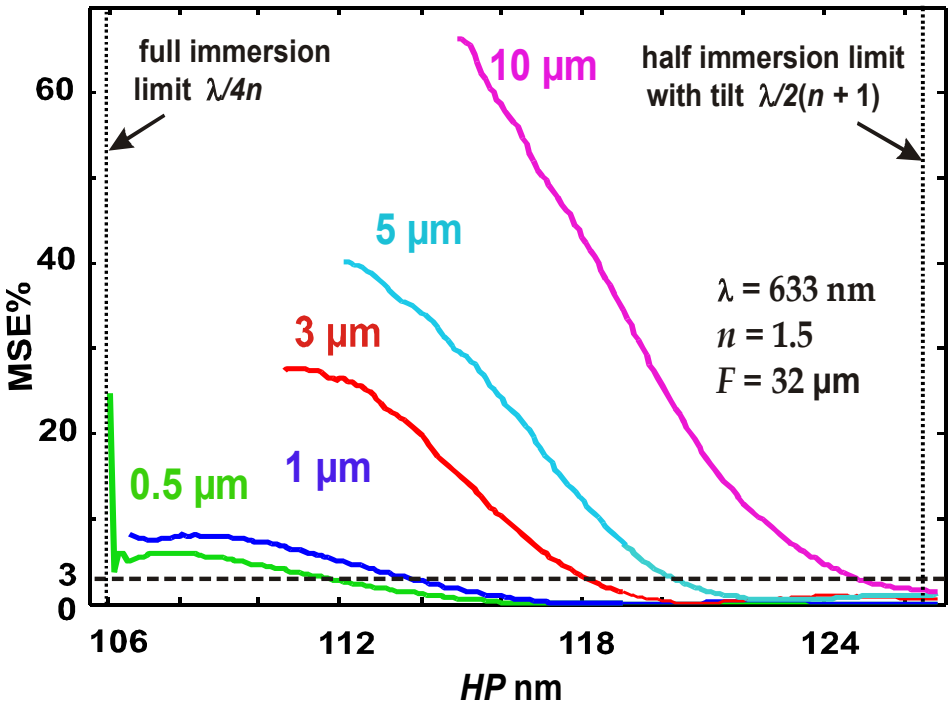

Fig. 2.29. MSE versus HP of a 10-line pattern for different substrate thicknesses, n = 1.5, F = 32 μm, λ = 633 nm. 3% MSE considered as images with acceptable quality. 0.5 μm substrate allows restoration of images with 112 nm features, 1 μm ~ 113.5 nm, 3 μm ~ 118 nm, 5 μm ~ 120 nm, 10 μm ~ 124 nm.

that the center frequency at the *HP* always passes through the center of the collection objective, as in the derivation of Eq. 2.28.

These calculations were carried out from the theoretical limit $\lambda/4n = 0.106$ µm to the half immersion limit $\lambda/(n+1) = 0.126$ µm ($\lambda = 633$ nm, $n = 1.5$). The MSE drops as image becomes resolvable. As expected, the distortion (expansion of the frequency content across the detection plane) of image features is lower in thinner films, which allow higher resolution with a smaller *FOV*.

The same models were used for substrates with different refractive indices in order to evaluate possible resolvable *HP* with MSE = 3% for substrate thicknesses of 1-, 5-, and 10-µm. The results are summarized in Fig. 2.30, where the resolvable *HP* versus

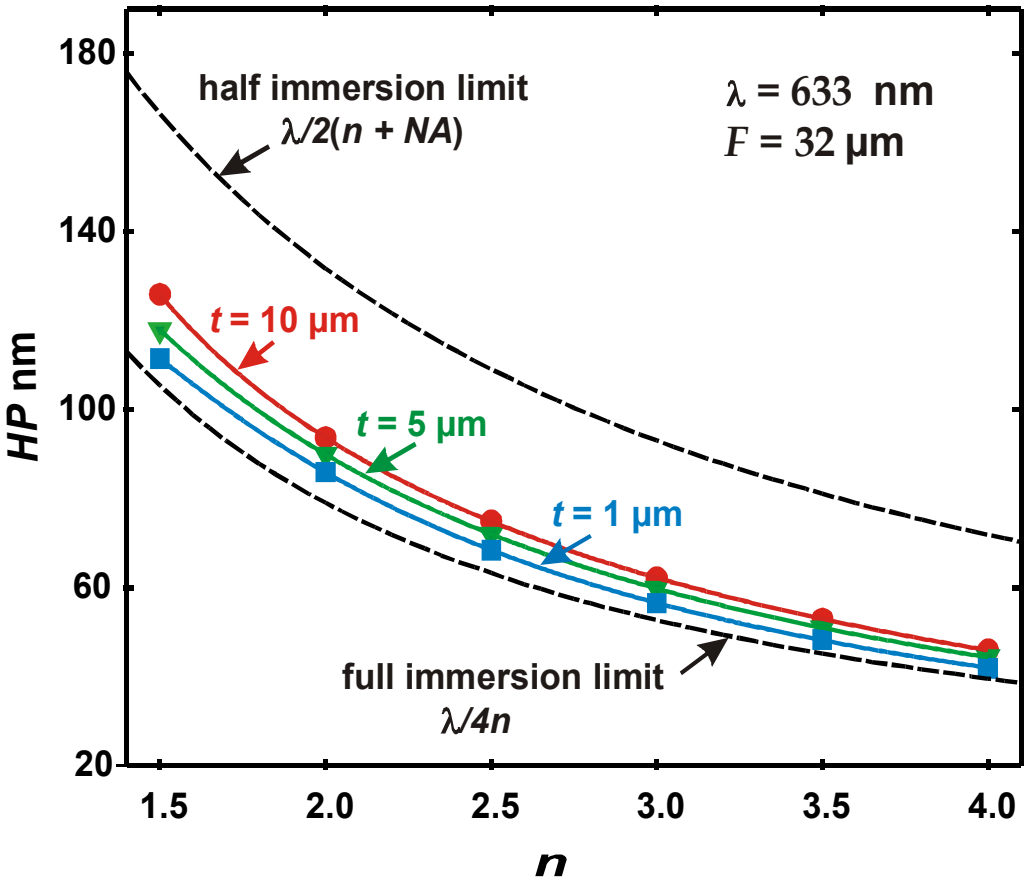

Fig. 2.30. *HP* versus *n* for different substrate thicknesses: 1, 5, 10 µm ($F = 32$ µm), $\lambda = 633$ nm. Substrates with higher *n* allow restoration and resolution of images with smaller features.

refractive index is shown. The lower black dashed curve $\lambda/4n$ is theoretical limit of full immersion resolution, the black upper dashed line $\lambda/2(n + NA)$ is the half-immersion limit with an un-tilted objective.

The modeling of image reconstruction represented in Fig. 2.30 qualitatively confirms the results obtained by investigation of theoretical resolution limit (Fig. 2.23). The image resolution depends on the optical system and substrate properties (*NA*, *FOV*, *t* and *n*). The achievable resolution scales inversely with the substrate index of refraction. Substrate thicknesses greater than several times the *FOV* result in experimental difficulties, both in registration and in lowered signal intensity leading to S/N issues.

Chapter 3. Conclusions and future work

3.1 Achievable resolutions in advanced configurations

3.1.1 Materials and frequency tiling for solid immersion

The goal of IIM is to reach ultimate resolution limits of non-fluorescent microscopy by using IIM in new optical configurations realizing a solid immersion technique with immersion materials employed in advanced regimes unsuitable in other systems. Multiple partial images obtained with off-axis illumination and interferometric optics can be combined to assemble a composite image corresponding to larger frequency space coverage than is available with conventional imaging approaches. Relatively low *NA* microscope objective in this synthetic aperture approach allows retaining large field-of view and working distance.

Using Manhattan geometry structures with different *CD* as objects and He-Ne laser with 632.8 nm wavelength as a coherent illumination source, we have shown the possibility of effective *NA* extension almost up to 1+*NA* (to 1.38 for *NA*=0.4 in our experiment). Tilting the object plane has further extended the resolution to λ/4 (or to λ/3.76 in our experiment). Evanescent wave illumination has been demonstrated to extend the resolution of IIM to λ/2(*n*+1). Images of 150-nm structures (arbitrary Manhattan geometry pattern) using a 633 nm wavelength (λ/4.2) have shown optical resolution below λ/4, the linear systems limit of available resolution in air. Further resolution improvement with this half-immersion geometry is available for a substrate with a higher refractive index (e.g. GaP with n = 3.3 allows NA_{eff} of 4.3 and a corresponding periodic pattern half-pitch resolution of 74 nm = λ/8.6 at 633 nm).

Table 3.1 provides resolutions calculated for several microscopy techniques and

compares their practical resolution achievements for different λ with a silicon immersion substrate.

Table 3.1. Wavelength dependent resolution with Si solid immersion layer for different techniques.

Wavelength (nm)	**1064**	**704**	**633**	**488**	**405**
	amorphous Si properties [SOPRA 2013]				
Si refractive index	4.1	4.31	4.5	5.01	4.97
Si 1/e length (μm)	--	1.6	0.2	40nm	13nm
Alternative approaches					
Annular illumination (NA=1.3) λ/4 *NA* [Vainrub *et al.* 2006]	205	135	122	94	79
SIL λ/4*n* [Köklü *et al.* 2009**] (thick lens does not allow materials with loss)**	65	--	--	--	--
IIM					
λ/4 (no immersion)	266	176	158	122	102
λ/[2(*n*+1)] (half immersion)	115	67	58	41	34
λ/4*n* (full immersion)	65	41	35	25	21

Annular illumination using the ~2× resolution advantage of incoherent off-axis illumination can be combined with immersion techniques (current results are obtained with liquid immersion and an *NA*=1.3 [Vainrub *et al.* 2006]). However, this requires alignment between two specialized high *NA,* small FOV objectives, which is a challenging task.

Even ignoring the fact that usually there is a tradeoff between the *FOV* and the *NA*, such objectives cannot use materials with significant losses due to the required macroscopic optical thicknesses.

Solid immersion lenses (SIL) [Köklü *et al.* 2009] provide a relatively cost-effective solution for increasing *NA* by a combination of a standard objective with a section of a high index refraction sphere as solid immersion media. This method has shown good resolution (to 145 nm using a Si SIL at 1.2 μm of FOV) but again can only be used with relatively long wavelengths since the sphere section (which in practice is close to a hemisphere) requires essentially lossless materials. As opposed to SIL, IIM can provide up to few tens of nanometers resolution with immersion media such as silicon at visible (red to green) wavelengths while retaining the full field of view, large working distance, depth of field, and low-cost of low *NA* objectives.

The possible increase of NA_{eff} is illustrated by Fig. 3.1, drawn for a 0.4 *NA* system and silicon as immersion medium. The red inner circle corresponds to the NA/λ frequency space coverage associated with coherent, normal-incidence illumination. The successively larger diameter concentric circles correspond to the frequency space coverage of the IIM optical configurations discussed in this theses: $3NA/\lambda$ (orange) is the coverage for a single offset exposure (Figs. 2.2 - 2.4); $(1+NA)/\lambda$ (yellow) is the coverage including multiple off-axis illumination angles (Fig. 2.5); tilting of the objective (Figs. 2.6 - 2.9) extends the frequency space coverage to $2/\lambda$ (lime green), independent of the NA of the objective; the dotted green circle at $(1+n)/\lambda$ show the coverage with half-immersion for an index of 1.5 (glass); light blue circle shows the full immersion frequency space coverage for the glass; the next blue circle at $(1+n)/\lambda$ shows the coverage

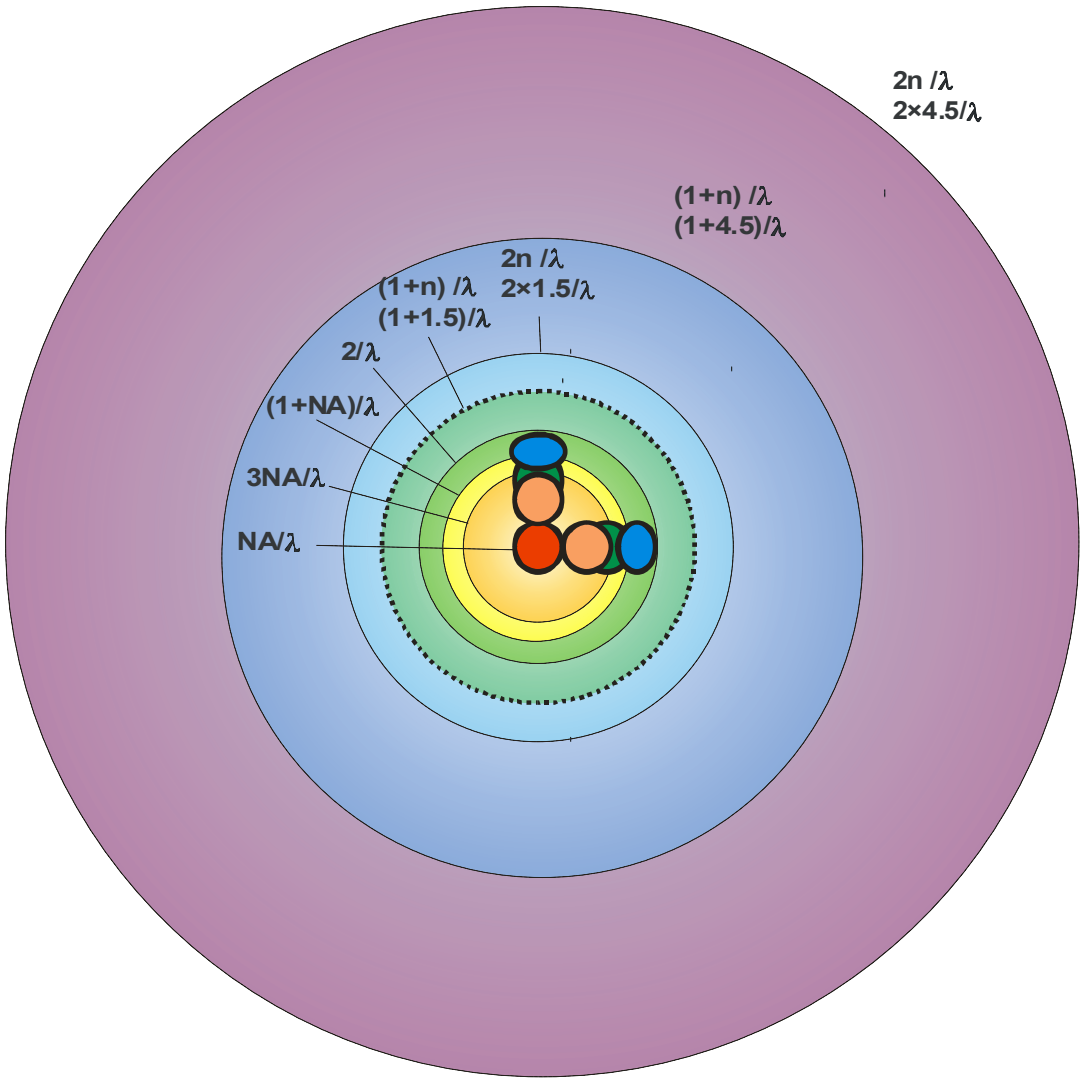

Fig. 3.1. Available frequency space coverage for various optical systems.

with half-immersion for an index of 4.5 (Si) at 633 nm (Figs. 2.16 - 2. 19); and finally the purple circle shows the full immersion frequency space coverage for the same index (Fig. 2.20).

As is always the case, there is a trade-off between the number of sub-images and the *NA* of the objective lens. As the frequency coverage is extended, the use of higher *NA* lenses will reduce the number of sub-images required for an equivalent coverage of

frequency space. Fig. 3.2 provides an example of two similar 1D tiling schemes for a Si substrate (n_{sub} = 4.1 at 1064 nm), one (vertical) for a 0.65 *NA* and the other (horizontal) for a 1.4 *NA* conventional immersion objective. NA_{ill} corresponds to particular illumination angle θ. Frequency G is normalized frequency of the decoupling grating. As many as seven sub-images are necessary to provide complete 1D coverage along just one axis for the 0.65 *NA*, whereas only three are sufficient for the larger *NA*. The whole frequency space can be covered by 21 sub-images for *NA* = 1.4, while as many as 75 images are required in case of *NA* =0.65. The required number of sub-images for nearly complete coverage increases approximately as NA^2. This suggests that there will be great advantage

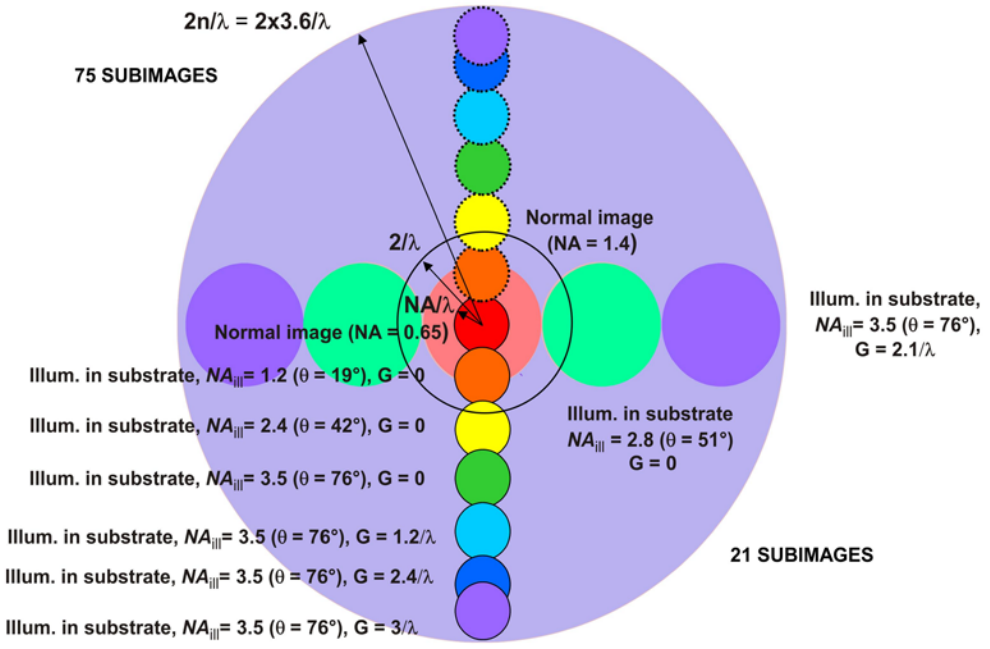

Fig. 3.2 Tiling strategy for high index substrate [example shown is n = 3.6 (Si at 1.06 μm)]. Collection *NA*'s are 1.4 and 0.65.

in knowing something about the image and its spectral content allowing image formation with less than complete coverage of the spatial frequency space. One situation where this

is clearly possible is in the inspection of silicon integrated circuits. The demands of manufacturable lithography at the nanoscale are putting great pressure on the range of patterns allowed in modern ICs, this is often referred to as lithography "friendly" design, which in general is forcing the patterns closer to periodic grating patterns. In turn, a lithography "friendly" circuit is a microscopy "friendly" circuit with a limited range of spatial frequencies, hence not requiring a complete coverage of spatial frequency space to reconstruct an image. In particular, the present examples used a binary geometric structure with the major spectral components along orthogonal axis. For more general objects, additional partial images covering all of frequency space inside the circle should be added.

Immersion lenses are not available at an NA corresponding to the refractive index of silicon (3.6-6.6). However an available immersion lens designed for more modest NA's of ~1.4 can be used with the addition of gratings to couple the higher spatial frequency light out of the substrate. An issue with the very high NA immersion lens is that these lenses typically have a very short working distance, which in turn will require a very thin substrate, or a specially designed objective.

3.1.2 Use of a thin overlayer for solid immersion immersion

The purpose of this discussion is to show the advantages and limitations of IIM in a new configuration, where a slab of high refractive index material is used as an effective solid-immersion medium (Fig. 3.3) to enhance the resolution up to the linear systems resolution limit of $\lambda/4n$. In what follows, we reveal a new regime for both half- and full-immersion IIM. Using very thin substrates (or overlayers) and thereby restricting the

propagation distance, higher absorption can be tolerated, allowing the use of shorter wavelengths. Then the resolution is improved by two factors: the shorter wavelength and the higher index of refraction within an absorption band. This approach provides resolutions that are not available to solid immersion microscopy approaches because of the need for a thick high-index solid immersion lens.

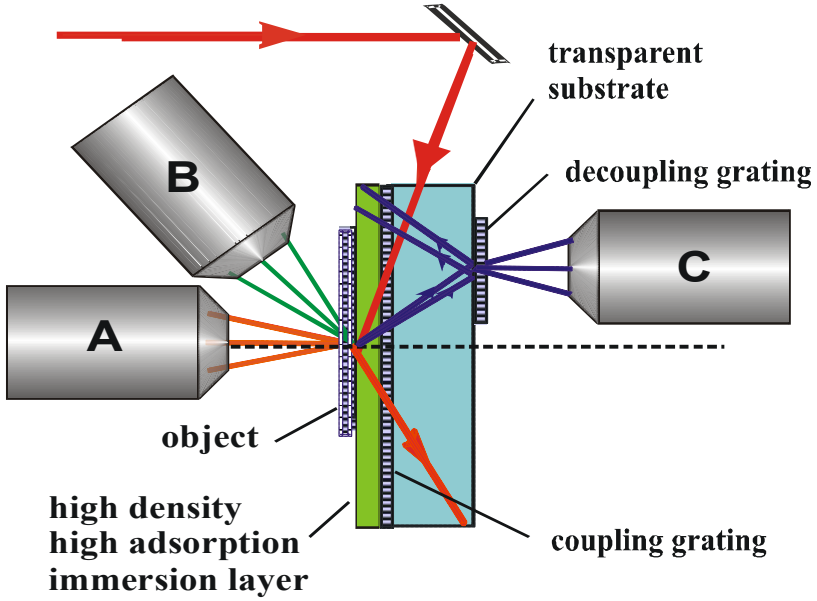

Fig 3.3. Advanced illumination/collection scheme allowing high-index-refractive material with high losses as solid immersion media.

Phase distortions of high frequency sub-images are inherent in the geometry of beam propagation in the immersion slab, requiring a phase restoration procedure. The resolution in this configuration depends not only on objective *NA* and *FOV*, but also on the captured part of the spectral information which is also a function of immersion slab refractive index and thickness. The criteria for evaluation of the ultimate *HP* limits for different immersion slab parameters and system field of view have been provided. The estimation shows that the minimum thickness of the immersion slab and the maximum

field-of-view of the optical system should be chosen to achieve the highest resolution with the smallest number of sub-images.

Other materials together with corresponding wavelengths in proximity to a material band-gap in combination with our method can also provide excellent results. Some possible wavelength/material combinations to explore are shown in Table 3.2. The columns labeled by n_{max} reflect the largest index transparent material of which we are

Table 3.2. Examples of possible combinations of materials and wavelength for enhanced resolution

λ (nm)	λ/4 (nm)	½–immersion ($\lambda/2(n_{max}+1)$);	Full-immersion $\lambda/4n_{max}$
690	173	72	47 (n = 3.7 AlSb)
633	158	74	48 (n = 3.30, GaP)
		65	41 (n = 3.87 AlSb)
		50	30 (n = 5.2 GaSb)
488	122	58	40 (n = 3.1, TiO_2)
		43	26 (n = 4.69, AlSb)
		44	27 (n = 4.5, Si)
193	48	34	27 (n = 1.8, Photoresist)
		31	23 (n = 2.1, Garnet)
		25	19 (n = 2.6, Si_3N_4)
		19	12 (n = 4.04, SiC)

length/material combination of 193 nm and SiC, but a more economical combination with somewhat lower resolution could be 488 nm and Si; longer wavelength for biology requires selecting a material out of III-V group of materials, for example 633 nm with GaSb or 690 nm with AlSb. Additional materials may further expand the available resolution.

3.2 Enhancements in hardware

Experimental setup improvements such as adding electrically controlled opto-mechanical elements such as shutters for the automatic beam blocks and rotation stages for mask rotation and changing tilt angle will allow a significant increase in the speed of taking images. Electronically controlled rotation stages will also allow adjustment of angles more precisely, which will lead to image reconstruction with higher quality. This is especially important for correct reconstruction of tilted images.

3.2.1 Elimination of dark fields and injection of reference beam

Evanescent illumination can be combined with structural illumination eliminating the need for access to the back focal plane. This moves the interferometer to the front of the objective lens and makes IIM readily adaptable to existing microscopes. We have already discussed two approaches to structured illumination:

a) Two plane waves incident on the sample - one at an extreme off-axis angle and one at an off-axis angle that is transmitted near the edge of the objective pupil (reference beam).

b) The off-axis plane wave incident on the sample and the reference beam inject-

ed between the object and the objective.

Each of these has some concerns: for case a) each of these waves produces diffracted information; sorting out the resultant overlapping images requires some access to the back pupil plane (to block the zero order of the illumination beam that is transmitted through the objective lens); for case b) the injection requires a beam-splitter which sacrifices working distance. To address these issues we are in the process of elaborating several techniques described below.

For example, guided-mode filters [Magnuson *et al*. 1992] (k-vector filters) provide an alternative approach for blocking zero order in structural illumination scheme. The basic idea is to fabricate a grating coupled waveguide to provide a high-resolution angular filter (Fig. 3.4) that can be designed to block the zero-order transmission just before the objective and transmit the diffracted information at all other angles (Fig. 3.5). Then by dithering the angular position or rotation it is possible to switch the zero-order on and off.

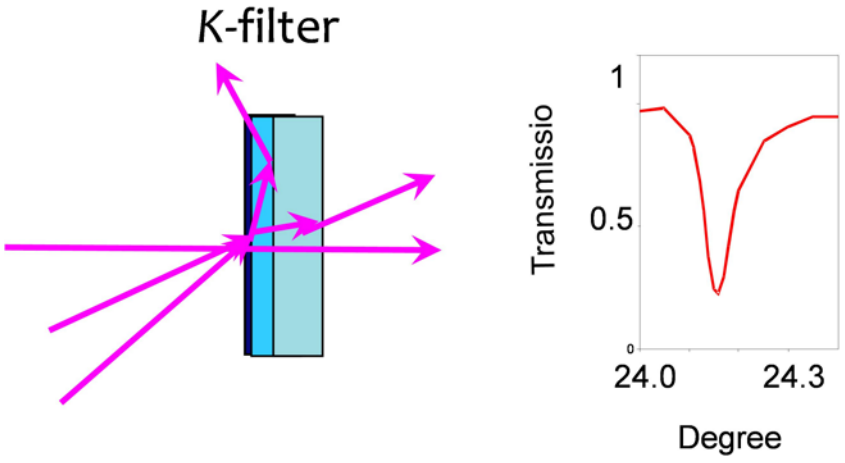

Fig. 3.4. K-vector filter schematic and characteristic of a SiN-on-glass guided mode resonance filter.

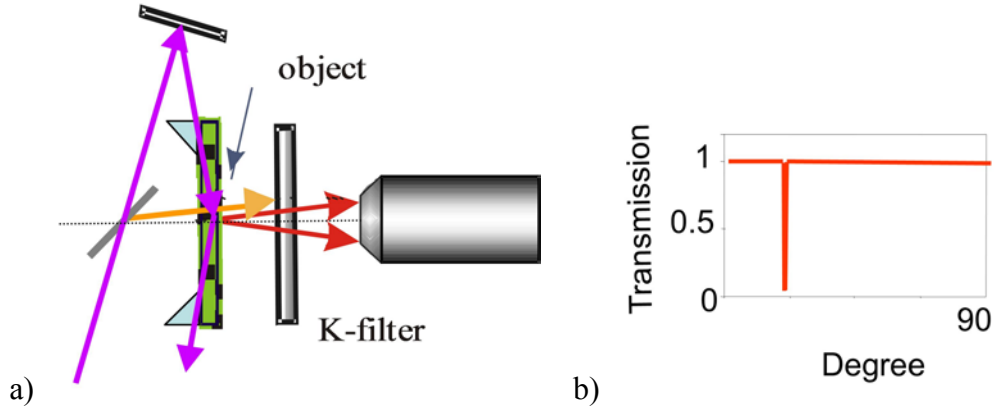

Fig. 3.5. Blocking of reference beam by k-vector filter.

Another possibility is to use a simple grating or grating on a waveguide instead of the beam-splitter to inject the reference beam before the objective as shown in Fig. 3.6. The grating should have a high enough spatial frequency pitch to avoid overlapping of images caused by high order difraction.

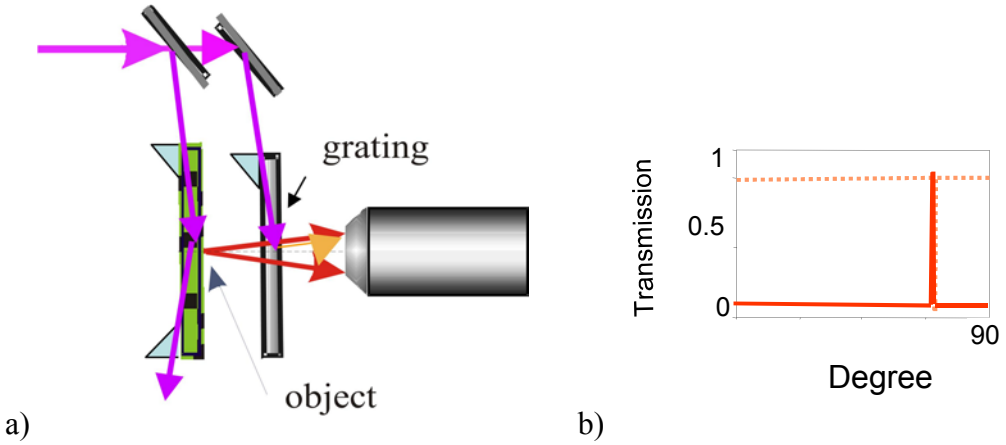

Fig. 3.6. Injection of reference beam with grating.

The advantage of this method is that it does not require switchable gratings or mechanical adjustment of the filter. Both structures will have only minimal impact on the

working distance and will not cause any significant aberrations because they could be manufactured as pellicles and mounted directly in front of and perpendicular to the objective lens.

3.2.2 Coupling into Immersion Slab

There are several techniques available to provide for the illumination through the substrate which should be investigated in future work. A sampling of these is shown in Fig. 3.7. A coupling through the side of the substrate is shown in Fig. 3.7(a). The side can be polished at an angle different from normal to the object surface (that is the substrate can be a prism). Fig. 3.7(b) shows a grating for coupling. In the figure the grating is on the top surface of the substrate (the same side as the object), alternatively it can be placed on the bottom side of the substrate. Fig. 3.7(c) shows a prism configuration. Since the propagation angle in the substrate is beyond the critical angle, the beam bounces from side to side as it progresses down the sample. For the bulk substrate, the position of the coupling element has to be adjusted so that the beam is incident on the top surface at the object position corresponding to the field of view of the collection objective. Also shown

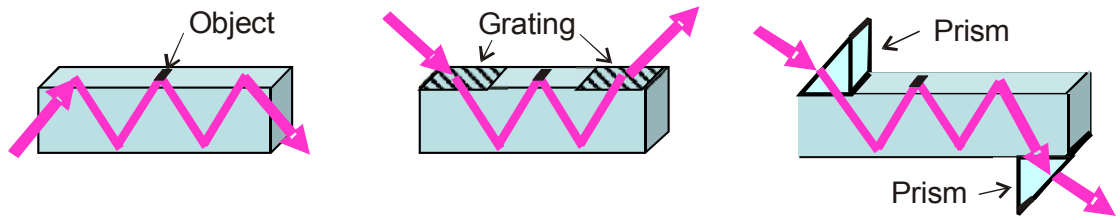

Fig. 3.7. Alternatives for coupling light for substrate illumination: end face, grating, prism.

in each of the figures is an additional coupling element that is used to extract the illumination beam from the substrate to minimize stray reflections, which can be particularly difficult to deal with in a coherent system (see below for a discussion of source coherence).

Another approach is to use a high index waveguide rather than a bulk substrate. Again, there are several techniques, well known to the integrated photonics research community, for injection of the illumination beam into the waveguide including prisms, gratings, and adiabatic tapers from larger waveguides or from fibers. A possible advantage of the use of a high-index waveguide is that it may be more compatible with the very short working distance of some high-NA objective lenses; the disadvantage is the filtering effect of the waveguide modal structure on the scattered light (some directions of scattering will be accepted by the waveguide and not transferred through). This suggests that a single-mode waveguide should be used when extraction of the scattered light through the waveguide is required.

3.2.3 Decoupling of high spatial frequency information out of an immersion slab

Fig. 3.8 represents an advanced schematic of capturing the light scattered from an object at steep angles into the substrate, beyond the total internal reflection angle. This light carries information on the higher spatial frequency structure within the object encoded in their amplitude and phase. Unless provision is made, this light is trapped by total internal reflection and is not collected. For convenience of representation, three separate diffracted bundles are shown, in reality there is a continuum of diffracted light with varying intensities and phases. Gratings are added at the top of the substrate to allow the

scattered light, impinging from the illuminated sample to exit the substrate and be collected. The use of decoupling gratings along with imaging interferometric microscopy is a major aspect of full-solid-immersion technique.

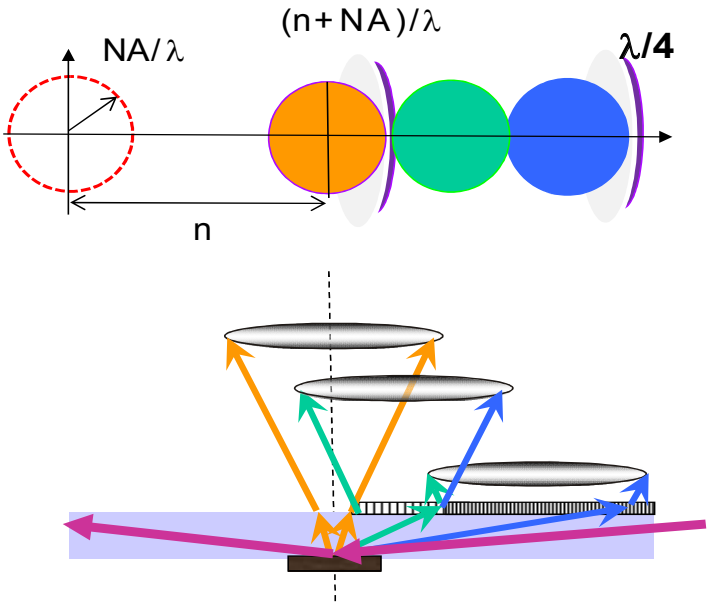

Fig. 3.8 Using gratings with different pitch for extraction of rays beyond total internal reflection for full-immersion configuration.

Clearly from the figure, significant phase (and amplitude) corrections are necessary. Appropriate phase correction for a single Fourier component in the plane of incidence can be done in accordance with Eq. 2.23.

In addition, there is a translation of the image associated with the high angle diffraction and the need to translate the lens to capture the relevant information. In this geometry, collection of light scattered close to 90° is not possible, but this information can be accessed if desired using a chamfered edge to the substrate with appropriate corrections.

Grating profiles have an impact on the extraction efficiency (how much of the

light incident from the substrate is transmitted across the interface and collected by the objective). In general, we are interested in using the minus-first-order component of the grating Fourier transform (corresponding to $2\pi/d$). A sinusoidal grating has components in its Fourier transform only at $\pm 2\pi/d$. A rectangular profile, which is commonly fabricated, has many more components that can lead to coupling of additional scattered image plane waves across the interface. For equal line:space gratings the second order (as well as other even orders) Fourier coefficient (at $\pm 4\pi/d$) vanishes, although for sufficiently deep gratings, comparable to the wavelength, additional coupling terms arise. The third order terms (at $\pm 6\pi/d$) are always present for rectangular grating profiles. This can give rise to multiple coupling orders which will lead to artifacts in the sub-images. For many arrangements, this is not an issue because of the spatial separation of the scattered spatial frequency information at the bottom of the substrate. This is, the bottom substrate plane is separated from the object plane and the different spatial frequency components, propagating at different angles, have separated to some extent by the time they reach this plane. If the thickness of the substrate is significantly larger than the field of view (illuminated aperture at the image plane), this separation will be large enough to avoid issues associated with higher-order coupling at the bottom surface extraction grating.

3.2.4 Coherence length of sources

So far the discussion has been for fully coherent sources with coherence lengths much greater then sample dimensions. The He-Ne laser we have used for the initial demonstrations has a coherence length of many cm, much larger than the sample, substrate, and substrate to objective lens distances. This long coherence length makes the experimental

arrangement simpler, since it is not necessary to critically match the interferometer lengths between the objective arm and the zero-order reinjection arm. However, it does increase the spurious speckle effects associated with stray light (flare) and with light that reflects between the various optical components. These effects can be mitigated by choosing a source with sufficient coherence for the IIM measurements but insufficient coherence for a millimeter scaled Fabry-Perot effects, for example between the front and back sides of the substrate, or between the substrate and the objective entrance surface. Since these dimensions are very different, ~ micrometer scale for the sample to several mm for the substrate thickness and the substrate-objective distance, it should be possible to minimize unrelated Fabry-Perot effects while retaining all of the resolution of IIM.

3.3 Enhancements in algorithms

The full apparatus of digital image processing is quite rich and many additional techniques will find application in IIM. An advantage of IIM is the availability of partial images allowing signal-processing enhancements. One example is the subtraction of dark-field images; another is the use of Fourier-transform filtering techniques to eliminate double coverage of the same spectral components in two images. More investigations should be carried out for the dependence of image quality improvement on applying different types of filters. Using different apodizing filters [Kuznetsova *et al.* 2007, Chang *et al.* 2012] electronically may improve the quality especially in the case where overlapping sub-images are combined and filtering range was not estimated accurately enough.

In chapter 2, it was shown that tilting the mask leads to image distortion due to

the non-uniaxial optical system, and thus restoration is necessary before image reconstruction. An algorithm for image restoration was developed and applied to experimental results. We recalculated frequencies in Fourier space. The resulting frequencies are no longer on a regular grid and therefore not suitable for an inverse FFT. So, a Fourier sum with off-grid frequencies was used for inverse Fourier transform, which gives us better results for the whole field restoration in comparison with recalculated frequencies using approximation to nearest grid points. However, the nearest-point method combined with artificial increasing number of pixels around the image (4x in off-axis direction) gave numerically better results by certain circumstances. The possibility of solving the defocusing problem using this approach has been demonstrated. The field of view increases with object plane tilt angle. Thus, it will be important to estimate the possible size of the restored field of view. The quality of the images was not very high due to the lack of precision in the mask and the illumination beam angle adjustments. Development of algorithms for determination of inclination angle with high precision would allow defocused tilted pictures to be restored with higher quality. Exploration of different algorithms, such as using different interpolation functions and approximations, also may improve restored image quality.

In order to choose the best algorithm we need to compare reconstructed images. The images were compared with corresponding models, and quality of images was estimated by a simple MSE method. Using different weights w_i for different pixels [Tridhavee *et al.* 2005] we can estimate the quality of images, with some emphasize on selected features, by an extended MSE method:

$$MSE = \frac{1}{N}\sum_i w_i (I_i - I_i')^2 \tag{3.1}$$

Also, using different weights of different exposures in the process of reconstruction will allow different features to be seen with different contrast, which can be useful for object investigation.

Other methods of image quality estimation can be combined together with MSE criteria. The important information from the images of microchips can be recognition of whether the lines are continuous or they are broken somewhere. It may also be important to see whether there is an unwanted (or desired) "bridge" between the lines, or whether the lines are well separated. The mean-square deviation of the line length estimated by different techniques can also give a quantitative criterion for the image quality. In particular, the method will be useful for analysis of fabricated micro-objects where the desired result is known a-priory, for example, microchips.

3.4 Fields of Application

3.4.1 Binary objects in far field

IIM is very useful for inspection of gratings and masks with *CD* between 35 nm (using liquid immersion with n=1.7 and objective *NA*=1.4, λ=212nm) and 200 nm, which are not possible to see using conventional microscopes. Fast object investigation is very important for lithography process control.

Proposed technique is easily combined with phase shift interferometry [Shaked 2009]. Then, surface mapping with lateral resolution about 35 nm and longitudinal resolution of a few nanometers can be done within seconds. Phase measurements are

readily available since the zero-order beam is independently accessible and can be advanced/retarded independently of the diffracted beams. For example, this will allow detailed microscopy of phase-shift lithography masks, which is difficult with traditional microscopy.

3.4.2 Shallow surface investigations (e.g. cell membranes)

Much research in biology is focused on membrane investigations, which can be successfully done using solid immersion IIM. Evanescent waves allow lateral resolution about 30 nm and longitudinal resolution about 1 nm. The overall noise will be reduced because observation layer is very thin (on the order of 100 nm).

3.4.3 Multiple wavelength illumination as an exciting direction for 3-D imaging

To date, our investigations have been restricted to 2D objects (e.g. Cr on glass masks). At a single frequency scattering from multiple objects in multiple z-planes (displaced along the optical axis of the objective) is indistinguishable and makes imaging of 3D objects problematic. 3D imaging is necessary to observe a majority of biological objects. As we discussed above (section 1.3.4) IIM, as single-side-band system with relatively long coherence length, has a quasi-unlimited depth of focus. Thus, it is impossible to record separate information from a thin in-focus layer without severe contamination by information from other (defocused) layers. This problem can be solved by tomography which is image observation at different angles or by using a set of different wavelength. Tomography is well established, but for initial understanding of our multi-wavelength concept we provide below a simple model for sectioning of just two longitudinally separated images using illuminations with two different wavelengths (Fig. 3.9). Both

objects are nested "ell's", but object B has slightly different pitches and is rotated relative to object A for the ease of identification. Focusing on the object A and using wavelength $\boldsymbol{\lambda_1}$ we also record defocused image B.

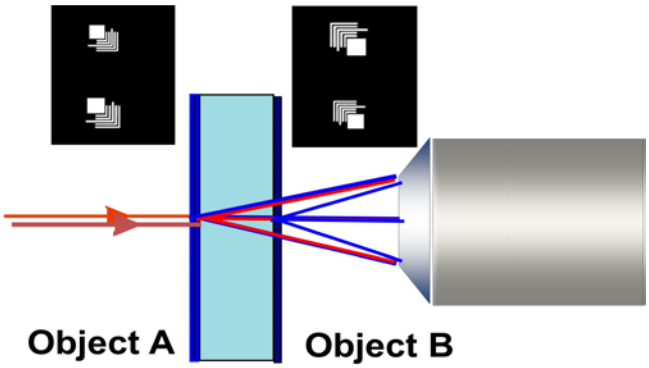

Fig. 3.9. Configuration for sectioning a 3D imaging. Object A is in focus; object B is out of focus. Object B has slightly different pitches and is rotated relative to object A for ease of identification.

Here, for simplicity, we assume a weakly-scattering sample, which means that scattering from both objects does not significantly perturb the incident light and multiple scattering involving both object planes is negligible. This is not too strong a restriction since many (if not most) biological samples are weak-scatterers. Under these conditions, each spatial Fourier component $\mathcal{C}_{qg}$ of the total image C can be described as:

$$\mathcal{C}_{qg} = \mathcal{A}_{qg} + \mathcal{B}_{qg} e^{i\varphi_{1,qg}} , \tag{3.2}$$

where $\varphi_{1,qg} = 2\pi n \Delta z s_{1,qg}/\lambda_1$ – is a defocusing term, e.g. the difference in phase occurring as a result of the separation Δz. Here $s_{1,qg} = \sqrt{1 - {f_{1,q}}^2 - {f_{1,g}}^2}$ and f_q, f_g are normalized shifted spatial frequencies (e.g. $f_{1,q} = \lambda_1/d_x - f_{ill}$). $\mathcal{A}_{qg}$ and $\mathcal{B}_{qg}$ are spatial Fourier coefficients of the original objects in sense of Eq. (2.8); n is the refractive index of the

medium between the two objects.

Using a different wavelength λ_2, we can describe the spatial Fourier coefficients of the recorded image *D* as:

$$\mathcal{D}_{qg} = \mathcal{A}_{qg} + \mathcal{B}_{qg} e^{i\varphi_{2,qg}} \tag{3.3}$$

Solving the system of equations (3.2) and (3.3) we can reconstruct the Fourier coefficients of image *B*:

$$\mathcal{B}_{qg} = \frac{\mathcal{C}_{qg} - \mathcal{D}_{qg}}{e^{i\varphi_{1,\mathrm{qg}} - e^{i\varphi_{2,\mathrm{qg}}}}} \tag{3.4 }$$

and similarly for image *A*.

In a model calculation we applied Eqs. (3.2) – (3.4) to a high frequency IIM image as shown in Fig. 3.10. Focused image *A* is in Fig 3.10(a); defocused image *B* is shown in Fig. 3.10(b)); the simulated 'recorded' combination of images is in Fig. 3.10(c). High frequency sub-images of the objects *A* and *B* after reconstruction are shown in Fig 3.10(d) and Fig. 3.10(e), correspondingly.

So far so good in a noiseless ideal world, however in a realistic experiment we are confronted with the subtraction of two almost identical, but noisy, images. It is clear from Eq. (3.4) that the quality of the separated images will be strongly dependent on the signal-to-noise ratio.

To demonstrate our ability to account for a defocusing term, we recorded in our setup a defocused image which was restored electronically. Pictures of recorded defocused high frequency image and electronically refocused one with corresponding models and crosscuts are shown in Fig. 3.11.

Rewriting Eqs. 3.2–3.4 for general case where *N* sectioning layers are required results in the need to record *N* sub-images with *N* different wavelengths. Eqs. 3.2-3.3 take

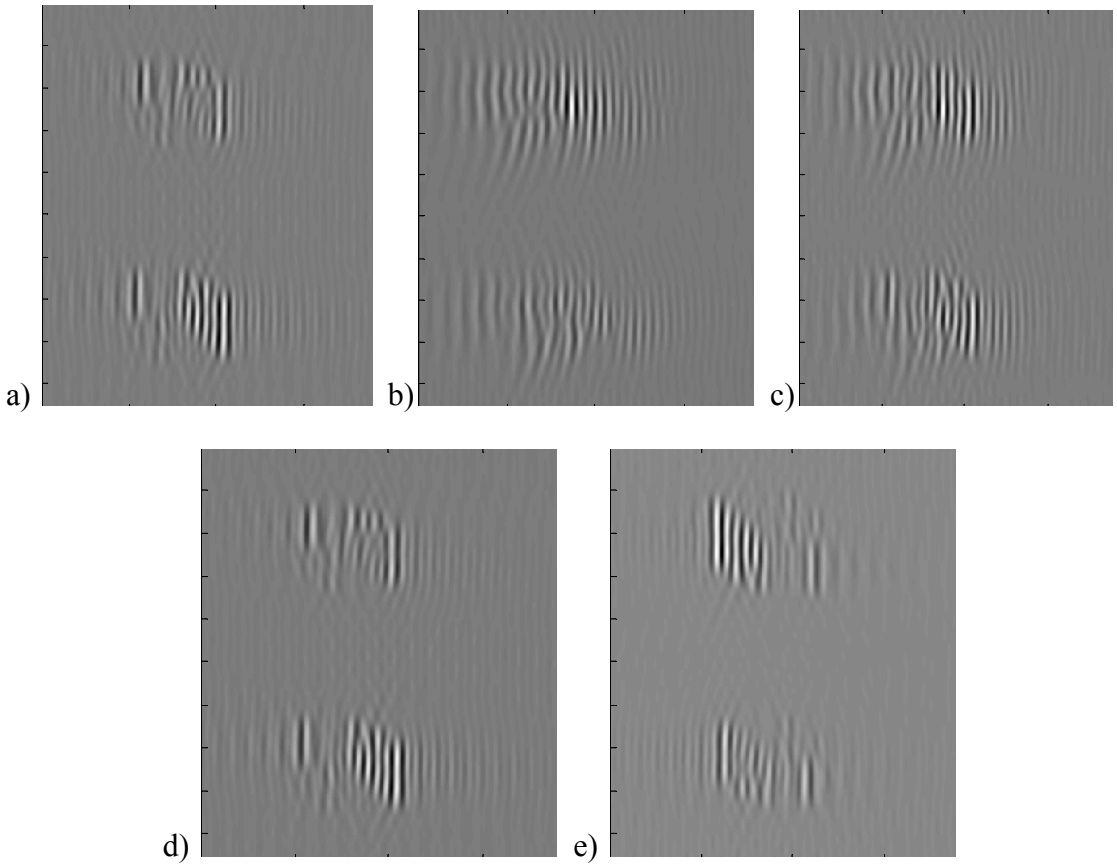

Fig. 3.10 High frequency images a) A in focus, b) Defocused B, c) Sum of two images: A + Bexp(iφ(λ1)) = C, d) Restored A, e) Restored B

the form of a system of linear equations:

$$\left\|\Psi_{qg}\right\| * \mathcal{A}_{qg} = \mathcal{D}_{qg} \ , \tag{3.5}$$

where $\mathcal{A}_{qg}$ is a vector of N coefficients at a particular frequency f_{qg} from the N layers in the object, each longitudinally separated by Δz_p; ; $\underline{D_{qg}}$ is a vector of N coefficients at a particular frequency f_{qg} from the N sub-images, each recorded with a unique wavelength; transfer matrix Ψ_{qg} is a N-by-N matrix of defocusing elements corresponding to the longitudinal position of a particular layer and the wavelength of a particular sub-image defined as:

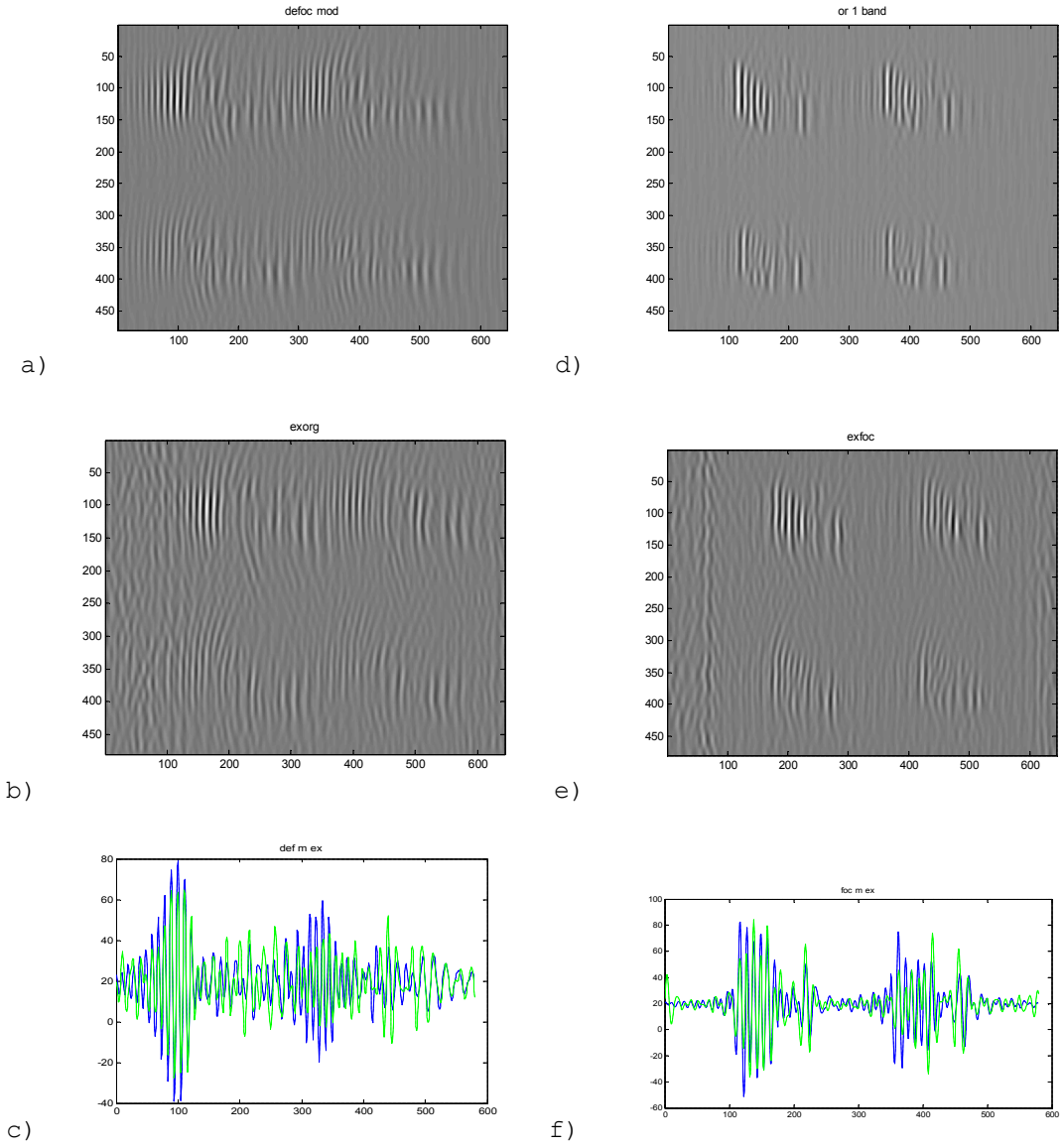

Fig. 3.11. a) Defocused model, b) defocused experimental resulted, c) crosscuts of defocused model(blue) and experimental result, d) reconstructed model(green), e) reconstructed experimental result, f) crosscuts of reconstructed model and experimental result

$$\psi_{\mathrm{jp,qg}=} e^{i\frac{2\pi}{\lambda_{\mathrm{j}}} s_{j,qg} \Delta Z_p} \quad . \tag{3.6}$$

Here $\Delta Z_p = \sum_0^p \Delta z_p$; assuming equal spacing $\Delta Z_p = p\Delta z_p$.

The formal solution of Eq. (3.5) is straightforward:

$$\mathcal{A}_{qg} = \left\|\Psi_{qg}\right\|^{-1} * \mathcal{D}_{qg} \,, \tag{3.7}$$

and it is easy to calculate as long as matrix Ψ_{qg} is well-conditioned. Evidently the degree of degeneracy of the matrix Ψ_{qg} is closely related to the magnitude of the difference of the defocusing terms of two adjacent separation layers (see the denominator of Eq. 3.4):

$$e^{i\varphi_{1,qg}} - e^{i\varphi_{2,qg}} = e^{i\overline{\varphi_{qg}}}\left(e^{i\frac{\Delta\varphi_{qg}}{2}} - e^{-i\frac{\Delta\varphi_{qg}}{2}}\right) = 2ie^{i\overline{\varphi_{qg}}}sin\frac{\Delta\varphi_{qg}}{2}. \tag{3. 8}$$

The larger the absolute value of the denominator the more robust the solution to the impact of noise on the separation of the images. The maximum is achieved when $\Delta\varphi_{qg}/2 = \pi/2$. Approximating terms $s_{1,qg}$ and $s_{2,qg}$ as $1\text{-}f_{1,q}\text{-}f_{1,g}$ as a consequence of the small objective *NA*, we get :

$$\Delta\varphi_{qg} \sim 2\pi n\Delta z\left(\frac{1}{\lambda_1} - \frac{1}{\lambda_2}\right) = 2\pi n\Delta z\frac{\Delta\lambda}{\lambda_2\lambda_1} \sim 2\pi n\Delta z\frac{\Delta\lambda}{\lambda^2} = \pi \tag{3.9}$$

Thus, we have a kind of 'uncertainty' relation for estimating the optimal range of wavelengths for a given axial resolution:

$$\Delta z\Delta\lambda_{\text{range}} = \frac{\hat{\lambda}^2}{2n} \tag{3.10}$$

Please note that $\Delta\lambda_{range}$ is the difference of maximal and minimal wavelengths used in the system (range of used wavelengths), but not an incremental step from a sub-image to the next one which is related to the $\Delta\lambda_{range}$ and number of desired sectioned layers *N* as follows:

$$\Delta\lambda_{inc} = \frac{\Delta\lambda_{range}}{N} \quad ; \tag{3.11}$$

or

$$\Delta\lambda_{inc} \sim \frac{\hat{\lambda}^2}{2nN\Delta z} \tag{3. 12}$$

So, if required resolution is say 120 nm, then wavelength range for the best results is

estimated as

$$\Delta\lambda_{range} \sim \frac{500^2}{2*120} = 1041 \text{ nm} .$$

The range is of the same order as the wavelength range for given resolution in OCT microscopy [Schmitt 1999], where longitudinal resolution and wavelength range are connected as $\Delta z \Delta\lambda_{\text{range}} = 2ln2\frac{\hat{\lambda}^2}{\pi n}$.

The information content in the transfer matrix (3.6) can be increased by including angular propagation information which allows us to add tomographic reconstruction to significantly reduce the necessary wavelength range and to increase the robustness of inversion process. The transfer matrix becomes much more complex since we are dealing with a higher-dimensional case, because every spatial frequency is now propagating under several different spatial angles for different illumination conditions.

In next step the weakly-scattering restriction can be removed for matrices that include this angular propagation information, since a contribution of multiple scattering, phase change and attenuation by spatial points along the propagation direction can be added for every frequency. Thus, we can deal with objects which are transparent enough to be recorded within good signal-to-noise ratio, but which cannot be considered as weakly-scattering; e.g. where multiple scattering has to be considered.

The realization of this 3D imaging technique requires establishing a low noise optical system including (but probably not limited to) determining the best reference object specifically suitable for 3D imaging in order to precisely adjust focus, reference beam angle and phase; measure phase transfer function of the entire optical system including chromatic aberrations; reduce as much as possible coherence length of sources. Another task is to choose an optimal algorithm for inversion the phase matrix.

3.4.4 Microscopy with Chemical Analyses (CARS)

The above discussion is pertinent to structural (reflection/transmission) microscopy that is sensitive to refractive index variations of the sample. Chemical information can be accessed using coherent anti-Stokes Raman scattering (CARS) spectroscopy. In CARS microscopy, two coherent sources at frequencies ω_1 and ω_2 are incident on the sample, the frequency difference, ω_1-ω_2, is tuned through sample material resonances and the anti-Stokes signal at $2\omega_1$-ω_2 is detected. This anti-Stokes signal is at higher frequency than either of the incident beams, which aids in discrimination against any fluorescent signals from the sample, which are at lower energy than the excitation. Since this is a coherent process, the concepts of IIM are directly applicable. In practice, we will need to generate a reference CARS beam to act as our reference beam in a suitable, non-resonant fashion, a traditional four-wave mixing arrangement is suitable for this generation. The beauty of the approach is that particular molecules (protein, DNA, etc.) or specific chemical bonds can be targeted without need to induce a specific marker into the sample. That gives a huge advantage for in-vivo investigations.

More investigations should be performed to find out what signal level can be obtained for realistic samples. If desired signal-to-noise ratio can be achieved than IIM can be very powerful tool for biological investigations.

3.4.5 Application in non-optical systems.

The extension of the effective numerical aperture demonstrated in the IIM also should be applicable to other waves such as electrons and atoms [Berkhout *et al.* 1989, Doak *et al*. 1999, Balykin *et al.* 2005]. It will be important to investigate application of IIM

principles to electron microscopy and x-ray diffraction as they can be used in any problem that involves capture of a wide range of spatial spectral components exceeding the band pass of a limiting aperture. Conventional focusing elements (lenses and mirrors) with large aperture are available in relatively narrow range of wavelengths, between 200 nm and 4000 nm; for shorter wavelengths, only low *NA* elements are available. Also, the focusing element for an atomic imaging system [Kouznetsov *et al.* 2006] is expected to work with *NA* of the order of several miliradian. If an appropriate coherent source was found, the IIM method could greatly extend the limit of resolution of such imaging systems.

3.5 Summary.

An important aspect of IIM is that frequency space is parsed into small, manageable pieces so that it is not necessary to provide the full *NA* in a single image. Existing immersion microscopy lens are limited to $NA \sim 1.4$, not only by the available indices of refraction, but by the difficulty of making a single diffraction limited objective at higher *NA* with acceptable aberrations. With IIM, we can in principle reach an *NA* as large as 5 (see Table 3.2). It is worthwhile to note that IIM provides an important advantage over conventional immersion microscopy techniques. Since only a relatively small region of frequency space ($\sim NA/\lambda$) is recorded in each sub-image, the aberration correction requirements for the objective lens are dramatically reduced.

The resolvable dimensions for typical source wavelengths approach typical SEM resolutions – down to tens of nanometers - without requiring vacuum and indeed being fully compatible with water immersion. These resolutions are well beyond the current

established perceptions of microscopy capabilities and suggest that advances in optical microscopy can yet yield improvements that will have important impacts across a broad swath of science and technology.

The place of IIM among other kinds of microscopy is shown in Fig 3.12 where they are located according to their resolution and field of view. It is clear that IIM allows high resolution and large field of view at the same time using modest equipment.

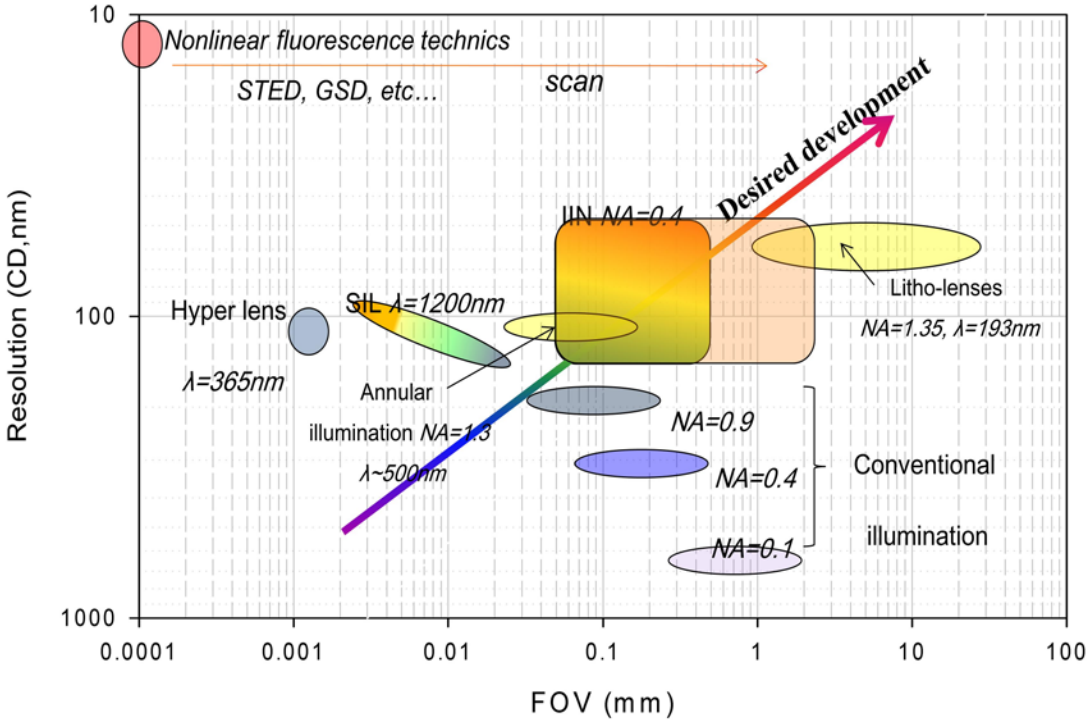

Fig. 3.12 Place of IIM in microscopy world.

References

Abbe, E. 1873. Beiträge zur theorie des mikroskops und der mikroskopischen wahrnehmung. Arch. Mikrosk. Anat. Entwicklungsmech. **9**, 413 – 468. [English translation in SPIE Milestone Series. MS178].

Alexandrov, S. A. and D. D. Sampson. 2008. Spatial information transmission beyond a systems diffraction limit using optical spectral encoding of the spatial frequency. J. Opt. A – Pure Appl. Opt. **10,** 025304.

Alexandrov, S. A., T. R. Hillman, and D. D. Sampson. 2005. Spatially resolved Fourier holographic light scattering angular spectroscopy. Opt.,Lett. **30**, 3305.

Alexandrov, S. A., T. R. Hillman, T. Gutzler, and D. D. Sampson. 2006. Synthetic aperture Fourier holographic optical microscopy. Phys. Rev. Lett. **97**, 168102.

Alexandrov, S. A., T. R. Hillman, T. Gutzler, and D. D. Sampson. 2007. Digital Fourier holography enables wide-field,superresolved, microscopic characterization. Opt. Photonics News **18,** December 29.

Axelrod, D. 2001. Total internal reflection fluorescence microscopy in cell biology. Traffic **2**, 764-774.

Balykin, V., V. Klimov, V. Letokhov. 2005. Optics and Photonics News. Atom nanooptics. 16, 44.

Becherer, R. J. and G. B. Parrent. 1967. Nonlinearity in optical imaging system. J. Opt. Soc. Amer. **57**, 1479.

Berkhout, J. J., O. J. Luiten, I. D. Setija, T. W. Hijmans, T. Mizusaki and J. T. M. Walraven. 1989. Quantum reflection: Focusing of hydrogen atoms with a concave mirror Phys. Rev. Lett. 63 1689-92

Betzig, E., G. H. Patterson, S. Sougrat *et al.* 2006. Imaging intracellular fluorescent proteins at nanometer resolution. Science **313**, 1642.

Bewersdorf, J., R. Schmidt and S. W. Hell, 2006, Comparison of I5M and 4Pi-microscopy, J. Microsc. **2222**, 105.

Born, M. and E.M. Wolf. 1999. Principles of Optics, Cambridge University Press.

Brueck , S.R.J. and X. Chen. 1999. Experimental comparison of off-axis illumination and imaging interferometric lithography - approaching the resolution limits of optics. Jour. Vac. Sci. Tech. **B17**, 921-929.

Cai, W. and V. Shalaev. 2009. Optical Metamaterials: Fundamentals and Applications. Springer-Verlag.

Campion, A. and P. Kambhampati. 1998. Surface-enhanced Raman scattering. Chem. Soc. Rev. **27**, 241- 250.

Chang, S., D. Wang ; Yu. Wang ; J. Zhao and L. Rong. 2012. Improving the phase measurement by the apodization filter in the digital holography. *Proc. SPIE* 8556, Holography, Diffractive Optics and Applications V, 85561S.

Chen, X. and S. R. J. Brueck. 1998. Imaging interferometric lithography: A wavelength division multiplex approach to extending of optical lithography. Jour. Vac. Sci. Tech. **B16**, 3392-3397.

Chen, X. and S. R. J. Brueck. 1999. Imaging interferometric lithography - approaching the resolution limits of optics. Opt. Lett. **24**, 124-126.

Coe, J. V., J. M. Heer, S. Teeters-Kennedy, H. Tian, and K. R. Rodriquez. 2008. Extraordinary transmission of metal films with arrays of subwavelength holes," Ann.

Rev. Phys. Chem. **59**, 179-202.

Courjon, D. 2003. Near-Field Microscopy and Near-Field Optics. London: Imperial College Press.

Cox, I. J. and J. R. Sheppard. 1986. Information capacity and resolution in an optical system. J. Opt. Soc. Am. **A3**, 1152–1158.

Cragg, G. E. and P. T. C. So. 2000. Lateral resolution enhancement with standing evanescent waves. Opt. Lett. **25**, 46-48.

Cubukcu, E., E. A. Kort, K. B. Crozier and F. Capasso. 2006. Plasmonic laser antenna. 2006. Appl. Phys. Lett. **89**, 093120.

Curlander, J. C. and R. N. McDounough. 1991. Synthetic Aperture Radar, Systems and Signal Processing. , John Wiley & Sons, New York.

Davis, B. J., D. L. Marks, T. S. Ralston, P. S. Carney, and S. A. Boppart. 2008. Interferometric synthetic aperture microscopy: computed imaging for scanned coherent microscopy. Sensors **8**, 3903-3931.

Decker, A., Y. Pao, and P. Claspy. 1978. Electronic heterodyne recording and processing of optical holograms using phase modulated reference waves. Appl. Opt. **17**, 917–921.

Denk, W., J.H. Strickler, W.W. Webb. 1990. Two-photon laser scanning fluorescence microscopy. Science **248**, 73.

Doak, R.B., R.E. Grisenti, S. Rehbein, G. Schmahl, J.P. Toennies and C. Woll. 1999. Towards Realization of an Atomic de Broglie Microscope: Helium Atom Focusing using Fresnel Zone Plates. Phys. Rev. Letts. 83, 4229-32

Donnert, G., J. Keller, R. Medda *et al.* 2006. Macromolecular-scale resolution in

biological fluorescence microscopy. Proc. Natl. Acad. Sci. **103**, 11440-11445.

Dubois, A., L. Vabre, and A. C. Boccara. 2001 . Sinusoidally phase-modulated interference microscope for high-speed high-resolution topographic imagery. Opt. Lett. **26**, 1873-1875.

Ebbesen, T. W., H. J. Lezec, H. F. Ghaemi, T. Thio, and P. A. Wolff. 1998. Extraordinary optical transmission through sub-wavelength hole arrays. Nature **391**, 667-669.

Engheta, N. and R. W. Ziolkowski. 2006. Metamaterials – Physics and Engineering Explorations. New York: John Wiley and Sons.

Fong, Y. C. and S. R. J. Brueck. 1992. Confocal photoluminescence: a direct measurement of semiconductor carrier transport properties. Appl. Phys. Lett. **61**, 1332-4.

Fong, Y. C., E. A. Armour, S. D. Hersee and S. R. J. Brueck. 1994. A confocal photoluminescence study of MOCVD growth on patterned GaAs substrates. Jour. Appl. Phys. **75**, 3049-3055.

Françon, M. 1952. Amélioration de la reśolution d'optique. Nuovo Cimento, Suppl. **9**, 283–290.

Frieden, B. R. 1983. Probability, Statistical Optics and Data Testing. Springer-Verlag.

Gensch, T. 2004. Two-Photon Microscopy. http://www.fz-juelich.de/ibi/ibi-1, (accessed 02/07).

Goodman, J. W. 1985. Statistical Optics, New York: John Wiley and Sons.

Goodman, J. W. 1998. Introduction to Fourier Optics, 2nd Ed., New York: John Wiley and

Sons.

Göppert-Mayer M. 2009 (reprinted) Elementary processes with two quantum transitions, Annalen der Physik **18**, 466.

Granero, L. , V. Micó, Z. Zalevsky, and J. García. 2009. Superresolution imaging method using phase-shifting digital lensless Fourier holography. Opt. Exp. **17**, 15008-15022.

Grilli, S., P. Ferraro, S. De Incola, A. Finizio, G. Pierattini, and R. Meucci. 2001. Whole optical wavefields reconstruction by digital holography. Opt. Exp. **9**, 294–302.

Gu, M. 2000. Advanced Optical Imaging Theory, Springer-Verlag.

Guo, P. and A. J. Devaney. 2004. Digital microscopy using phase shifting digital holography with two reference waves. Opt. Lett. **29**, 857–859.

Gustafsson, M. G. L., D. A. Agart and J. W. Sedat. 1999. I^5M: 3D widefield light microscopy with better than 100 nm axial resolution. Journal of Microscopy **195,** 10-16.

Gustafsson, M. G. L. 2000. Surpassing the lateral resolution limit by a factor of two using structured illumination microscopy. J. Microsc. **198**, 82-87.

Gustafsson, M. G. L. 2005. Nonlinear structured-illumination microscopy: wide-field fluorescence imaging with theoretically unlimited resolution. Proc Natl. Acad. Sci **102**, 13081-13086.

Haddad, W. S., D. Cullen, J. C. Solem *et al.* 1992. Fourier transform holographic microscope. Appl. Opt. **31**, 4973–4978.

Heintzmann, R. and G. Ficz. 2006. Breaking the resolution limit in light microscopy. Brief. in Func. Genom. And Proteom. **5**, 289-301.

Hell, S. W. 2007. Far-field optical nanoscopy (review). Science **316**, 1153-1158.

Hell, S. W. 2009. Microscopy and its Focal Switch. Nature–Meth. **6**, 24- 32.

Hell, S.W. and E.H.K. Stelzer, 1992. Fundamental improvement of resolution with a 4Pi-confocal fluorescence microscope using two-photon excitation. Opt. Comm. **93**, 277.

Hell, S.W. and J. Wichmann. 1994. Breaking the diffraction resolution limit by stimulated emission: stimulated-emission-depletion fluorescence microscopy," Opt. Lett. **19**, 7809.

Hess, S. T., T. P. K. Girirajan and M. D. Mason. 2006. Ultra-high resolution imaging by fluorescence photoactivation localization microscopy. Biophys. Jour. **91**, 4258-4272.

Hillman, T. R., T. Gutzler, S. A. Alexandrov, and D. D. Sampson. 2009. High-resolution, wide-field object reconstruction with synthetic aperture Fourier holographic optical microscopy. Opt. Exp. **17**, 7873.

Hopkins, H. 1955. The frequency response of a defocused optical system. Proc. Royal Soc. *London* **A231**, 91.

Hopt, A., E. Neher. 2001. Highly nonlinear photodamage in two-photon fluorescence microscopy. Biophys. J. **80**, 2029.

Huang, F., S. L. Schwartz, J. M. Byars, and K. A. Lidke. 2011. Simultaneous multiple-emitter fitting for single molecule super-resolution imaging. Biomed. Opt. Express 2(5), 1377–1393.

International Technology Roadmap for Semiconductors (ITRS) at www.public.itrs.net, (accessed 11/2009).

Ippolito, S. B., A. K. Swan, B. B. Goldberg, and M. S. Ünlü. 2000. High resolution

subsurface microscopy technique. Proceedings of LEOS, Annual Meeting, Vol. 2, 13-16 November, pp. 430-431.

Kartashev, A. I. 1960. Optical system with enhanced resolving power. Opt. Spectrosc. **9**, 204–206.

Klein, V. and T. E. Furtak. 1986. Optics. New York: John Wiley and Sons.

Kouznetsov, D., H. Oberst, K. Shimizu, A.Neumann, Y. Kuznetsova, J.F. Bisson, K. Ueda, S.R.J. Brueck. 2006. Ridged atomic mirrors and atomic nanoscope. J.Phys. B., v39, 1605-1623.

Köklü, F. H., S. B. Ippolito, B. B. Goldberg, and M. S. Ünlü. 2009. Subsurface microscopy of integrated circuits with angular spectrum and polarization control. Opt. Lett. **34**, 1261-3.

Kreis, T. 2005. Hankbook of holographic interferometry: optical and digital methods. Wiley-VCH Verlag GmbH & Co. KGaA, Weinheim.

Kuznetsova, Y., A. Neumann and S. R. J. Brueck. 2007. Imaging interferometric microscopy – approaching the linear systems limits of optical resolution. Opt. Exp. **15**, 6651-6663.

Kuznetsova, Y., A. Neumann and S. R. J. Brueck. 2008. Imaging interferometric microscopy. Jour. Opt. Soc. Amer. **A25**, 811-822.

Kuznetsova, Y., A. Neumann and S.R.J. Brueck. 2012. Solid-Immersion Imaging Interferometric Nanoscopy to the Limits of Available Frequency Space. Jour. Opt. Soc. Amer. A29, 772-781.

Lai, S. and M. A. Neifeld. 2000. Digital wavefront reconstruction and its application to

image encryption. Opt. Commun. **178**, 283–289.

Lai, S., B. King, and M. A. Neifeld. 2000. Wave front reconstruction by means of phase-shifting digital in-lineholography. Opt. Commun. **173**, 155–160.

Le Clerc, F., M. Gross, and L. Collot. 2001. Synthetic aperture experiment in the visible with on-axis digital heterodyne holography. Opt. Lett. **26**, 1550–1552.

Lee, H., Z. Liu, Y. Xiong, C. Sun and X. Zhang. 2007. Development of optical hyperlens for imaging below the diffraction limit. Opt. Exp. **15**, 15886.

Leith, E. N. 1990. Small-aperture, high-resolution, two-channel imaging system. Opt. Lett., **15** 885–887.

Leith, E. N., D. Angell, and C.-P. Kuei. 1987. Superresolution by incoherent-to-coherent conversion. J. Opt. Soc. Am. **A4**, 1050–1054.

Lidke, K. A. 2012. Super resolution for common probes and common microscopes. Nature Methods 9. 139–141.

Liu, Z., H. Lee, Y. Xiong, C. Sun and X. Zhang. 2007. Far-field optical hyperlens magnifying sub-diffraction-limited objects. Science **315**, 1686.

Lohmann, A. W. and D. P. Parish. 1964. Superresolution for nonbirefringent objects. Appl. Opt. **3**, 1037–1043.

Lukosz, W. 1967. Optical systems with resolving powers exceeding the classical limit. II. J. Opt. Soc. Am. **57**, 932–941.

Magnuson, R. and S. Wang. 1992. New principles for optical filters. Appl. Phys.

Lett. 61, 1022-1024 .

Marcus, D., S. W. Hell. 2002. Focal spots of size λ/23 open up far-field florescence

microscopy at 33 nm axial resolution,". Phys. Rev. Lett. **88**, 16390.

Massig, J. H. 2002. Digital off-axis holography with a synthetic aperture. Opt. Lett. **27**, 2179–2181.

Micó, V. , J. Garcia and Z. Zalevsky. 2008. Axial superresolution by synthetic aperture generation. J. Opt. A: Pure Appl. Opt. **10**, 125001.

Micó, V. , Z. Zalevsky, and J. García. 2008. Common-path phase-shifting digital holographic microscopy: a way to quantitative imaging and superresolution. Opt. Commun. **281**, 4273-4281.

Micó, V. , Z. Zalevsky, C. Ferreira, and J. García. 2008. Superresolution digital holographic microscopy for three dimensional samples. Opt. Exp. **16**, 19260-19270.

Micó, V., Z. Zalevsky and J. Garcia. 2006. Superresolution optical system by common-path interferometry. Opt. Exp. **14**, 5168-5177.

Micó, V., Z. Zalevsky and J. García. 2007. Synthetic aperture microscopy using off-axis illumination and polarization coding. Opt. Commun. **276**, 209-217.

Micó, V., Z. Zalevsky, P. Garcia-Martinez and J. Garcia. 2006. Superresolved imaging in digital holography by superposition of tilted wavefronts. Appl. Opt. **45**, 822-826.

Micó, V., Z. Zalevsky, P. Garcia-Martinez, and J. Garcia. 2004. Single-step superresolution by interferometric imaging. Opt. Exp. **12**, 2589-2595.

Micó, V., Z. Zalevsky, P. García-Martínez, and J. García. 2006. Synthetic aperture superresolution with multiple off-axis holograms. Jour. Opt. Soc. Amer. **A23**, 3162-70.

Moskovits, M. 1985. Surface-enhanced spectroscopy. Rev. Mod. Phys. **57**, 783.

Murphy, D. 2001. Fundamentals of Light Microscopy and Digital Imaging. New York:

John Wiley and Sons.

Nagorni, M. and S. W. Hell. 1998. 4Pi-confocal microscopy provides three dimensional images of the microtubule network with 100- to 150-nm resolution. J. Struct. Biol. **123**, 236-247.

Nelson, D. F. and E. H. Turner. 1968. Electro-optic and piezoelectric coefficients and refractive index of gallium phosphide. J. Appl. Phys. **39**, 3337-3343.

Nesterov, A.V., V.G. Niziev. 2005. Vector solution of diffraction task using the Hertz vector. Phys. Rev. **E71**, 046608.

Neumann, A., Y. Kusnetsova and S. R. J. Brueck. 2008. Structured illumination for the extension of imaging interferometric lithography. Opt. Exp. **16**, 6785-6793.

Neumann, A. , Y. Kuznetsova and S. R. J. Brueck**.** 2008. Optical resolution below λ/4 using synthetic aperture microscopy and evanescent-wave illumination. Opt. Exp. **16**, 20477-20485.

Novotny, L. and S. J. Stranick. 2006. Near-field optical microscopy and spectroscopy with pointed probes. Annu. Rev. Phys. Chem. **57**, 303-331.

Pawley, J. B. 2006. Handbook of Biological Confocal Microscopy, (third edition). Springer-Verlag.

Pendry, J. B. 2000. Negative Refraction Makes a Perfect Lens. Phys. Rev. Lett. **85**, 3966.

Pitter, M. C., C. W. See, and M. G. Somekh. 2004. Full-field heterodyne interference microscope with spatially incoherent illumination. Opt. Lett. **29**, 1200-1202.

Price, J., P. Bingham, and C.E. Thomas. 2007. Improving resolution in microscopic holography by computationally fusing multiple, obliquely-illuminated object waves in

the Fourier domain. Appl. Opt. **46**, 8227-833.

Rao, Z., L. Hesselink and J. S. Harris. 2007. High-intensity bowtie-shaped nano-aperture vertical-cavity surface-emitting laser for near-field optics. Opt. Lett. **32**, 1995-1997.

Raub, A.K., A. Frauenglass, S.R.J. Brueck *et al.* 2004. Deep-UV immersion interferometric lithography. Proc. SPIE **5377**, 306-318.

Rayleigh, L. 1879. Investigations in optics, with special reference to the spectroscope. The London, Edinburgh, and Dublin Philosophical Magazine and Journal of Science, **8**(49), Part XXXI, 261-274.

Richards, B. and E. Wolf. 1959. Electromagnetic diffraction in optical systems. II. Structure of the image field in an aplanatic system. Proc. R. Soc. London **A253**, 358–379.

Rittweger, E., K. Y. Han, S. E. Irvine, C. Eggeling and S. W. Hell. 2009. STED microscopy reveals crystal colour centres with nanometric resolution. Nature Photon. **3**, 144-147.

Rudolph, W., P. Dorn, X. Liu, N. Vretenar, R. Stock. 2003. Microscopy with femtosecond laser pulses: applications in engineering, physics and biomedicine. Appl. Surf. Sci. **208**, 327.

Rust, M. J., M. Bates & X. Zhuang. 2006. Sub-diffraction-limit imaging by stochastic optical reconstruction microscopy (STORM). Nature Methods **3**, 793-796.

Schmitt, J.M. 1999. Optical coherence tomography (OCT): a review. IEEE Journal of Selected Topics in Quantum Electronics 5 (4): 1205.

Schnars, U. 1994. Direct phase determination in hologram interferometry with use of

digitally recorded holograms. J. Opt. Soc. Am. **A11**, 2011–2015.

Schnars, U. and W. P. O. Jüpter. 1994. Direct recording of holograms by a CCD target and numerical reconstruction. Appl. Opt. **33**, 179–181.

Schwarz, C. J., Y. Kuznetsova, and S. R. J. Brueck. 2003. Imaging interferometric microscopy. Opt. Lett. **28**, 1424-1426.

Sentenac, A., P. C. Chaumet, and K. Belkebir. 2006. Beyond the Rayleigh Criterion: Grating Assisted Far-Field Optical Diffraction Tomography. Phys. Rev. Lett. 97, 243901.

Shaked, N. T., Yi. Zhu, M. T. Rinehart, and A. Wax. 2009 Two-step-only phase-shifting interferometry with optimized detector bandwidth for microscopy of live cells. Opt. Express **17**, 15585-15591.

Shalaev, V. M. 2007. Optical negative-index metamaterials. Nature Photonics **1**, 41.

Shemer, A., D. Mendlovic, Z. Zalevsky, J. Garcia, and P. García-Martínez. 1999. Superresolving optical system with time multiplexing and computer decoding. Appl. Opt. **38**, 7245–7251.

Sheppard, C. J. R. and Z. Hegedus. 1998. Resolution for off-axis illumination. J. Opt. Soc. Amer. **A15**, 622–624.

Smith, D. R., D. Schurig, M. Rosenbluth, S. Schultz, S. A. Ramakrishna and J. B. Pendry. 2003. Limitations on subdiffraction imaging with a negative refractive index slab. Appl. Phys. Lett. **82**, 156.

Smith, S. W. 2007. The Scientist and Engineer's Guide to Digital Signal Processing, ISBN 0-7506-7444-X**,** http://www.dspguide.com/ch11/4.htm.

Smolev, S., A. Biswas, A. Frauenglass and S.R.J. Brueck. 2006. 244-nm imaging interferometric lithography test bed. Proc. SPIE **6154,** 61542K.

Smolyaninov, I., Y. J. Hung and C. C. Davis. 2007. Magnifying superlens in the visible frequency range. Science **315**, 1699-1701.

SOPRA Data Base. 2013. http://refractiveindex.info/

Sparrow, C.M. 1916. On spectroscopic resolving power. The Astrophysical Journal **64**, 76-86.

Sun, P. C. and E. N. Leith. 1992. Superresolution by spatial–temporal encoding methods. Appl. Opt. **31**, 4857–4862.

Tamaguchi, I., J. Kato, S. Ohta, and J. Mizuno. 2001. Image formation in phase-shifting digital holography and applications to microscopy. Appl. Opt. **40**, 6177-6185.

Toraldo di Francia, G. 1955. Resolving power and information. J. Opt. Soc. Am. **45**, 497–501.

Toraldo di Francia, G. 1969. Degrees of freedom of an image. J. Opt. Soc. Am. **59**, 799–804.

Török, P. and F-J. Kau. 2007. Optical Imaging and Microscopy, Springer-Verlag.

Tridhavee, T.M., B. Santhanam, S.R.J. Brueck. 2005. Optimization and apodization of aerial images at high NA for imaging interferometric lithography. J. of Microlith., Microfab. and Microsys 4, 023009.

Tyler, S., D. L. Ralston, P. Marks, S. Carney, and S. A. Boppar. 2008. Real-time interferometric synthetic aperture microscopy. Opt. Exp. **16**, 2555.

Tyler, S., D. L. Ralston, P. Marks, S. Carney, and S. A. Boppart. 2007. Interferometric

synthetic aperture microscopy. Nature Physics **3**, 129.

Vainrub, A., O. Pustovyy, and V. Vodyanoy. 2006 . Resolution of 90 nm (λ/5) in an optical transmission microscope with an annular condenser. Opt. Lett. **31,** 2855-2857.

Vedantam, S., H. Lee, J. Tang, J. Conway, M. Staffaroni and E. Yablonivitch. 2009. A plasmonic dimple lens for nanoscale focusing of light. Nano Lett. 9, 3447-3452.

Voelz, D. G., K. A. Bush, and P. S. Idell. 1997. Illumination coherence effects in laser-speckle imaging: modeling and experimental demonstration. Appl. Opt. **36**, 1781-1788

Webb, R. H. 1996. Confocal optical microscopy. Rep. Prog. Phys. **59**, 427-471.

Williams, C. S. and O.A. Becklund. 1989. Introduction to the Optical Transfer Function. New York: John Wiley and Sons, p. 338.

Wilson, T. 1990. Confocal Microscopy. London: Academic press.

Wu, Q., L. P. Ghislan, and V. B. Elings. 2000 . Imaging with solid immersion lenses, spatial resolution, and applications. Proc. IEEE **88**, 1491-1498.

www.cytoviva.com (accessed 11/1/2009).

Yamaguchi, I. and T. Zhang. 1997. Phase-shifting digital holography. Opt. Lett. **22**, 1268–1270.

Yamaguchi, I., J.-I. Kato, S. Otha, and J. Mizuno. 2001. Image formation in phase-shifting digital holography and applications to microscopy. Appl. Opt. **40**, 6177–6186.

Zalevsky, Z. and D. Mendlovic. 2002. Optical Super Resolution. Springer-Verlag.

Zalevsky, Z., D. Mendlovic, and A. W. Lohmann. 1999. Optical systems with improved resolving power. In *Progress in Optics* **15**, ed. E. Wolf, Chap. 4.

Zernike, F. 1942. Phase contrast, a new method for the microscopic observation of

transparent objects. Physica **9**, 686-698.

Zhang, T. and I. Yamaguchi. 1998. Three-dimensional microscopy with phase-shifting digital holography. Opt. Lett. **23**, 1221–1223.

Zlotnik, A., Z. Zalevsky, and E. Marom. 2005. Superresolution with nonorthogonal polarization coding. Appl. Opt. **44**, 3705–3715.